الجمهورية الجزائرية الديمقراطية الشعبية
The People's Democratic Republic of Algeria
وزارة التعليم العالي و البحث العلمي
Ministry of Higher Education and Scientific Research
جامعة الشهيد حمة لخضر –الوادي
University of Echahid Hamma Lakhdar –EL OUED

Faculty of Exact Sciences — **كلية العلوم الدقيقة**

Department of Physics — **قسم الفيزياء**

Ref : …… — **المرجع: ……**

Thesis presented for the purpose of obtaining the degree of Doctorate LMD

Specialty: Physics

Option: Fondamental Physics

SUBJECT OF THE THESIS:

Non-linear Optical Properties of Nickel Oxide Undoped and (Li, Ca) Doped

Presented by :

Mr. Abdellatif LAIB

Publicly defended on: 05/05/2024

In front of the jury composed of:

M : Mohammed Sadok MAHBOUB	**Pr**	**El oued University**	**President**
M : Azzeddine BEGGAS	**Pr**	**El oued University**	**Supervisor**
M : Rahal ACHOUR	**MCA**	**El oued University**	**Examiner**
M : Yasin AOUN	**Pr**	**El oued University**	**Examiner**
M : Omar BENTOUILA	**Pr**	**Ouargla University**	**Examiner**
M : Abderrahim ACHOURI	**Pr**	**Ouargla University**	**Examiner**

Academic year: 2023/2024

Dedicace

- To my parents
- To my sisters and brothers
- To all my family
- To my friends
- To my teachers and colleagues

Abdellatif Laib

Acknowledgements

May Allah grant mercy to my dear Professor, Dr. Athman BENHAOUA.

He was a guiding light who helped me complete this work. With a heavy heart, I write these words to express my deepest gratitude for his constant support. He was always there to offer help and advice throughout my studies.

History will remember his contributions and the mark he left on this field through his own work, as well as the work of his students. This project was one of the last he oversaw. May Allah accept all his efforts as good deeds and grant him a place in Paradise.

Ameen.

Abdellatif Laib

Acknowledgements

I begin with expressions of thanks and praises for Allah, who inspired and enabled me to successfully complete this work.

Foremost, I wish to convey my profound appreciation to His Eminence Pr. Azzeddine BEGGAS for his unwavering support and sagacious guidance throughout my research journey. His profound insights and unwavering encouragement have been instrumental in shaping the trajectory of my academic pursuits, and for that, I am deeply grateful.

I would also like to acknowledge Dr. Zoubir BECER for his significant contributions that greatly enhanced the quality of this thesis. Additionally, I extend my sincere thanks to Professors Salah Eddine LAOUINI, Fethi BOURAS, and Mohammed El Hadi ATTIA for their invaluable assistance and guidance during the research process.

A special acknowledgment is reserved for the members of the evaluation committee, namely, Pr. Mohammed Sadok MAHBOUB, Dr. Rahal ACHOUR, Pr. Yasin AOUN, Pr. Omar BENTOUILA, and Pr. Abderrahim ACHOURI, for dedicating their valuable time to review and evaluate my thesis.

In conclusion, I extend my deep thanks and appreciation to all those who supported me, contributing to the success of this scholarly journey.

Abdellatif Laib

contents

Chapter 2: Nonlinear Optical Responses in Materials

Chapter 3: Production and Characterization of NiO Thin Films

Chapter 4: Exploring Calcium Doping Effects on NiO Thin Films

List of figures

Chapter 2

Chapter 3

Chapter 4

List of Tables

General introduction

Prelude

In recent years, semiconductor metal oxide materials such as SnO_2, TiO_2, ZnO, and NiO have received greater attention and have been extensively studied, sparking considerable interest in both academic and industrial spheres. At the nanoscale dimension, these materials exhibit attractive physical qualities and benefits, such as stability, non-toxicity, cheap cost, etc., where their properties differ significantly from those at similar micro and macro dimensions. Metal oxides are desirable possibilities, particularly in photovoltaics and optoelectronics, as well as for many technological domains (Moseley, 2017; Lany, 2015; Dey, 2018).

Transparent conducting oxides have undergone a notable scientific resurgence in recent times, as the synthesis and investigation of entities known as "nanoparticles" have extended to become a crucial multidisciplinary field of study globally (Chtouki et al., 2017a). As the particle size becomes smaller, the ratio of surface atoms to internal atoms increases, making such particles important in the performance of new functional materials (Abd-Lefdil et al., 2014). Significant nanoparticle characteristics, including chemical, electrical, mechanical, and optical characteristics, clearly set them apart from the comparable "bulk" material. One of these qualities is the nonlinear optical (NLO) response of nanoparticles, which is markedly improved in comparison to the corresponding "bulk" materials because of their atomic-scale structures, as well as their interface and surface structures (Chtouki et al., 2017a; Abd-Lefdil et al., 2014). Materials with high third-order optical nonlinearity and quick reaction times are crucial for future optical devices (Abd-Lefdil et al., 2014). Since these NLO materials have such high nonlinear optical responses, they are considered good candidates for use in fiber optic communication systems such as all-optical switching, routing units, digital signal recovery, and optical storage media. Consequently, extensive research has been conducted in recent years to delve into the nonlinear optics of nanoparticles (Darabi et al., 2014).

Metal oxide thin films are well-known materials for electrical and optoelectronic applications due to their compatibility with large-area synthesis and low cost. Numerous studies have been undertaken to comprehensively characterize the preparation methods and properties of thin films incorporating transition metal oxides. Among the transition metal oxides, nickel oxide (NiO) is a widely used oxide material that has attracted widespread attention due to its excellent chemical stability and optical, electrical, and magnetic properties. NiO crystallizes in NaCl cubic structure and is a p-type semiconducting material with a band gap energy of 3.6 to 4 eV at ambient temperature (Taşköprü et al., 2016) . Nickel oxide (NiO) thin films have enormous

potential in a variety of applications, including electrochromic devices (Avendaño et al., 2006; Granqvist, 2008) , gas sensors (Taşköprü et al., 2016), lithium batteries (Taşköprü et al., 2016; Yin and Park, 2014), and supercapacitors (Taşköprü et al., 2016; Al-bahrani et al., 2015). Nickel oxide thin films have demonstrated their potential uses in photodetectors, displays, and photovoltaic solar cells (Manjunatha et al., 2015; Park et al., 2005). Several deposition methods are used to deposit nickel oxide, and each one offers advantages of certain qualities that are ideal for particular purposes. A few popular fabrication methods for depositing NiO include chemical bath deposition, chemical vapor deposition, spray pyrolysis, and thermal evaporation (Manjunatha et al., 2015; Park et al., 2005).

- **Bibliographic study**

Numerous researchers are striving to explore NLO materials in various disciplines of optoelectronics because they have applications in a wide range of science and technology. The substantial rise in publications over the years, nearing almost 570 papers in 2021, underscores the significant endeavors in the nonlinear optics domain. Figure 1 displays a bar graph that depicts the number of publications during the previous five years.

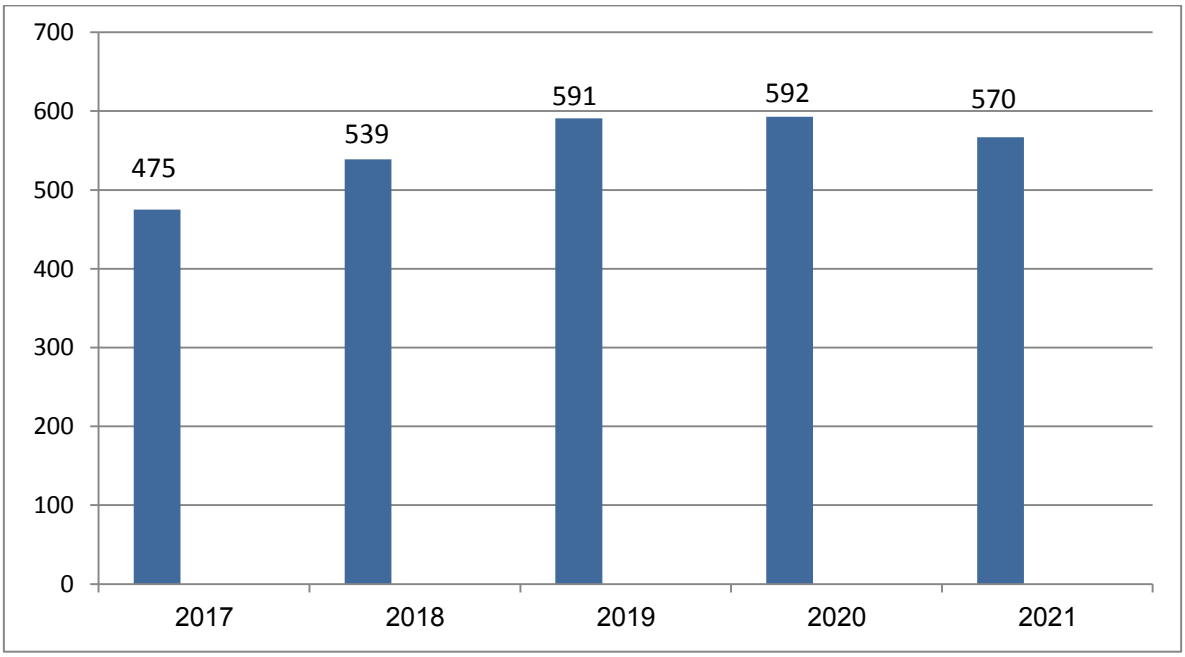

Figure 1 Number of publications in the field of nonlinear optics in recent years (Bano et al., 2021)**.**

Nanometal oxides have gained significant attention from researchers owing to their diverse applications. The nanoparticles have been broadly examined, looking at their outstanding chemical stability and considerable optoelectrical properties among the different nano metal

oxides, nickel oxide (NiO). As a result, many scientists working in the physics field are interested in knowing more about the chemical, morphological, linear, and optical characteristics of doped and undoped NiO thin films produced using various techniques. Numerous reviews and studies have been achieved in the past few years, including studies about the nonlinear theory and materials properties.

There is no question that the methods used to prepare NiO materials play a crucial role in their shaping, architecture, and morphology, which in turn leads to optoelectronic performances and nonlinear response. Melo Jr et al. (de Melo et al., 2009) reported that thermal evaporation of nickel chips deposits NiO films of different thicknesses on glass substrates. These films exhibit significant nonlinear refraction of 10^{-12} cm^2/W with a negligibly nonlinear absorption when exposed to an 800 nm laser pulse. Furthermore, by altering the annealing temperature, NiO micro rods with variable aspect ratios were created using a chemical method. When illuminated by a 532 nm, 5ns laser pulse, effective two-photon absorption coefficients are estimated in the order of 10^{-11} m/W (Karthikeyan et al., 2016). Additionally, Chtouki et al. have compared the nonlinear optical properties of thin NiO films made by spin-coating and spray pyrolysis (Chtouki et al., 2017b).

It is widely recognized that doping provides an adequate approach to controlling the optical and electrical characteristics of the transition metal oxides. In this regard, the introduction of dopants into NiO has recently gained prominence as a strong candidate for applications related to nonlinearity, primarily due to its ability to reduce the band gap compared to the undoped form. Shkir et al. examined the reliance of the nonlinear optical responses of Cr-doped NiO films on dopant concentration levels (1, 3, 5, and 7 wt%) (Shkir et al., 2018). Meanwhile, Cu (1, 5, 10 and 15 wt%) doped NiO films are effectively produced utilizing the spin coating deposition approach, and it is also discovered that the NLO responses may be adjusted as needed under 632.8 nm CW laser irradiation (Ganesh et al., 2019). Additionally, the impacts of tin doping on the structural, linear, and nonlinear optical characteristics of the spin-coated NiO thin films were investigated (Yan et al., 2020) . Conversely, N has been injected into the NiO films using the typical sol-gel spin coating method. It is discovered that when doping rises (1, 5, 10 and 15 wt%), the transparency and band gap of the NiO films decrease concurrently, which is consistent with the increased nonlinear refraction effect. In addition, the nonlinear absorption effect is less significant at higher levels of doping (Ganesh et al., 2018) .

M. Shkir et al.(Shkir et al., 2020) Through a straightforward spin-coating process, nanostructured NiO thin films were produced with different Fe concentrations (0, 1, 2.5, and 5 wt%), which are then investigated for potential nonlinear optoelectronic applications. According to the optical analysis, the films that have been grown have a high degree of transparency—roughly 70–85%. The assessment of several optical characteristics was performed, and a direct energy gap was discovered in the range of 3.60 to 3.64 eV for 0, 1, 2.5, and 5 wt% Fe:NiO films, respectively. The nonlinear properties were examined, and it was discovered that the values of χ^1, χ^3, and n_2 had increased from 0.16 to 0.54, 1.3×10^{-13} to 1.2×10^{-11} esu and 2.6×10^{-12} to 1.7×10^{-10} esu, respectively. The improved linear and nonlinear properties brought on by the Fe-doping concentration increase the usefulness of the produced films in the optoelectronics field.

V. Ganesh et al. discussed the impact of Cu-doped NiO thin films prepared using the spin coating method on their nonlinear optical properties (Ganesh et al., 2019). The researchers concluded that Cu is powerful in changing the NLO characteristics of NiO thin film. It optimized the nonlinear refraction phase from positive to negative, which is consistent with the Z-scan data. Based on Z-scan analyses, many nonlinear constants were determined. The observed values for χ^1, χ^3, and n_2 ranged from 0.5 to 7.5, 8×10^{-8} to 0.5×10^{-8} esu, and 0.5×10^{-8} to 8.5×10^{-8} esu, respectively.

The nonlinear optical characteristics of the Sn doped NiO thin films produced by spin-coating were investigated by Chtouki et al. (Chtouki et al., 2017a). A peak THG signal value of 3.13×10^{-21} m^2/V^2 has been recorded by these researchers in the film doped with 1 at% Sn. The values of χ^3 were evaluated, and found to vary between 2.25×10^{-21} m^2/V^2 and 3.13×10^{-21} m^2/V^2 depending on the amount of doping. The nonlinear optical parameters were less than those that were shown in the works of M. Shkir et al. (Shkir et al., 2020) and V. Ganesh et al. (Ganesh et al., 2019).

Chtouki et al. (Chtouki et al., 2017b) performed a comparative investigation of NiO films prepared utilizing two different deposition processes. The researchers employed both spin coating and spray pyrolysis deposition methods to examine and compare the structural, morphological, linear, and nonlinear optical characteristics of NiO thin films. The solution for spray pyrolysis deposition consisted of a blend of 0.5 M and 0.75 M nickel chloride dissolved in 30 ml of deionized water. The spraying process lasted for 3 minutes on a pre-heated glass substrate at 350 °C. The films exhibited a reduction in the band gap as the precursor concentration increased in both methods. Third harmonic generation analysis of the nonlinear

optical properties indicated a slightly higher third-order nonlinear optical susceptibility for the sprayed film compared to the spin-coated film. Specifically, the spin coating method yielded a nonlinear optical susceptibility (χ^3) of 1.49×10^{-21} m^2/V^2, while the spray pyrolysis technique resulted in 1.94×10^{-21} m^2/V^2.

In a different work, to evaluate the nonlinear optical properties of thin films prepared using the spin coating technique, Ganesh et al. conducted experiments that yielded graphs showing changes in χ^1, χ^3, and n_2 for NiO thin films doped with nitrogen (N) with different concentrations: 1%, 5%, 10%, and 15% (Ganesh et al., 2018), the Z-scan investigations demonstrate that the theoretically estimated values for the nonlinear refractive index and absorption index perfectly matched the outcomes of the experiments. This investigation also shows that all parameters act consistently. Additionally, the sensitivity levels rise when N doping concentrations rise. The ranges of the observed χ^1, χ^3, and n_2 values were 0.49-3.9 esu, 0.5×10^{-10}-3.46×10^{-9} esu, and 0.46×10^{-9}-1.21×10^{-8} esu, respectively.

In a paper written by V. Usha et al. (Usha et al., 2018), NiO nanoparticles were produced using the simple and inexpensive sol-gel process. They studied the linear and nonlinear optical characteristics. The XRD results showed that NiO is nanocrystalline and free of any secondary phases, with a predicted crystallite size of 25 nm. The Wemple-DiDomenico technique was used to compute the static refractive index and high-frequency lattice dielectric constants. Additionally, the calculation of linear and nonlinear optical susceptibilities yielded a maximum value of 2.2×10^{-12} esu for the nonlinear optical susceptibility χ^3.

Ganesh et al.'s (Ganesh et al., 2022) research centered on determining how Gd (1, 3, and 5%) doping affected the structural, morphological, optical, and electrical characteristics of NiO thin films produced on glass substrate by spray pyrolysis. According to an X-ray diffraction analysis, the Gd:NiO (0-5%) films that were deposited had a cubic structure with a preferred orientation growth along the (111) direction. The prepared films show a decrease in optical band gap energy values which clearly suggest that with increases of Gd content and an average transparency of 70%. The refractive indices in these films range between 1.5 and 2.6. Moreover, Gd-doped NiO films exhibit significantly heightened values of linear and nonlinear optical parameters, including χ^1, χ^3, and n_2, which were measured at 0.98 esu, 3.31×10^{-10} esu, and 2.92×10^{-9} esu, respectively. According to the current research, NiO films' linear and non-linear optical characteristics are significantly influenced by the amount of Gd doping, which makes them beneficial for various of optoelectronic device applications.

Shkir et al. (Shkir et al., 2018) produced thin films of NiO with varied concentrations (1, 3, 5, and 7 wt%) of Cr doping at ambient temperature and then annealed at 450 °C in an oxygen atmosphere for 2 hours using a low-cost spin-coating process. An X-ray diffraction investigation indicates that all the produced films are polycrystalline with a cubic phase. For all the films, the direct optical energy gap was measured and found to be between 3.85 and 3.78 eV. The high optical conductivity value demonstrates that the films have a high light responsiveness. The values of n_2 and $\chi 3$ are determined to be in the ranges of 1.81×10^{-7} to 1.09×10^{-10} and 3.3×10^{-8} to $3.5 \times 10{-}^{12}$ esu, respectively.

Yasemin Pepe and colleagues improved the optical nonlinearity of nickel oxide by creating nanoparticles of Cr/Sb-doped NiO using the hydrothermal process. The spin-coating process was used at 400 ° C to produce the membranes on a glass substrate. According to XRD patterns, nanoparticle crystal diameters ranged from 10.3 nm to 17.3 nm. The band gap energy values ranged from 3 eV to 1.42 eV and decreased as the doping concentrations increased. Doped nanocomposite films have greater transmittances than pure films. Nanocomposite films were found to have a nonlinear absorption coefficient of 1.84×10^{-4} cm/W, which rose to 7.45 10^{-4} cm/W with Cr doping and 4.18×10^{-4} cm/W with Sb doping (Pepe et al., 2021).

NiO nanoparticles have unveiled new avenues in nonlinear optical research owing to the amalgamation of various intriguing properties. However, their contributions to applications are relatively constrained, therefore, warrant further exploration.

○ Objectives of the thesis

Extensive research has been conducted on the development of the n-type semiconductor, which finds use in several fields (Chtouki et al., 2017b). Conversely, p-type semiconductor-related studies are not as widespread. However, their technical applications have garnered significant interest. Among them is nickel oxide, which has a broad band gap averaged in 3.6 eV and 4 eV. It is one of the most studied p-type transition metal oxides because of its low cost, nontoxicity, and good optical transparency (Chtouki et al., 2017b). Generally, the nature of the precursors, elaboration techniques, and doping concentration affect these values (Alshahrie et al., 2016) . The poor p-type conductivity of NiO is one of its drawbacks, which can be considerably enhanced by selecting the right dopant (Krunks et al., 2014).

P-type semiconductors are currently in great demand for optoelectronics devices to compete with n-type materials. They are used in many other applications (Zawadzka et al.,

2019). Because of this, choosing a simple method to create a p-type NiO semiconductor is essential. The spray pyrolysis method is a highly preferred for NiO thin film preparation due to its efficiency in high-quality multi-layer thin film formation (Şimşek et al., 2021). In this study, we will present the morphological, structural, linear, and nonlinear optical characteristics of undoped and doped NiO thin films prepared by the spray pyrolysis method using the SEM, XRD, UV-Vis, and EDX (Chtouki et al., 2021).

Given these important properties of NiO, it seems reasonable and necessary to improve its properties by adding a metal dopant that is appropriate and capable of producing extremely high conducting charges. Similar to the previous years, several researchers have attempted to use various dopants to enhance several important NiO features. In consideration of this, the current study involves the fabrication of NiO thin films with varying concentrations of metal dopants utilizing spray pyrolysis technology. These films undergo structural analysis and are comprehensively studied for their linear and nonlinear (NLO) properties. In recent years, NiO films have been prepared through various procedures to investigate diverse physical properties. However, a significant gap exists in the literature regarding the nonlinear properties of NiO films. Therefore, emphasizing this aspect of the characteristics is intriguing. Understanding these nonlinear properties is crucial for improving the design and application of these materials across a broad spectrum of uses, including nonlinear electronic devices, optical communication systems, and nonlinear optical sensors (Shkir et al., 2018) .

○ Organization of the thesis

The thesis comprises four chapters, commencing with an introduction and concluding with suggestions for future research.

The first chapter offers a succinct examination of nanomaterials and their classification, with particular emphasis on transparent conductive oxides (TCOs), including a detailed exploration of the fundamental attributes of nickel oxide (NiO). Additionally, diverse methodologies utilized in nanomaterial synthesis are delineated, with special attention given to the spray pyrolysis method. Lastly, we underscore the characterization techniques employed for thin films.

The second chapter will provide an in-depth examination of nonlinear optical materials (NLO) and their categorization. Additionally, we will highlight the nonlinear optical phenomena and the corresponding processes.

The third and fourth chapters elaborate on the procedures involved in preparing and characterizing lithium (Li) and calcium (Ca) doped nickel oxide thin films, respectively. Data acquired from analytical methods such as XRD, EDX/SEM, and UV/VIS spectrophotometry are presented graphically and thoroughly examined. Finally, the thesis will conclude with a comprehensive summary and future directions.

References

Abd-Lefdil, M., Douayar, A., Belayachi, A., Reshak, A. H., Fedorchuk, A. O., Pramodini, S., Poornesh, P., Nagaraja, K.K., & Nagaraja, H. S. (2014). Third harmonic generation process in Al doped ZnO thin films. Journal of alloys and compounds, 584, 7-12. https://doi.org/10.1016/j.jallcom.2013.08.134

Al-bahrani, M. R., Liu, L., Ahmad, W., Tao, J., Tu, F., Cheng, Z., & Gao, Y. (2015). NiO-NF/MWCNT nanocomposite catalyst as a counter electrode for high performance dye-sensitized solar cells. Applied Surface Science, 331, 333-338. https://doi.org/10.1016/j.apsusc.2015.01.015

Alshahrie, A., Yahia, I. S., Alghamdi, A., & Al Hassan, P. Z. (2016). Morphological, structural and optical dispersion parameters of Cd-doped NiO nanostructure thin film. Optik, 127(12), 5105-5109. https://doi.org/10.1016/j.ijleo.2016.02.023

Avendaño, E. S. T. A. B. A. N., Berggren, L., Niklasson, G. A., Granqvist, C. G., & Azens, A. (2006). Electrochromic materials and devices: Brief survey and new data on optical absorption in tungsten oxide and nickel oxide films. Thin solid films, 496(1), 30-36. https://doi.org/10.1016/j.tsf.2005.08.183

Bano, R., Asghar, M., Ayub, K., Mahmood, T., Iqbal, J., Tabassum, S., Zakaria, R., & Gilani, M. A. (2021). A theoretical perspective on strategies for modeling high performance nonlinear optical materials. Frontiers in Materials, 8, 783239. https://doi.org/10.3389/fmats.2021.783239

Chtouki, T., El Mrabet, M., Tarbi, A., Goncharova, I., & Erguig, H. (2021). Comprehensive review of the morphological, linear and nonlinear optical characterization of spin-coated NiO thin films for optoelectronic applications. Optical Materials, 118, 111294. https://doi.org/10.1016/j.optmat.2021.111294

Chtouki, T., Soumahoro, L., Kulyk, B., Bougharraf, H., Kabouchi, B., Erguig, H., & Sahraoui, B. (2017b). Comparison of structural, morphological, linear and nonlinear optical properties of NiO thin films elaborated by spin-coating and spray pyrolysis. Optik, 128, 8-13. https://doi.org/10.1016/j.ijleo.2016.10.007

Chtouki, T., Soumahoro, L., Kulyk, B., Erguig, H., Elidrissi, B., & Sahraoui, B. (2017a). Spin-coated Tin-doped NiO thin films for third order nonlinear optical applications. Optik, 136, 237-243. https://doi.org/10.1016/j.ijleo.2017.01.110

Darabi, H., Adelifard, M., & Rajabi, Y. (2019). Characterization of nonlinear optical refractive index for graphene oxide–silicon oxide nanohybrid composite. Journal of Nonlinear Optical Physics & Materials, 28(01), 1950005. https://doi.org/10.1142/S021886351950005X

de Melo, R. P., da Silva, B. J., dos Santos, F. E. P., Azevedo, A., & de Araújo, C. B. (2009). Nonlinear refraction properties of nickel oxide thin films at 800 nm. Journal of Applied Physics, 106(9). https://doi.org/10.1063/1.3254233

Dey, A. (2018). Semiconductor metal oxide gas sensors: A review. Materials science and Engineering: B, 229, 206-217. https://doi.org/10.1016/j.mseb.2017.12.036

Ganesh, V., Akkera, H. S., Bitla, Y., Haritha, L., AlFaify, S., & Yahia, I. S. (2022). Effect of Gd doping on spray pyrolyzed NiO thin films for optoelectronic applications. Physica B: Condensed Matter, 635, 413786. https://doi.org/10.1016/j.physb.2022.413786

Ganesh, V., Haritha, L., Anis, M., Shkir, M., Yahia, I. S., Singh, A., & AlFaify, S. (2018). Structural, morphological, optical and third order nonlinear optical response of spin-coated NiO thin films: An effect of N doping. Solid State Sciences, 86, 98-106. https://doi.org/10.1016/j.solidstatesciences.2018.10.009

Ganesh, V., Shkir, M., Anis, M., & AlFaify, S. (2019). Structural, morphological and opto-nonlinear studies of Cu: NiO: glass thin films facilely designed by spin coater for electro-optics. Materials Research Express, 6(8), 086439. https://doi.org/10.1088/2053-1591/ab2090

Granqvist, C. G. (2008). Oxide electrochromics: Why, how, and whither. Solar Energy Materials and Solar Cells, 92(2), 203-208. https://doi.org/10.1016/j.solmat.2006.10.027

Karthikeyan, B., Pandiyarajan, T., Hariharan, S., & Ollakkan, M. S. (2016). Wet chemical synthesis of diameter tuned NiO microrods: microstructural, optical and optical power limiting applications. CrystEngComm, 18(4), 601-607. https://doi.org/10.1039/C5CE02232K

Krunks, M., Soon, J., Unt, T., Mere, A., & Mikli, V. (2014). Deposition of p-type NiO films by chemical spray pyrolysis. Vacuum, 107, 242-246. https://doi.org/10.1016/j.vacuum.2014.02.013

Lany, S. (2015). Semiconducting transition metal oxides. Journal of Physics: Condensed Matter, 27(28), 283203. https://doi.org/10.1088/0953-8984/27/28/283203

Manjunatha, K. N., & Paul, S. (2015). Investigation of optical properties of nickel oxide thin films deposited on different substrates. Applied Surface Science, 352, 10-15. https://doi.org/10.1016/j.apsusc.2015.03.092

Moseley, P. T. (2017). Progress in the development of semiconducting metal oxide gas sensors: A review. Measurement Science and Technology, 28(8), 082001. https://doi.org/10.1088/1361-6501/aa7443

Park, S. W., Choi, J. M., Kim, E., & Im, S. (2005). Inverted top-emitting organic light-emitting diodes using transparent conductive NiO electrode. Applied surface science, 244(1-4), 439-443. https://doi.org/10.1016/j.apsusc.2004.10.099

Pepe, Y., Karatay, A., Donar, Y. O., Yildiz, E. A., Sınağ, A., Unver, H., & Elmali, A. (2021). Enhanced nonlinear absorption coefficient and low optical limiting threshold of NiO nanocomposite films. Optik, 227, 165975. https://doi.org/10.1016/j.ijleo.2020.165975

Shkir, M., Arif, M., Ganesh, V., Singh, A., Algarni, H., Yahia, I. S., & AlFaify, S. (2020). An effect of Fe on physical properties of nanostructured NiO thin films for nonlinear optoelectronic applications. Applied Physics A, 126(2), 119. https://doi.org/10.1007/s00339-020-3293-2

Shkir, M., Ganesh, V., AlFaify, S., Yahia, I. S., & Zahran, H. Y. (2018). Tailoring the linear and nonlinear optical properties of NiO thin films through Cr 3+ doping. Journal of Materials Science: Materials in Electronics, 29, 6446-6457. https://doi.org/10.1007/s10854-018-8626-y

Şimşek, B., Ceran, Ö. B., & Şara, O. N. (2021). Difficulties in thin film synthesis. Handbook of Nanomaterials and Nanocomposites for Energy and Environmental Applications, 251-273. https://doi.org/10.1007/978-3-030-36268-3_84

Taşköprü, T., Turan, E., & Zor, M. (2016). Characterization of NiO films deposited by homemade spin coater. International Journal of Hydrogen Energy, 41(16), 6965-6971. https://doi.org/10.1016/j.ijhydene.2015.12.008

Usha, V., Vettumperumal, R., Kalyanaraman, S., & Thangavel, R. (2018). Analysis of linear and nonlinear optical properties of NiO nanoparticles by sol–gel method. International Journal of Nanoscience, 17(05), 1850003. https://doi.org/10.1142/S0219581X18500035

Yan, L., Wang, M., Gong, L., Wang, D., Tian, Y., Tian, Y., ... & Nie, Z. (2020). Enhanced and tunable nonlinear optical responses of nitrogen-doped nickel oxide induced by femtosecond laser excitation. Optical Materials, 106, 109987. https://doi.org/10.1016/j.optmat.2020.109987

Yin, J. L., & Park, J. Y. (2014). Electrochemical investigation of copper/nickel oxide composites for supercapacitor applications. International journal of hydrogen energy, 39(29), 16562-16568. https://doi.org/10.1016/j.ijhydene.2014.04.202

Zawadzka, A., Płóciennik, P., El Kouari, Y., Bougharraf, H., & Sahraoui, B. (2016). Linear and nonlinear optical properties of ZnO thin films deposited by pulsed laser deposition. Journal of Luminescence, 169, 483-491. https://doi.org/10.1016/j.jlumin.2015.04.020

Chapter 1 : Fundamentals Of Thin Films Deposition And Analysis

Chapter 1 | Fundamentals of thin films deposition and analysis

1.1 Introduction

Materials science is an approach employed to explore, examine, and enhance both novel and known materials by integrating synthesis, characterization, and information processing to prepare, analyze, and interpret a wide array of materials. In this context, thin films have garnered increased focus over the last decade, emerging as a significant facet of materials science. Progress in this field necessitates a comprehensive comprehension of the fundamental properties of transparent conducting oxides (TCOs). Therefore, within this chapter, we provide a concise overview of nanomaterials and their categorization, notably transparent conductive oxides (TCOs), along with a specific discussion on the fundamental characteristics of nickel oxide (NiO). Furthermore, we outline various methods employed for the production of nanomaterials with a particular focus on the spray pyrolysis technique. Finally, we highlight the techniques used to characterize thin films (Li et al., 2019; Shimanovich, 2015).

1.2 Transparent conductive oxides (TCOs)

TCOs are significant materials primarily used for research in optoelectronics because they exhibit unique optical properties in the visible light field, such as transparency of more than 85% and band gap exceeding 3 eV in addition to the electrical conductivity (A minimum carrier concentration of 10^{20} cm^{-3}). These oxides often consist of oxygen plus one or two metallic elements, and their properties are highly influenced affected by the components utilized and the deposition technique (Bouaichi, 2019; Rahal, 2017).

In 1907, Baedeker discovered TCO, which was a thin film of cadmium oxide (CdO). TCO's experienced little practical growth in the first 50 years after the discovery of CdO until the chemical deposition technique (pyrolysis) was invented in the 1940s. The breakthrough in the field of TCOs and associated applications came in the 1960s with the development of many compounds that can be classified as TCO materials, such as: NiO, ZnO, In_2O_3, SnO_2. Tin-doped indium oxide (ITO) has long been the most popular material for a range of applications. The lack of indium and its high cost prompted researchers to search for a material that might be an alternative to it. Doped and undoped nickel oxide (NiO) has emerged as a preferable contender due to its good crystal structure, excellent transparency, and good electrical conductivity in the visible area, in addition to being plentiful and inexpensive (Wang et al., 2015; Bouaichi, 2019).

- **Types of TCOs**

All TCOs may be divided into two types, the n-type and p-type categories based on the predominant charge carriers. Applying doping can increase the concentration and mobility of free carriers, resulting in a remarkable enhancement in the material's electrical conductivity. The addition of an element should be taken into account when selecting a p or n-type doped semiconductor. Semiconductors are doped with donors (n-type) and acceptors (p-type) to improve their electrical conductivity. In the most obvious cases, when an atom with a valence higher than +4 is added, it results in an n-type doped semiconductor and an atom with a valence lower than +4 yields a p-type doped semiconductor (Kawazoe et al., 2000; Mitridis, 2008; Banerjee et al., 2005).

Doping occurs when a dopant atom is added and substitutes for one of the component atoms in the network of both (n- and p-type) metal oxide. When it comes to n-type doping, the added corn is associated with four links with adjacent atoms. As a result, the fifth electron of the added atom receives some thermal energy right away and frees up. On the contrary instance, where the valence of the dopant atom is +3, a hole is formed, which can become a free hole in the presence of thermal energy (Mitridis, 2008; Ghougali, 2019).

The insertion of a doping atom into the material's structure causes the formation of new levels in the gap between the conduction and valence bands. The status of the energy levels in semiconductors is described by the band structure theory, which also provides some streamlined graphic designs (Mitridis ,2008; Ghougali, 2019) (Figure 1.1).

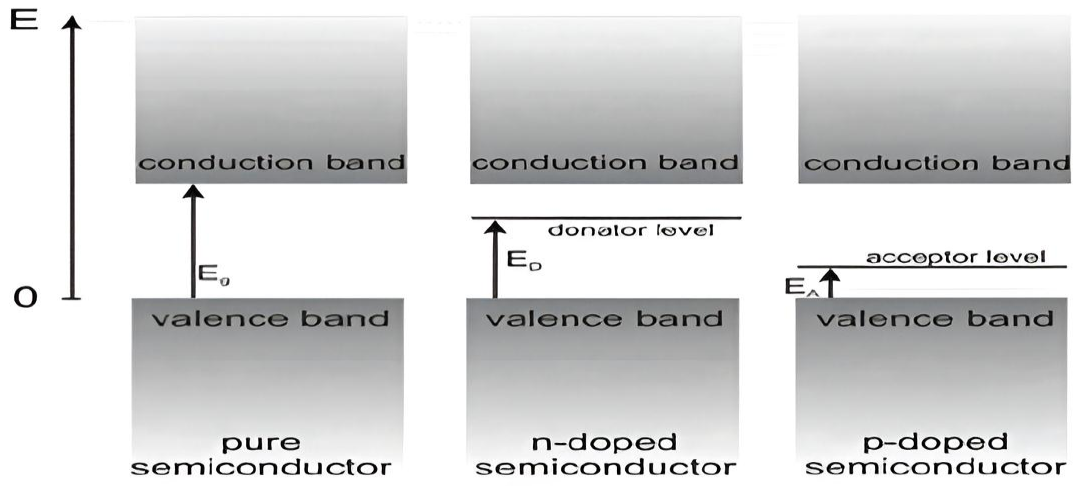

Figure 1.1. Diagram showing the energy band of semiconductors that are doped and pure (also known as extrinsic and intrinsic, respectively) (Mitridis,2008).

1.3 Nickel oxide (NiO)

Due to the possibility of using them in modern technology, TCOs have recently drawn more interest. There have been several studies that detail the creation and characteristics of metal oxide films. Among the extremely few p-type the transition semiconducting oxides, we find nickel oxide (NiO) which is a promising choice in a variety of cutting-edge fields of study due to its unique physical and chemical properties (Taeño et al.,2021).

Nickel (II) oxide is the chemical compound with the formula NiO. It is the principal oxide of nickel; it has a nickel content of 78.55% and an oxygen content of 21.40%, it has a molar mass of 74.69 g/mol (Ukoba et al., 2018). Like many other binary metal oxides, NiO is often non-stoichiometric, meaning that the Ni:O ratio deviates from 1:1. In nickel oxide, this non-stoichiometry is accompanied by a color change, with the stoichiometrically correct NiO being green and the non-stoichiometric NiO being black. NiO can either be a black or green crystalline powder. NiO has a density of 6.67 g/cm^3 and a 1955 °C melting temperature. Furthermore, its refractive index is 2.18 and has a $+660\times10^{-6}$ cm^3/mol magnetic sensitivity (Kunz, 1981).

1.3.1 Crystallographic properties

NiO displays a cubic structure of NaCl-type (rock salt) as seen in Figure 1.2. Where the centers of the faces and the cube's corners are occupied by nickel atoms, whereas the oxygen atoms are concentrated in the center and the middle of the sides of the cube in this crystal, following the structure (FCC). Also, NiO is included in the space group (Fm3m), with a lattice parameter of 4.177 Å. It should be mentioned that at ambient pressure and temperature, NiO is stable and takes a cubic structure. In addition to the cubic shape, a mild cubic-to-rhombohedral distortion may occur in this oxide (Lattice parameters a = b = 0.295 nm and c = 0.722 nm with space group R3m) (Taeño et al., 2021; Chen et al., 2017). Furthermore, the incorporation of doping may cause stress on the crystal lattice, which can be reduced by allowing the structure to relax. The amount and atomic size of the dopant play a significant role in determining the level of stress (Twagirayezu, 2017).

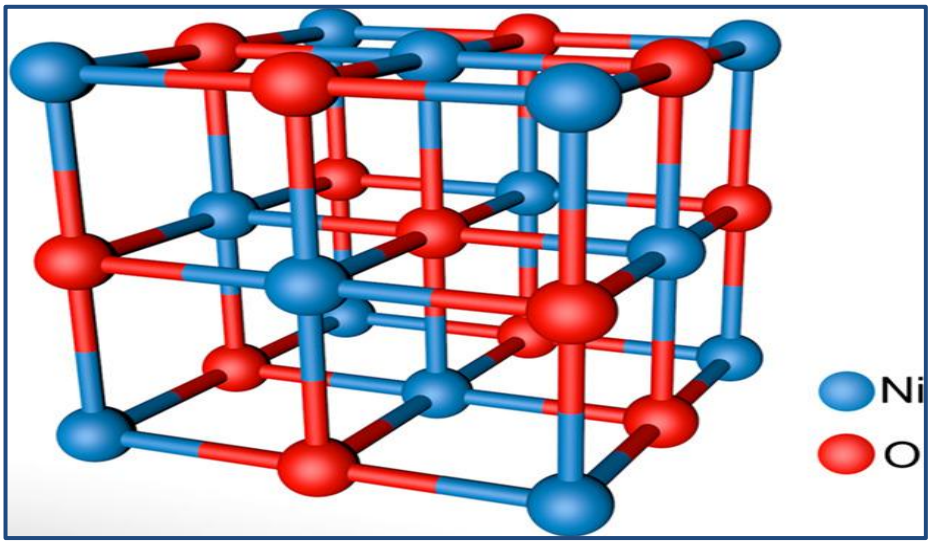

Figure 1.2. Crystal structure of NiO (Yin,2019).

1.3.2 Electrical properties of NiO

Nickel oxide (NiO) is an important wide band gap semiconductor material with a band gap width of approximately 3.6 to 4.0 eV Figure 1.3 (Venter and Botha, 2011). Nickel oxide is a semiconductor that is known for its versatility. The majority of transparent conductive oxides used today are n-type, they are used as electrodes and in optoelectronic applications. However, optical windows require p-type conducting films of which NiO is the most prominent. NiO is a (p-type) semiconductor that has a large bandgap as mentioned above.

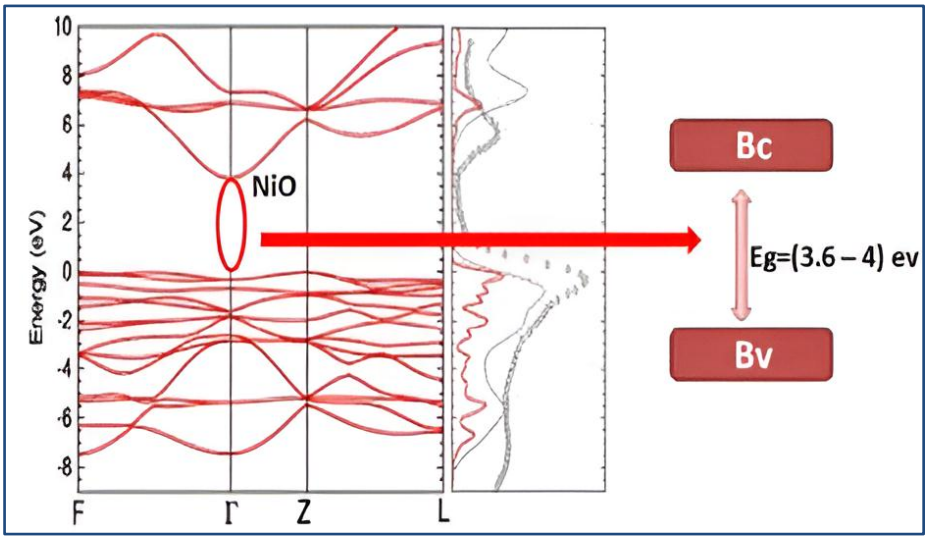

Figure 1.3. Illustration of the NiO Band structure (Ghougali, 2019)

NiO has a cubic shape in its structural masses with a lattice parameter of (0.4177 nm) and is categorized as a Mott- Hubbard insulator with extremely weak conductivity on the order of (10^{-11} Ω^{-1} m^{-1}) at ambient temperature. However, because of the holes that Ni vacancies create in the lattice, the conductivity is dramatically improved when formed as thin films or nanoparticles. Some of NiO's electrical properties were included in Table 1.1 (Makhlouf, 2008).

The electronic configuration of the nickel and oxygen atoms in nickel oxide is defined as follows:

Ni: $1s^2 2s^2 2p^6 3s^2 3p^6 3d^8 4s^2$

O: $1s^2 2s^2 2p^4$

Yongyue Chen et al, investigated the electrical characteristics of NiO films deposited in pure surroundings depending on the growth temperature. They found that the resistivity grew from (20.96 to 44.75 Ω cm) as the temperature raised from room temperature to 300 °C, but the mobility decreased from (1.07 to 0.21 cm^2 /Vs). When the temperature was changed from room temperature to 200 °C, the carrier concentration rises from (2.78×10^{17} to 9.36×10^{17} cm^3), then falls to (6.6×10^{17} cm^3) at 300 °C (Chen et al.,2015).

The primary factor influencing the electrical characteristics of NiO films is the microstructure and composition, together with the deposition circumstances and environment. Since the NiO has an intriguing electrical structure, it has been the subject of intense research for many years (Zaouche, 2021).

Table 1.1. Part of the electrical properties parameters of NiO (Chavillon,2011; Zhao et al.,2015).

Properties	Values
Type of conductivity	P-type
Conductivity $(\Omega.cm)^{-1}$	≤ 0.1
band energy Eg (ev)	3.6 – 4
charge carrier density (cm^{-3})	10^{17}-10^{18}
Hall coefficient (cm^3/C)	5-120
Mobility (cm^2/ V.s)	0.1- 7.6
Dielectric constant	10

1.3.3 Optical properties of NiO

The fact that nickel oxide is characterized by outstanding endurance and electrochemical stability makes it one of the best low-cost polarizable materials with a transmittance of 40% to 80% in the spectral range of 300 to 900 nm (Diha et al.,2018; Talebian and Kheiri,2014). The gap energy value for NiO has been calculated by many studies to be between 3.6 and 4 eV with a refractive index of 2.33 for 2 eV photon energy (Powell and Spicer, 1970). Understanding how NiO's optical properties, including transmittance, absorbance, bandgap, extinction coefficient, refractive index and the real and imaginary components of the dielectric constant, affect device attributes is crucial (Manjunatha and Paul, 2015).

Many optical investigations, including photoemission spectroscopy, have been conducted to comprehend the electronic structure of NiO. One of the most often employed techniques for comprehending and advancing the band structure and energy band gap of crystal structure is ultraviolet-visible spectroscopy (Manjunatha and Paul, 2015).

NiO's optical properties are influenced by preparation conditions, deposition techniques, and doping. G. Turgut et al. (Turgut et al.,2015) reported that the precursor concentration, solvent type, and annealing temperature all have an impact on the optical characteristics of NiO thin films produced using spin-coating for sol-gel. The obtained values of the optical parameters showed that examining the annealed films at 550 °C at a concentration of 0.1 M with methanol solvent gave better results.

1.4 Thin films

1.4.1 Definition

The thin film of a material is usually an arrangement of the components of that material deposited on a substrate. This film is distinguished by its extremely tiny geometric dimensions, which ranging between a few nanometers and a micrometer (Beggas, 2018). Thin films are produced through several stages of growth summarized in nucleation, a process by which the interaction between species (atoms, ions, etc.) coming to the substrate where unstable clusters (nuclei) are formed on the surface of the substrate which are points for the assembly of other atoms. Following the nucleation, grain growth occurs, which is an expansion of growth starting at the nucleating point. These grains collide and combine to produce a bigger grain. This sort of

coalescence is caused by grain size expansion and is referred to as growth coalescence. Coalescence can also be triggered by nuclei movement. The formation of crystals is seen in Figure 1.4. Thin films acquire new properties as a result of the nucleation and growth processes (Chopra et al.,2004). These materials' physical and chemical properties are greatly influenced by a variety of deposition parameters, crystalline orientation, thickness, as well as deposition method (Beggas, 2018).

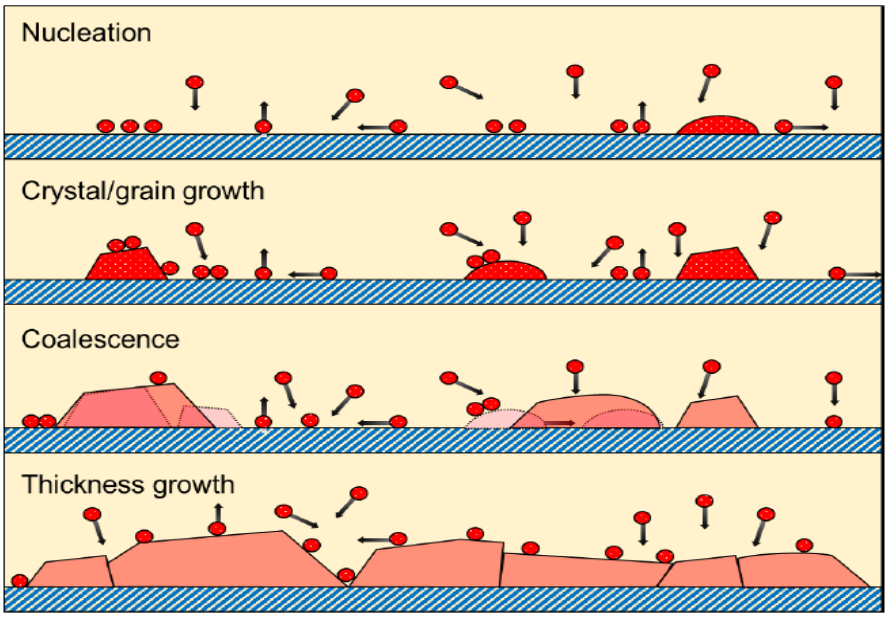

Figure 1.4. Diagram showing the stages of crystal growth (Roffi, 2016)

1.4.2 Thin film Deposition Method

Thin films are in general developed to provide special properties, i.e. optical, electrical, mechanical, and chemical, that satisfy the conditions for specific applications. The desired properties are defined by the resulting film structure, which strongly depends on the selected deposition technique, substrate, and film material. In line with the wide range of applications of thin films, several deposition techniques have been improved/developed to optimize the film properties. Broadly speaking, thin-film production can be realized based on two technological groups, namely physical and chemical deposition techniques.

Optical device design often necessitates tight control over the shape and size of micro- and nanoscale NiO structures, which may be employed as building blocks in a variety of optoelectronic devices. To date, physical or chemical methods have been used to increase the performance of this metal oxide. Several compositional strategies have been used to deposit NiO thin films in recent years (Taeño et al.,2021). Among these, a range of physical techniques has

been reported including PVD, laser ablation (Piriyawong et al.,2012), pulsed-laser deposition (Vanalakar et al.,2015), and molecular beam epitaxy (Wang et al.,2016). Chemical approaches are classified as solution techniques or gas-phase precipitates, which include chemical vapor deposition (CVD) (Purica et al.,2002), spray pyrolysis (Martínez et al.,2019), electrodeposition, dip coating, chemical bath, Gel Sol (Geremew et al.,2022) …etc. Different thin film deposition techniques are displayed in Figure 1.5.

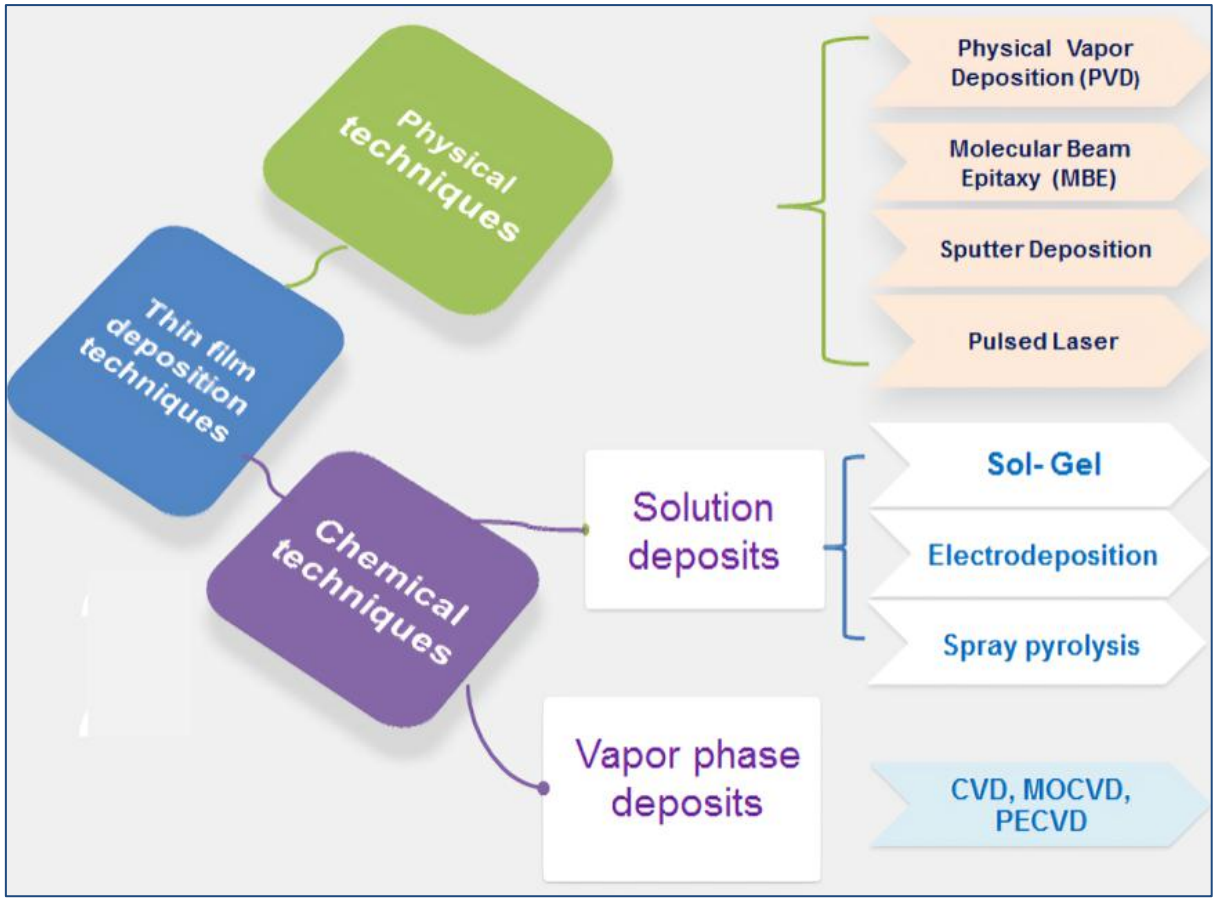

Figure 1.5. Different thin film deposition methods.

The thin film deposition technique utilized can have a substantial impact on the properties of the produced films. Overall, thin films are used to enhance the properties of bulk materials by depositing a layer with the desired chemical and physical characteristics to improve their functionality. Every deposition technique has advantages and disadvantages. Several criteria, including cost, quality, and growth rates, as well as desired film features like as crystallization, morphology and functional properties, will most likely be influenced by the technique used (Manzi, 2016). Spray pyrolysis is an easy, inexpensive, and integrated method to create films with large areas and excellent adhesion with tight growth (Martínez et al.,2019).

1.4.3 Chemical Spray Pyrolysis Technique (SPT)

Recent years have seen a significant increase in the application of the spray pyrolysis technique (SPT) for the production of various thin film types, particularly those made of the oxides and sulfides of numerous metals and semiconductors (Akl et al., 2018; Hassanien and Akl, 2018). The spray pyrolysis system is depicted in Figure 1.6. This system's features of easy equipment setup, high production and low cost made. It's possible for it to be widely applied. Additionally, numerous preparation factors (for example, solution molarity, substrate temperature, flow rate...etc.) may be changed during the film production process (Hassanien and Akl, 2018; Akl, 2014). As a result of these and other advantages, the SPT process is regarded as a successful and appealing technology for producing NiO thin films and many other oxides (Hassanien and Akl, 2018).

In this technique, small droplets of a precursor solution (it contains atoms of the desired compound) are sprayed onto a heated surface. The solvent evaporates and the remaining ingredients react to form the desired material as soon as they contact the hot surface. Spray pyrolysis of cadmium chloride and thiourea dissolved in water with the substrate at about 300°C is one example of how cadmium sulfide films can be created (Chamberlin and Skarman, 1966; Geremew, 2022).

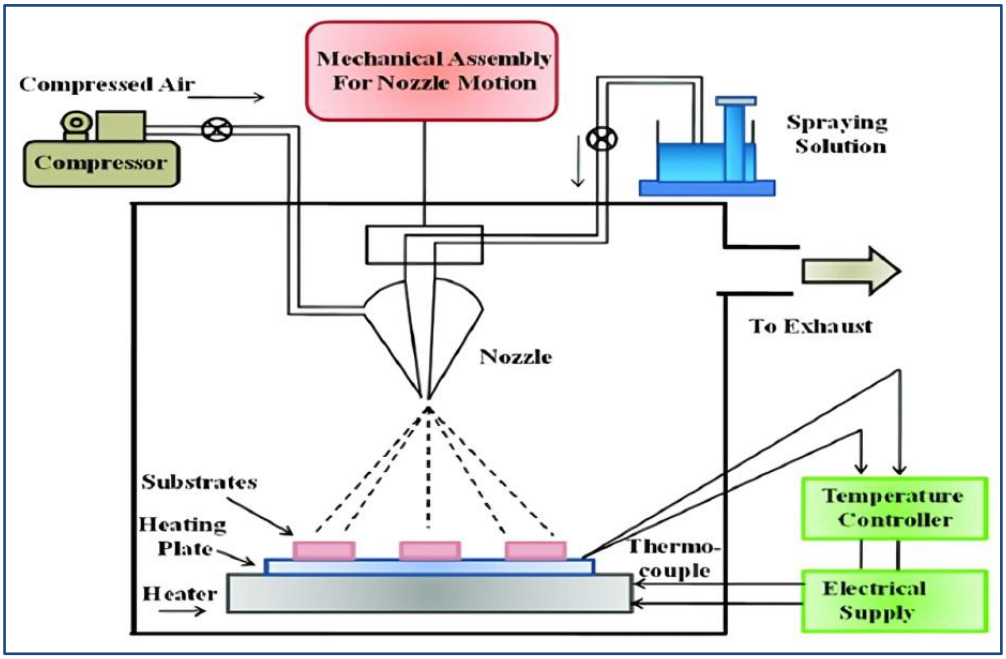

Figure 1.6. Diagram of the spray pyrolysis method (Waghmare et al., 2018).

1.4.4 Mechanism of the (SPT) process

Several processes occur sequentially or concurrently during film production using spray pyrolysis. The quality of films can be raised by comprehending these procedures. The system's nozzle atomizes the precursor solution into tiny aerosols, which fall on heated substrates. Various phases in spray pyrolysis are summarized as follows (Perednis and Gauckler, 2005):

✓ An aqueous precursor solution is first transformed by a spray nozzle into aerosols.
✓ The second phase involves the evaporation of the solvent from the surface of the droplets.
✓ As the droplets reach the substrate in this stage, the solvent vaporizes and precipitates develop.
✓ Prior to the material to be deposited reaching the substrate, it undergoes a series of pyrolysis reactions; this is step 4.
✓ in stage 5, when the deposit touches the substrate, thin films begin to form and develop.
✓ Finally, the nuclei expand, resulting in the creation of a thin metal oxide film (Ukoba et al., 2018).

The kind of films formation process depends on several factors. The most important parameters to be controlled in all of these processes are the substrate temperature, droplet size, carrier gas flow rate, nozzle-to-substrate distance, and the solution content and concentration. Among these variables, the temperature of the substrate has been considered the most important factor in producing thin film from spray pyrolysis processing; this is because the droplets drying, decomposition, crystallization, and grain growth depend strongly on this parameter. The spray pyrolysis mechanisms are schematically depicted in Figure 1.7 as a function of droplet size and substrate temperature. At minimal temperature and significant droplet size, the solvent does not entirely evaporate and the liquid droplet collides with the substrate and evaporates, producing a dry precipitate this process is A. At low to medium temperatures and droplet size (big or medium), the solvent evaporates before the drop sticks to the substrate. Where a dry precipitate falls on the substrate leading to decomposition (process B). At intermediate to elevated temperatures and medium-sized to tiny droplet size, the solvent evaporates prior the drop approaches the surface. After that, the dry precipitate is evaporated, and the vapor spreads to the substrate where the CVD process will take place (process C). Finally, for the highest temperature and droplet size is tiny, Prior to the precursor material reaching the substrate it evaporates. As a

result, there is limited adhesion to the substrate (process D) (Mwakikunga, 2014; Falcony et al., 2018)

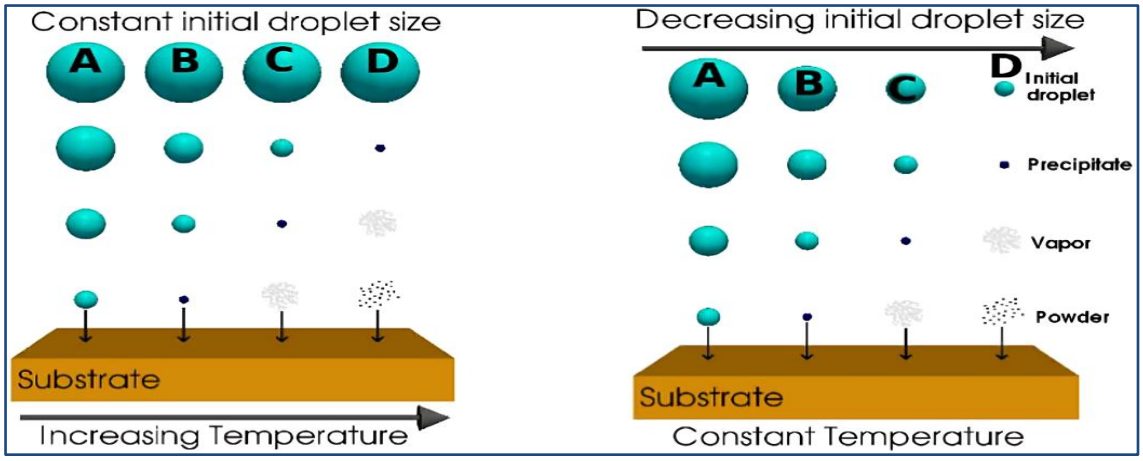

Figure 1.7. Schematic diagram of spray pyrolysis droplet formation stages (Ukoba et al., 2018).

1.4.5 Effect of deposition parameters on the properties of deposited films

Numerous studies have been reported on the structural, optical, and electrical properties of NiO thin films produced via spray pyrolysis. It has been noted that changes in the substrate temperature, dopant, precursor concentrations, spray rate, and so on all impact the film's properties.

1.4.5.1 Effect of Temperature

The substrate temperature at the moment of deposition is a critical element in spray pyrolysis because it regulates the interaction between the evaporation rate of the solvent and the decomposition of the starting material (Marinov et al., 2018). Additionally, it is believed to be the primary factor that significantly influences the morphology of deposited films as well as their optical and electrical characteristics. The film morphology can shift from fractured to porous as the temperature rises. Deposition temperature was indicated as the most significant variable of spray pyrolysis in numerous research (Perednis and Gauckler, 2005; Zahedi et al., 2013).

A study was performed on the deposition temperature concerning the properties of F-doped In_2O_3 films and found that the deposition temperature was discovered to have a significant impact on the films' structure. As the film thickness rises, the degree of favored (4 0 0) orientation also rises (Perednis and Gauckler, 2005). A. Bedia et al. (Bedia et al., 2015) studied the optical and structural properties of ZnO thin films produced on glass substrates at various

temperatures for use with solar cells were investigated. The proportion of PL emission intensity in UV and visible is at its highest at 550°C, indicating fewer flaws are produced, and film quality improves with rising temperature.

1.4.5.2 Effect of Precursor Solution

Precursor solution is critical in the creation of thin films of different chemicals. The precursor solution's physicochemical composition is impacted by the solvent and additives. Aqueous solutions are frequently utilized because they are simple to handle, low cost, safe, and availability of a variety of metal salts that are water-soluble. To have excellent process yield, the solute is required to be of high solubility. As a result, by varying the content of the precursor solution, the properties of the prepared film may be adjusted (Perednis and Gauckler, 2005).

Cattin et al. performed research where four distinct precursors for NiO films were used (Cattin et al., 2008). A modified SPT was used to deposit the precursors. This study involved changing the precursor concentrations between (0.2 M and 0.3 M) while the substrate temperature was 350 °C. The precursors have been nickel nitrate hexahydrate [$Ni(NO_3)_2 \cdot 6H_2O$], [$NiCl_2 \cdot 6H_2O$], [$NiSO_4 \cdot 4H_2O$], and nickel hydroxide hexahydrate [$Ni(OH)_2 \cdot 6H_2O$]. The films were annealed thereafter at 425 °C. All of the precursors demonstrated p-type conductivity. The annealing procedure affected the conductivity and transmittance of NiO films. The cubic phase of pure NiO films was obtained using nickel nitrate and nickel chloride as precursors, whereas $NiSO_4$ and $Ni(OH)_2$ precursors did not support the development of pure NiO films but may be helpful in solar cells and electrical devices as native electrodes (Ukoba et al., 2018).

1.5 Films Characterization

Structure, morphological, optical, and electrical characteristics are frequently used to describe thin films. This section highlights the techniques used for the study and the characterization of thin films and also focuses on the procedures utilized to evaluate material properties.

A complete characterization of thin films requires knowledge of their thickness, composition, stress state, morphology, adhesion, and degree of crystallinity, as well as whatever physical properties are germane to their operation (i.e., optical, electrical, magnetic, and mechanical). There are several available texts devoted to thin film characterization.

1.5.1 Structural properties

1.5.1.1 X-ray Diffraction (XRD)

X-ray Diffraction (XRD) is a potent method for identifying crystalline phases in materials and evaluating their structural characteristics, such as grain size, orientation, crystallization, strain state, and defect structure. The technique is also utilized to determine the thickness of films and multi-layers, as well as the atomic configurations in amorphous materials (polymers included) (Chang, 2001).

The XRD mechanism occurs when monochromatic X-rays strike a crystal sample, leading to diffraction due to interference between the X-rays and interactions with the crystal's planes. However, diffraction is only observed when Bragg's law is satisfied, as indicated by the equation.

$$n\lambda = 2d_{hkl} \sin\theta \qquad (1\text{-}1)$$

Where λ is the X-ray wavelength, n is an integer, d is the crystal's interplanar distance, hkl is the Miller indices, and θ the Bragg angle. Bragg diffraction is illustrated in Figure 1.8 (Intilla, 2016; Lalonde et al., 2010).

This technique involves directing an X-ray beam towards the sample to be examined and measuring the intensity of the refracted beam. The source of X-rays and detector rotate on a circle in opposition to one another, scanning the various angles of incident (θ) and dispersion (2θ) determined in relation to the film surface (Leber, 2018), where the nature of the crystalline structure of the films can be known by looking at the presence of diffraction peaks, their shape and intensity. Peak detection offers information on the crystal's interplanar spacing according to Bragg's law. Using diffraction patterns, the phase and crystalline structure of the films are determined based on comparison with the database file ICDD (International Center for Diffraction Data) (Roffi, 2016; Waseda et al., 2011).

The structural measurements of the deposited films in this study were performed using a diffractometer (Philips X'pert pro-2-X) Figure 1.8b, using Cu − Kα radiation with λ = 0.15406 nm. This system runs at 30 mA current and 30 kV voltage. Each sample's statement was determined according to the 2θ scan (2θ =20- 80°).

(a) **(b)**

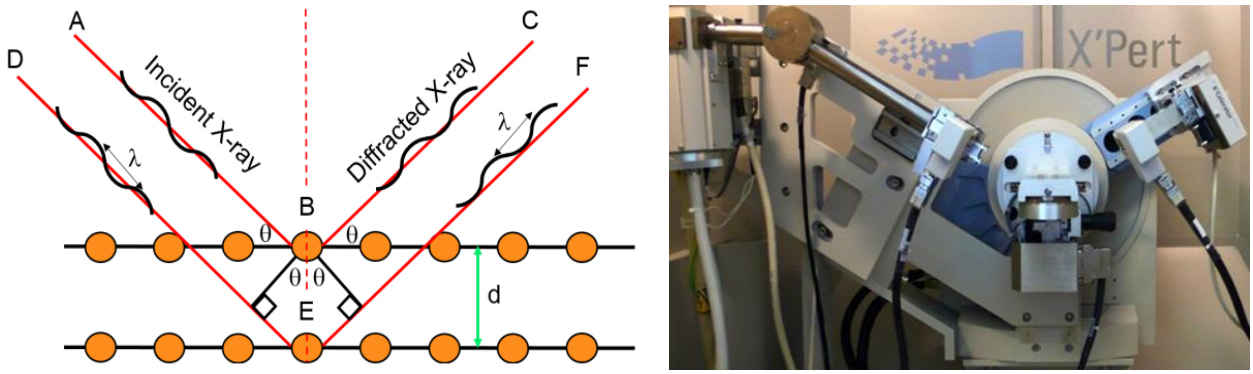

Figure 1.8. (a) Bragg diffraction (b) X-ray diffractometer (Philips X'Pert Pro) (Intilla, 2016; Mo et al., 2014**).**

1.5.1.2 Structural information using X-ray diffraction analysis

The X-ray diffraction pattern provides a range of information about the properties of the material studied, some of which will be discussed in the section below.

- **Lattice parameters**

A three-dimensional space lattice is used to create the crystal's mathematical description. The smallest volume within a lattice is referred to by the unit cell defined by the fundamental vectors (a, b, and c). The lattice atoms are depicted as dots associated with lattice planes defined by Miller indices (h k l) (Intilla, 2016; Dove, 2003).

The values of the lattice parameters for various crystal structures can be computed by the equations listed in the table 1.2 using the interplanetary distance (d) and the (hkl) parameters.

Table 1.2. Equations that link the lattice parameters, the planes (hkl) and (d_{hkl}) for crystal systems (cubic, tetragonal and hexagonal) (Dove, 2003**).**

System	mathematics equations
Cubic	$\frac{1}{d^2} = \frac{h^2 + k^2 + l^2}{a^2}$
Tetragonal	$\frac{1}{d^2} = \frac{h^2 + k^2}{a^2} + \frac{l^2}{c^2}$
Hexagonal	$\frac{1}{d^2} = \frac{4}{3}\left(\frac{h^2 + kl + k^2}{a^2}\right) + \frac{l^2}{c^2}$

- **crystallite size**

X-ray diffraction spectra are also utilized to estimate crystallite size (D), which may be computed from the full width at half maximum (FWHM), using the Scherrer equation (Hamrouni et al., 2014):

$$D = \frac{0.9\lambda}{\beta \cos(\theta)} \quad (1\text{-}2)$$

Where:

D = crystallite size

λ = X-ray wavelength

β = the width at half intensity in radian (Figure 1.9)

θ = diffraction angle.

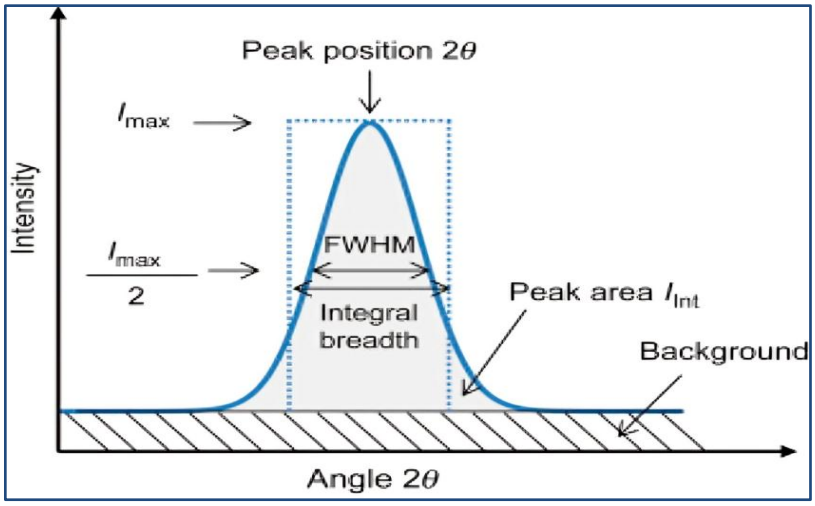

Figure 1.9. A graphic showing extraction of FWHM from the diffraction peak (Epp, 2016).

- **structural defects**

It is very unlikely that crystals will not have defects because they are created during the crystal development and growth phases. Structural defects are described as deviation and irregularity in the periodic arrangement of atoms in a crystal lattice. Moreover, there are several factors during the manufacturing process that can enhance defect density including doping content, thermal annealing, etc. (Dolabella et al., 2014). Structural defects like dislocation density and micro strain may be examined using the XRD technique. Before a material is used in technology, it is essential to understand these parameters. The dislocation density (δ) and the

lattice micro strain (ε) of the deposited films can be determined by the following relationships (Beggas, 2018):

$$\varepsilon = \frac{\beta \cos\theta}{4} \quad (1\text{-}3)$$

$$\delta = \frac{1}{D^2} \quad (1\text{-}4)$$

- **Texture Coefficient**

The texture coefficient TC (hkl) allows an evaluation of the preferred orientation of the thin films, whose difference from unity indicates the preferred growth of a given plane. The texture coefficient may be used to determine the degrees of the various crystal planes' preferred orientation based on Harris's study according to the folowing relation (Kumar et al., 2015; Babu et al., 2019):

$$TC(hkl) = \frac{I(hkl)}{I_0(hkl)} \left[\frac{1}{n}\sum_n \frac{I(hkl)}{I_0(hkl)}\right]^{-1} \quad (1\text{-}5)$$

Where:

I(hkl) : The measured intensity of a plane (hkl).

I_0(hkl) :The standard density extracted from the database ICDD for the plane (hkl).

n : The number of diffraction peaks.

1.5.2 Electrical properties

1.5.2.1 Four-Point Probe Technique

In materials science, a four-point probe characterization is a typical approach for evaluating the electrical characteristics of thin films and solids (Li et al., 2012). Because four locations on the sample surface were contacted, the device is known as a "four-point probe". These four-point probes are lined up in a straight line, with the spacing between them adjusted so that each probe has the same distance (Waremra and Betaubun, 2018) (see Figure 1.10)).

The four-point probe's fundamental mode of operation is depicted in Figure 1.10. Through the external probes, a constant current is sent along the sample. When current (I) runs through a sample with resistance, a voltage drop (V) will occur. Two inside probes are used to measure the voltage variation (Li et al., 2012). This method of determining electrical resistivity by surface

contact is frequently utilized (Panta and Subedi, 2012). The sheet resistivity may be calculated using the following relationship (Intilla, 2016):

$$\rho = \frac{\pi V}{\ln(2) I} \tag{1-6}$$

Where: $\frac{\pi}{ln(2)} = 4.523$.

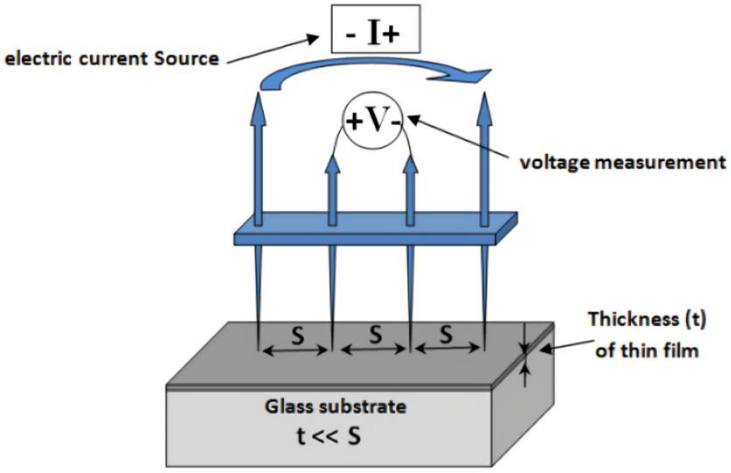

Figure 1.10 . Diagram of a four-point probe (Ghougali, 2019).

By modifying the preceding equation for thin films, the formula below can be used to determine the film's resistivity (ρ) when its length is substantially greater than its thickness (d) (Panta and Subedi, 2012).

$$\rho = \frac{\pi}{\ln(2)} d \frac{V}{I} \approx 4.523\ d\ \frac{V}{I} \tag{1-7}$$

Where I is the electric current in (mA), V is the voltage and d is the film thickness. The films' electrical conductivity may be determined by the relation as follows (Panta and Subedi, 2012):

$$\sigma = \frac{1}{\rho} \tag{1- 8}$$

1.5.2.2 Hall Effect

To comprehend semiconductor electrical characteristics that depend on the characterization of semiconducting materials' transport using a combination of resistivity and Hall effect studies (Orton and Powell, 1980). The use of a magnetic field perpendicular to the

direction of current flow through a conductor or semiconductor creates a transverse voltage known as the Hall voltage, and the phenomenon is known as the Hall effect (see Figure 1.11). This approach is based on "Lorentz Force", a physics concept defined as the force applied to a point charge as a result of an electromagnetic field. In fact, a number of material parameters may be determined using a Hall effect measuring device, but the Hall voltage is the most important one. In addition to other measurements like carrier concentration, carrier mobility, conduction type (n/p) and Hall coefficient (RH) (Remadevi et al., 2018; Intilla, 2016).

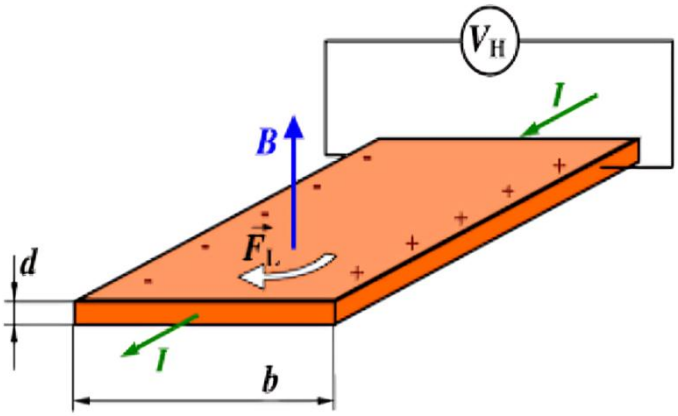

Figure 1.11. Diagrammatic arrangement for measuring the Hall effect (Nair et al., 2012).

The electrons are directed toward the specimen's edge according to the Lorentz force due to the application of magnetic field B in a manner that is perpendicular to the current's flow, which causes a voltage drop. This voltage drop is referred to as a "Hall voltage (V_H)", and is affected by the magnetic field B, sample thickness d and the current I. The relationship can be described as follows (Intilla, 2016; Nair et al., 2012):

$$V_H = \frac{1}{nq}\frac{I}{d}B = R_H\frac{I}{d}B \qquad (1 - 9)$$

Where: $R_H = 1/nq$ (Hall coefficient).

q is the charge and n is the carrier concentration.

Once the Hall potential V_H has been determined, the carrier concentration can also be estimated by (Nair et al., 2012):

$$n = \frac{1}{R_H q} \qquad (1\text{-}10)$$

The mobility (μ) is a gauge of how quickly a carrier in a medium and is determined by (Intilla, 2016):

$$\mu = \frac{R_H}{\rho} \qquad (1\text{- }11)$$

Where ρ is the resistivity.

1.5.3 Optical Properties

1.5.3.1 UV-visible spectroscopy

Optical properties provide in-depth knowledge about the nature of materials in anticipation of their use in many modern applications, so it has become necessary to study and analyze these properties. In order to investigate the material's optical properties such as the absorbance, transmittance, energy gap, refractive index, etc. (Boukhari, 2022). UV-visible spectrophotometry is a technique applied in optical characterization. Absorption of UV and visible light upon impact on a sample is the basis for UV/VIS spectroscopy and refers to the interaction between matter and electromagnetic radiation. (Leber, 2018).

The interaction between ultraviolet and visible light with the sample's surface occurs where the photon energy induces the semiconductor electrons in the valence band to transition to the conduction band. An electron is excited when the frequency of the incoming radiation matches the energy differential between two states of an electronic system. The electronic structure of the studied molecule determines this energy (Picollo et al., 2018). Incident radiation photons with energies equal to or greater than the bandgap energy ($h\nu \geq Eg$) are absorbed. The absorption is determined by the properties of the film, such as film thickness and impurities since there are numerous valence band electrons, and the conduction band contains many empty states into which these electrons can be excited. Incident radiation photons with energies less than the bandgap energy ($h\nu < Eg$) are unable to excite a valence band electron to the conduction band, and as consequence they are transmitted, this explains why some semiconductors are transparent in certain wavelength ranges. Thus, for pure (intrinsic) semiconductors. There is negligible absorption of photons with ($h\nu < Eg$), a photon will be absorbed only if there are available energy states in the forbidden band gap due to chemical impurities or physical defects, this process is called extrinsic transition (Beggas, 2018).

UV-Vis spectroscopy offers much information on the characteristics of materials as they interact with incident radiation (electromagnetic). When an electromagnetic radiation is incident

on a material, there is some predictable absorption, determined by the properties of the material. There is a dependence of the ratio of transmitted to incident photon intensity that depends on the thickness of the material and photon wavelength. This dependence can be expressed by the Lambert-Beer- Bouguer formula (Beggas, 2018; Ezekoye and Okeke, 2006):

$$I = I_0 \exp(-\alpha d) \tag{1- 12}$$

Where, I_0 is the initial light intensity, I is the light intensity at a distance (d) inside the sample, (α) is a coefficient that represents the decrease in the intensity of a light beam as it travels through a medium and is known as the absorption (or attenuation) coefficient, which can be obtained through the relation (Ghougali, 2019; Sagadevan and Podder, 2015) :

$$\alpha = -\frac{\ln(I/I_0)}{d} \tag{1- 13}$$

For hv < Eg (direct), no electron hole pairs can be created, the material is transparent and (α) is small. For hv ≥ Eg (direct), absorption should be strong and it is clear that (α) must be strong. The absorption coefficient (α) is related to the incident photon energy hv and the band gap Eg of the material as:

$$\alpha = \frac{A(hv-Eg)^{n/2}}{hv} \tag{1-14}$$

Where A is a constant, Eg is the optical band gap.

UV-Vis spectra of the samples obtained by a spectrophotometer (Shimadzu, UV-1800) available at VTRS Laboratory, El Oued University, in the wavelength range between 300-900 nm (Figure 1.12a). All spectra were measured by placing the samples in the holder attached to the device. The UV/Vis spectrometer equipment schematic diagram is shown in (Figure 1.12b). The visible wavelengths are produced by a halogen lamp, while the UV wavelengths are produced by a tungsten filament. Mirrors are used to monochromatize the light after it has passed through the filters. After that, two beams of monochromatic light are created, one of which passes through the sample and the other via the reference cell. Finally, a detector is used to gather the sample's emitted light. The detector turns light into an electrical signal to produce a spectrogram versus wavelength (Leber, 2018).

(a) **(b)**

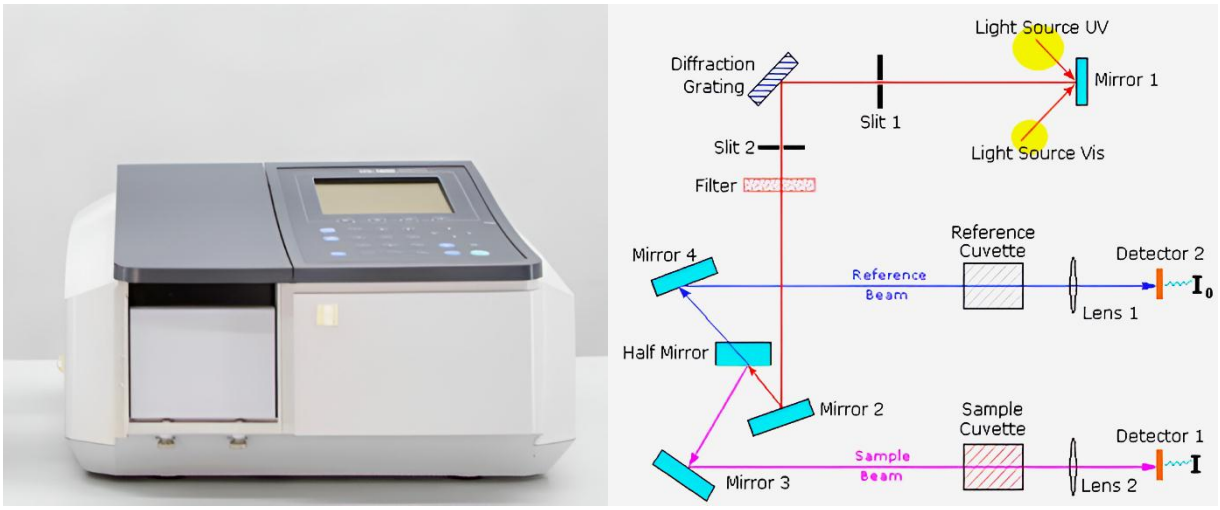

Figure 1.12. (a) Shimadzu UV-1800 spectrophotometer and (b) Illustration diagram of UV-Vis set u (Boukhari, 2022)

1.5.3.2 Optical band gap energy

One of the essential properties of optical materials is the band gap energy (E_g). The band gap refers to the energy difference (often expressed in electron-volts) between the top of the valence band and the bottom of the conduction band in insulators and semiconductors . It is well known that a semiconductor material's band gap can only ever be direct or indirect (Ahrenkiel and Johnston, 1998). As seen in Figure 1.13 the minimal-energy state in the conduction band and the maximal-energy state in the valence band are each characterized by a certain crystal momentum (k-vector) in the Brillouin zone. If the k-vectors are different, the material has an "indirect gap". The band gap is called "direct" if the crystal momentum of electrons and holes is the same in both the conduction band and the valence band; an electron can directly emit a photon. In an "indirect" gap, a photon cannot be emitted because the electron must pass through an intermediate state and transfer momentum to the crystal lattice (Garrillo, 2018).

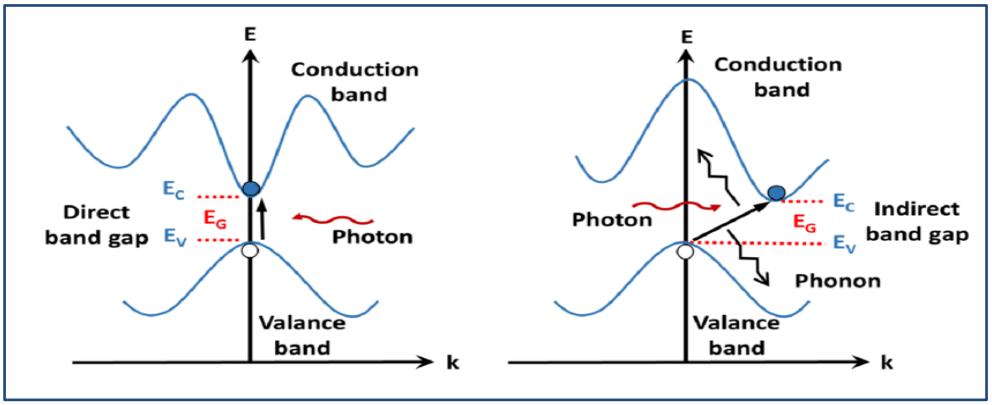

Figure 1.13. Scheme showing the indirect (right) and direct (left) bandgap (Garrillo, 2018).

The band gap energy (of the forbidden energy zone) can be estimated from the mathematical study of measurements obtained with a UV-Vis spectrophotometer according to Tauc's formula (Tauc et al., 1966) :

$$\alpha h\vartheta = A\left(h\vartheta - E_g\right)^m \qquad (1\text{- }15)$$

Where α is absorption coefficient, hϑ is the energy of photons (h is Planck's constant and ϑ is incident photon frequency), A is constant, E_g is the band gap, and (m) represents the transition type. The value of m is 1/2 and 2 for direct allowed and indirect allowed band gap transition, respectively. Also, m = 3/2 for direct forbidden transitions and m = 3 for indirect forbidden transitions. The determination of band gap energy by using Tauc plot is done by plotting the value of the $(\alpha h\upsilon)^2$ versus (hυ), then taking the extrapolation in the linear area across the energy axis in the corresponding curve. The intersection with energy-axis is the estimation of the corresponding energy gap as shown in the Figure 1.14 (Mishra et al., 2011).

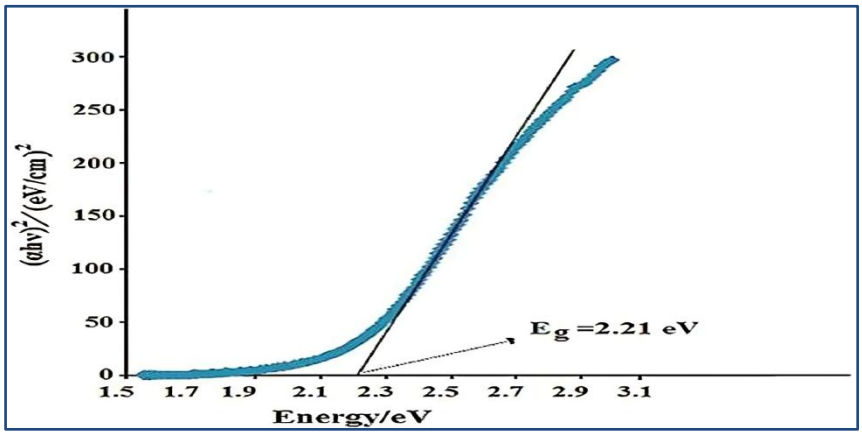

Figure 1.14. Extract the energy bandgap (E_g) from the graph of $(\alpha h\nu)^2$ vs (hν) (Tadjarodi et al., 2013).

1.5.3.3 Urbach energy

Impurity insertion into semiconductors frequently displays the appearance of band tails in the bandgap results of the emergence of localized states (Mrabet et al., 2016). These defect states provide absorption up to the depth of the forbidden range, which establishes a band tail from below the conduction band to the depth of the bandgap. Likewise, defect states close to the valence band stretch the valence band edge into the gap. Therefore, an energy tail forms on either side of the conduction band minimum and valence band maximum, which relates to the disorder of matter (Borah and Mohanta, 2012; Parida et al., 2015). This tail is called the Urbach tail, and the energy is known as Urbach energy. The Urbach energy formula is given by (Choudhury and Choudhury, 2014; Parida et al., 2015):

$$\alpha = \alpha_0 \exp\left(\frac{h\vartheta}{E_u}\right) \quad (1\text{- }16)$$

Where (E_u) is the Urbach energy and (α_0) is a constant. The Urbach energy can be determined by the opposite slope of the linear part of ln (α) vs. (hv). The band states formed between the conduction and valence bands are known to narrow the band gap. The band gap is known to be narrowed by the band states that occur between the conduction and valence bands. This demonstrates that there is a link between the Urbach energy and the band gap energy since the band gap energy value rises as the Urbach energy value falls (Parida et al., 2015; Ali et al., 2017). Figure 1.15 provide schematic illustrations of the Urbach tail and the relation between Urbach energy and bandgap for various samples.

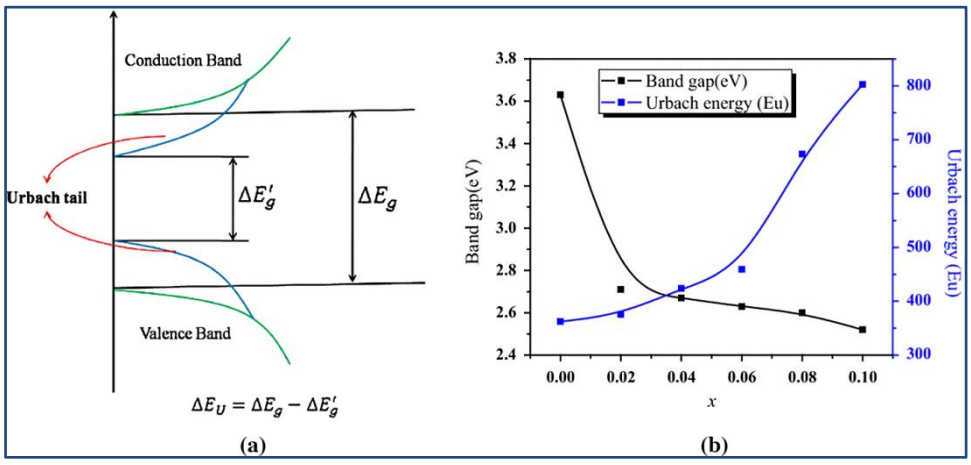

Figure 1.15. (a) Scheme showing the formation of the Urbach tail and (b) Changes in bandgap and Urbach energy with different samples (Parida et al., 2015).

1.5.4 Scanning Electron Microscopy (SEM)

The scanning electron microscope (SEM) is a very flexible tool for studying and evaluating chemical compositions, morphology, and microstructures of a sample. By exploiting the interaction between beam of electrons and the material surface to produce a high-resolution topological image. Electron microscopy enables the imaging of a specimen's surface. Researchers may view stuff with greater detail with electron microscopy than they can using a light microscope because of its higher magnification compared to a light microscope. This non-destructive method offers important insights into sample shape, crystallization mode, crystallite size estimate, and sample thickness from cross-sectional views (Abd Mutalib et al., 2017).

Images are created by the scanning electron microscope (SEM) by detecting signals caused by interactions between electron signals and scanned material. Elastic and inelastic interactions can be used to categorize these interactions. Low-energy secondary electrons (SEs) are released as a result of the primary beam electrons' energy being transferred to the sample's atoms during inelastic interactions. Elastic interactions happen when the main electrons are deflected when they come into contact with an atomic nucleus or other electrons in the sample with a comparable energy. Imaging of the material can be done using backscattered electrons (BSEs), which are dispersed at angles larger than 90 degrees. The interaction of the electron beam with the material results in other signals in addition to imaging signals, such as recognizable x-rays and Auger electrons. These interactions and signal generation processes are depicted in Figure 1.16 (Abd Mutalib et al., 2017; Aharinejad et al., 1992).

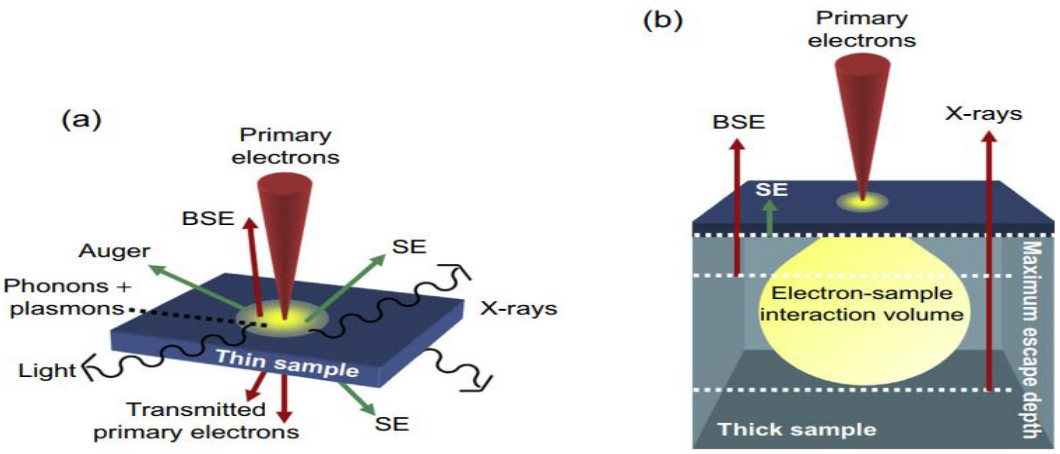

Figure 1.16. Electron Interaction with Sample. (a) The signals generated by the interaction of the electron beam with the sample. (b) a diagram showing the volume of the subsurface electron interaction (Inkson, 2016).

A common method for examining specimen surfaces is the scanning electron microscope (SEM). The usual design of a SEM is seen in Figure 1.17. It has a number of parts, including an electron cannon, electromagnetic lenses for electron focusing, a vacuum chamber with a specimen stage, and detectors to gather emitted signals. Secondary electron (SE) detectors, backscattered electron (BSE) detectors, and X-ray spectrometers are frequently found in SEMs. The SEMs imaging modes and application possibilities are controlled by these detectors. Figure 1.17b, shows a full SEM apparatus (Inkson, 2016).

(a) **(b)**

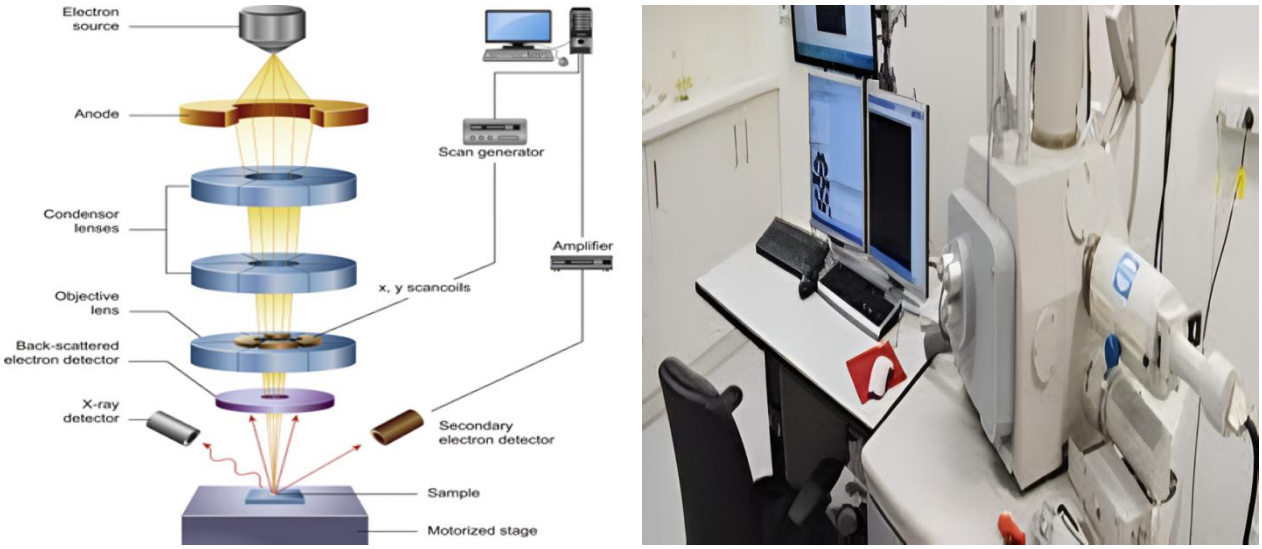

Figure 1.17. Scanning electron microscopy. (a) a schematic showing the essential elements of a SEM microscope. (b) SEM device (Inkson, 2016)

1.5.5 Photoluminescence spectroscopy (PL)

Photoluminescence is a versatile, non-destructive spectroscopy technique for examining the electronic structure of a studied sample. This method involves analyzing the energy distribution of photons that have released following the optical stimulation. Absorption of a photon by a substance pushes electrons to be excited and transition to a greater energy level. When the electron returns to a lower energy level, the energy of the emitted photon will be different than that of the incident photon. The energy of the emitted photon is proportional to the electron energy levels. Typically, a laser is used to excite the sample, and after that, a Rayleigh filter is used to focus the dispersed light. Then, the intensity of the generated spectra is

determined on the detector after being transmitted through a monochromator (Gilliland, 1997; Evans, 2020).

A multitude of parameters, including the band gap, the existence of defects or impurities, and the recombination processes, may be identified via photoluminescence spectroscopy. A simplified representation of the photoluminescence mechanisms is shown in Figure 1.18.

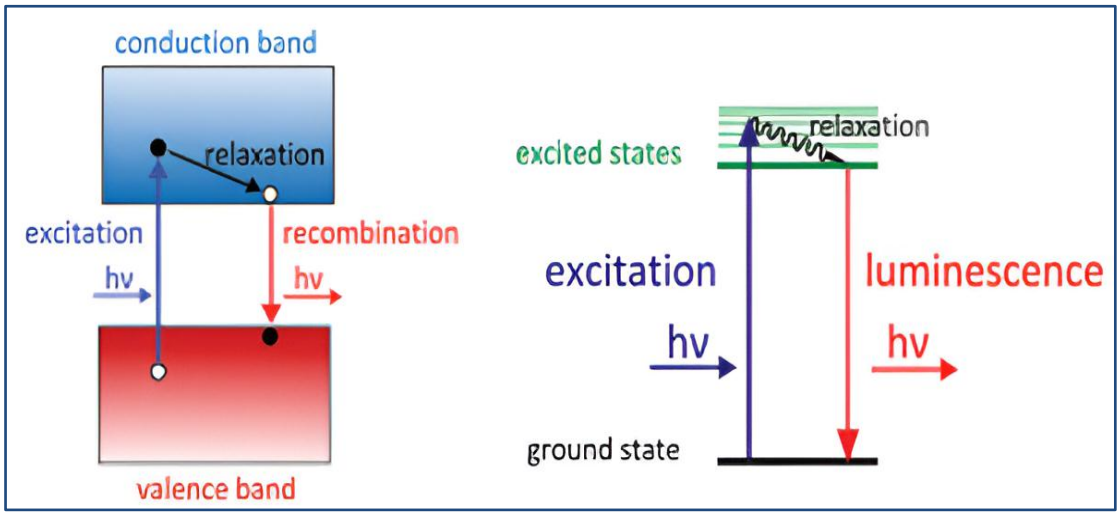

Figure 1.18. Diagram illustrates the phenomena of photoluminescence (Heine and Müller-Buschbaum, 2013**).**

The photoluminescence of a sample is measured and recorded using an analytical tool called a spectrofluorometer (Figure 1.19b). The device uses a continuous light source, which is a xenon lamp with a capacity of 150 w. A mirror collects the lamp's light, which then is focused on the entry slit of the excitation monochromator. The outgoing beam is divided by a semi-transparent blade (Beam splitter), with one half reflecting to a control detector and the other part interacts with the sample. The monochromator receives the luminescence radiation generated by the latter, and the photomultiplier measures the related intensity value. Finally, the data is collected and displayed using a computer system (Vallikkodi, 2018; Boukhari, 2022).

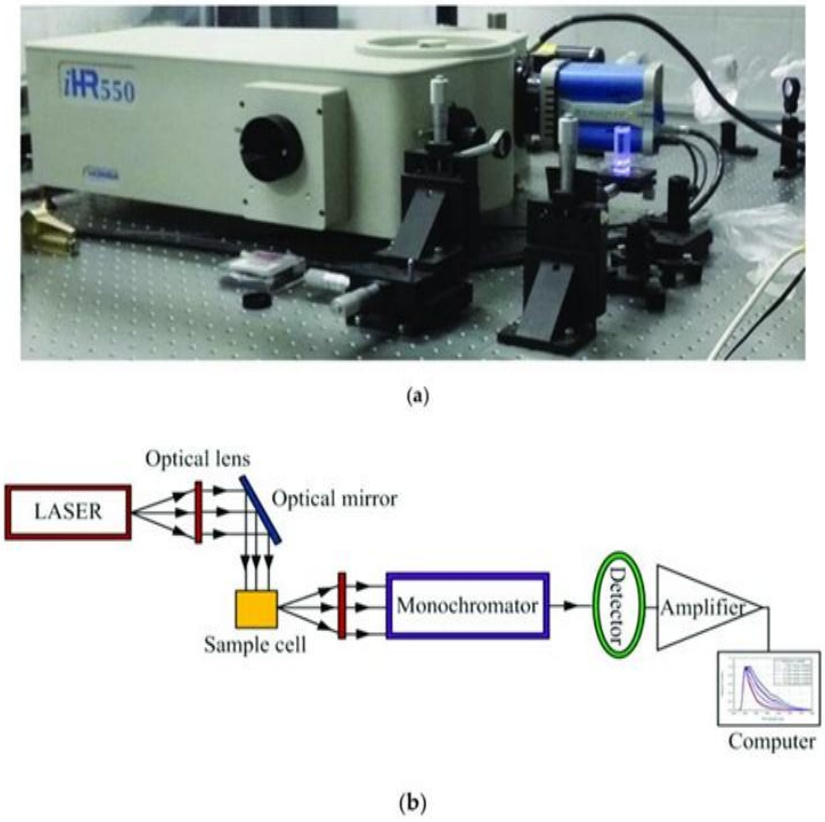

Figure 1.19. Photoluminescence spectroscopy experimental setup : (a) PL spectrometer setup and (b) Diagrammatic representation of the photoluminescence system (Alshehawy et al., 2021**)**

1.6 Conclusion

In this chapter, we delineated the concept of thin films, elaborating on several methods for their preparation, with a particular focus on the spray pyrolysis method. Following this, we outlined the devices utilized for studying the properties of the prepared films. It is widely recognized that nonlinear optical properties play a pivotal role in determining the electronic characteristics of semiconductor materials, making them a crucial parameter for device design. To address this aspect comprehensively, the next chapter will offer a detailed overview of nonlinear optical materials (NLO) and their classification. Furthermore, we will highlight the nonlinear optical phenomena and the associated processes.

References

Abd Mutalib, M., Rahman, M. A., Othman, M. H. D., Ismail, A. F., & Jaafar, J. (2017). Scanning electron microscopy (SEM) and energy-dispersive X-ray (EDX) spectroscopy. In Membrane characterization (pp. 161-179). Elsevier. https://doi.org/10.1016/B978-0-444-63776-5.00009-7

Aharinejad, S. H., Lametschwandtner, A., Aharinejad, S. H., & Lametschwandtner, A. (1992). Fundamentals of scanning electron microscopy. Microvascular Corrosion Casting in Scanning Electron Microscopy: Techniques and Applications, 44-51. https://doi.org/10.1007/978-3-7091-9230-6_3

Ahrenkiel, R. K., & Johnston, S. (1998). Contactless measurement of recombination lifetime in photovoltaic materials. Solar Energy Materials and Solar Cells, 55(1-2), 59-73. https://doi.org/10.1016/S0927-0248(98)00047-6

Akl, A. A. (2010). Thermal annealing effect on the crystallization and optical dispersion of sprayed V2O5 thin films. Journal of Physics and Chemistry of Solids, 71(3), 223-229. https://doi.org/10.1016/j.jpcs.2009.11.009

Akl, A. A., Mahmoud, S. A., Al-Shomar, S. M., & Hassanien, A. S. (2018). Improving microstructural properties and minimizing crystal imperfections of nanocrystalline Cu2O thin films of different solution molarities for solar cell applications. Materials Science in Semiconductor Processing, 74, 183-192. https://doi.org/10.1007/s00339-018-2180-6

Ali, D., Butt, M. Z., Muneer, I., Bashir, F., & Saleem, M. (2017). Correlation between structural and optoelectronic properties of tin doped indium oxide thin films. Optik, 128, 235-246. https://doi.org/10.1016/j.ijleo.2016.10.028

Alshehawy, A. M., Mansour, D. E. A., Ghali, M., Lehtonen, M., & Darwish, M. M. (2021). Photoluminescence spectroscopy measurements for effective condition assessment of transformer insulating oil. Processes, 9(5), 732. http://dx.doi.org/10.3390/pr9050732

Babu, M. H., Dev, B. C., & Podder, J. (2019). Texture coefficient and band gap tailoring of Fe-doped SnO 2 nanoparticles via thermal spray pyrolysis. Rare Metals, 1-10. . https://doi.org/10.1007/s12598-019-01278-3

Banerjee, A. N., & Chattopadhyay, K. K. (2005). Recent developments in the emerging field of crystalline p-type transparent conducting oxide thin films. Progress in Crystal Growth and Characterization of materials, 50(1-3), 52-105. https://doi.org/10.1016/j.pcrysgrow.2005.10.001

Bedia, A., Bedia, F. Z., Aillerie, M., Maloufi, N., & Benyoucef, B. (2015). Morphological and optical properties of ZnO thin films prepared by spray pyrolysis on glass substrates at various temperatures for integration in solar cell. Energy Procedia, 74, 529-538. https://doi.org/10.1016/j.egypro.2015.07.740

Beggas, A. (2018). Elaboration and characterization of chalcogenide thin films by chemical bath deposition technique (Doctoral dissertation, Universite Mohamed Khider Biskra). http://thesis.univ-biskra.dz/id/eprint/3825

Borah, M., & Mohanta, D. (2012). Structural and optoelectronic properties of Eu^{2+}-doped nanoscale barium titanates of pseudo-cubic form. Journal of Applied Physics, 112(12), 124321. https://doi.org/10.1063/1.4770492

Bouaichi, F. (2019). Deposition and analysis of Zinc Oxide thin films elaborated using spray pyrolysis for photovoltaic applications (Doctoral dissertation, University Mohamed Khider of Biskra). http://thesis.univ-biskra.dz/id/eprint/4533

Boukhari, A. (2022). Elaboration, characterization and modeling of oxide-based nanostructured thin films (Doctoral dissertation, Université de M'sila). http://dspace.univ-msila.dz:8080//xmlui/handle/123456789/27640

Cattin, L., Reguig, B. A., Khelil, A., Morsli, M., Benchouk, K., & Bernede, J. C. (2008). Properties of NiO thin films deposited by chemical spray pyrolysis using different precursor solutions. Applied Surface Science, 254(18), 5814-5821. https://doi.org/10.1016/j.apsusc.2008.03.071

Chamberlin, R. R., & Skarman, J. S. (1966). Chemical spray deposition process for inorganic films. Journal of the Electrochemical Society, 113(1), 86. https://doi.org/10.1149/1.2423871

Chang, S. L. (2001). Thin-film characterization by grazing incidence X-ray diffraction and multiple beam interference. Journal of Physics and Chemistry of Solids, 62(9-10), 1765-1775. https://doi.org/10.1016/S0022-3697(01)00109-3

Chavillon, B. (2011). Synthèse et caractérisation d'oxydes transparents conducteurs de type p pour application en cellules solaires à colorant (Doctoral dissertation, Université de Nantes). https://theses.hal.science/tel-00674543

Chen, Y., Sakata, O., Yamauchi, R., Yang, A., Kumara, L. S. R., Song, C., Palina, N., Taguchi, M., Ina, T., Katsuya, Y., Daimon, H., Matsuda, A., & Yoshimoto, M. (2017). Lattice distortion and electronic structure of magnesium-doped nickel oxide epitaxial thin films. Physical Review B, 95(24), 245301. https://doi.org/10.1103/PhysRevB.95.245301

Chen, Y., Sun, Y., Dai, X., Zhang, B., Ye, Z., Wang, M., & Wu, H. (2015). Tunable electrical properties of NiO thin films and p-type thin-film transistors. Thin Solid Films, 592, 195-199. https://doi.org/10.1016/j.tsf.2015.09.025

Chopra, K. L., Paulson, P. D., & Dutta, V. (2004). Thin-film solar cells: an overview. Progress in Photovoltaics: Research and applications, 12(2-3), 69-92. https://doi.org/10.1002/pip.541

Choudhury, B., & Choudhury, A. (2014). Oxygen defect dependent variation of band gap, Urbach energy and luminescence property of anatase, anatase–rutile mixed phase and of rutile phases of TiO_2 nanoparticles. Physica E: Low-Dimensional Systems and Nanostructures, 56, 364-371. https://doi.org/10.1016/j.physe.2013.10.014

Diha, A., Benramache, S., & Benhaoua, B. (2018). Transparent nanostructured Co doped NiO thin films deposited by sol–gel technique. Optik, 172, 832-839. https://doi.org/10.1016/j.ijleo.2018.07.062

Dolabella, S., Borzì, A., Dommann, A., & Neels, A. (2022). Lattice strain and defects analysis in nanostructured semiconductor materials and devices by high-resolution X-ray diffraction: theoretical and practical aspects. Small Methods, 6(2), 2100932. . https://doi.org/10.1002/smtd.202100932

Dove, M. T. (2003). Structure and dynamics: an atomic view of materials (Vol. 1). Oxford University Press. http://dx.doi.org/10.1016/S1369-7021(03)00639-4

Epp, J. (2016). X-ray diffraction (XRD) techniques for materials characterization. In Materials characterization using nondestructive evaluation (NDE) methods (pp. 81-124). Woodhead Publishing. https://doi.org/10.1016/B978-0-08-100040-3.00004-3

Evans, S. (2020). Growth, Optical Properties and Applications of Thin Film Diamond (Doctoral dissertation, UCL (University College London)). https://discovery.ucl.ac.uk/id/eprint/10101998

Ezekoye, B. A., & Okeke, C. E. (2006). Optical Properties in PbHgS Ternary Thin Films Deposited by Solution Growth Method. http://www.akamaiuniversity.us/PJST.htm

Falcony, C., Aguilar-Frutis, M. A., & García-Hipólito, M. (2018). Spray pyrolysis technique; high-K dielectric films and luminescent materials: a review. Micromachines, 9(8), 414. https://doi.org/10.3390/mi9080414

Garrillo, P. A. F. (2018). Development of highly resolved and photo-modulated Kelvin probe microscopy techniques for the study of photovoltaic systems (Doctoral dissertation, Université Grenoble Alpes). https://theses.hal.science/tel-01970171

Geremew, T. (2022). Thin film deposition and characterization techniques. J. 3D Print. Appl, 1, 1-24. https://doi.org/10.14302/issn.2831-8846.j3dpa-22-4066

Ghougali, M. (2019). Elaboration and characterization of nanostructuring NiO thin films for gas sensing applications (Doctoral dissertation, University of Mohamed Khider, Biskra). http://thesis.univ-biskra.dz/id/eprint/4617.

Gilliland, G. D. (1997). Photoluminescence spectroscopy of crystalline semiconductors. Materials Science and Engineering: R: Reports, 18(3-6), 99-399. https://doi.org/10.1016/S0927-796X(97)80003-4

Hamrouni, A., Moussa, N., Parrino, F., Di Paola, A., Houas, A., & Palmisano, L. (2014). Sol–gel synthesis and photocatalytic activity of ZnO–SnO2 nanocomposites. Journal of Molecular Catalysis A: Chemical, 390, 133-141. https://doi.org/10.1016/j.molcata.2014.03.018

Hassanien, A. S., & Akl, A. A. (2018). Optical characteristics of iron oxide thin films prepared by spray pyrolysis technique at different substrate temperatures. Applied Physics A, 124(11), 752. https://doi.org/10.1007/s00339-018-2180-6

Heine, J., & Müller-Buschbaum, K. (2013). Engineering metal-based luminescence in coordination polymers and metal–organic frameworks. Chemical Society Reviews, 42(24), 9232-9242. https://doi.org/10.1039/C3CS60232J

Inkson, B. J. (2016). Scanning electron microscopy (SEM) and transmission electron microscopy (TEM) for materials characterization. In Materials characterization using nondestructive evaluation (NDE) methods (pp. 17-43). Woodhead publishing. https://doi.org/10.1016/B978-0-08-100040-3.00002-X

Intilla, L. (2016). Study of ZnO properties applied to thin film transistors (Doctoral dissertation, UCL (University College London)). https://discovery.ucl.ac.uk/id/eprint/1530069

Kawazoe, H., Yanagi, H., Ueda, K., & Hosono, H. (2000). Transparent p-type conducting oxides: design and fabrication of pn heterojunctions. Mrs Bulletin, 25(8), 28-36. https://doi.org/10.1557/mrs2000.148

Kumar, M., Kumar, A., & Abhyankar, A. C. (2015). Influence of texture coefficient on surface morphology and sensing properties of W-doped nanocrystalline tin oxide thin films. ACS applied materials & interfaces, 7(6), 3571-3580. https://doi.org/10.1021/am507397z

Kunz, A. B. (1981). Electronic structure of NiO. Journal of Physics C: Solid State Physics, 14(16), L455. https://doi.org/10.1088/0022-3719/14/16/001

Lalonde, S. V., Dafoe, L. T., Pemberton, S. G., Gingras, M. K., & Konhauser, K. O. (2010). Investigating the geochemical impact of burrowing animals: Proton and cadmium adsorption onto the mucus lining of Terebellid polychaete worms. Chemical Geology, 271(1-2), 44-51. https://doi.org/10.1016/j.chemgeo.2009.12.010

Leber, R. (2018). Growth and Characterisation of Metallocene Based Thin Films for Spintronic Applications (Doctoral dissertation, UCL (University College London)). https://discovery.ucl.ac.uk/id/eprint/10056153

Li, J. C., Wang, Y., & Ba, D. C. (2012). Characterization of semiconductor surface conductivity by using microscopic four-point probe technique. Physics Procedia, 32, 347-355. https://doi.org/10.1016/j.phpro.2012.03.568

Li, Y. T., Han, C. F., & Lin, J. F. (2019). Characterization of the electrical and optical properties for a-IGZO/Ag/a-IGZO triple-layer thin films with different thickness depositions on a curved glass substrate. Optical Materials Express, 9(8), 3414-3431. https://doi.org/10.1364/OME.9.003414

Makhlouf, S. A. (2008). Electrical properties of NiO films obtained by high-temperature oxidation of nickel. Thin Solid Films, 516(10), 3112-3116. https://doi.org/10.1016/j.tsf.2007.07.213

Manjunatha, K. N., & Paul, S. (2015). Investigation of optical properties of nickel oxide thin films deposited on different substrates. Applied Surface Science, 352, 10-15. https://doi.org/10.1016/j.apsusc.2015.03.092

Manzi, J. A. (2016). Zinc Precursor Synthesis and the Aerosol Assisted Chemical Vapour Deposition of Zinc Oxide Thin Films (Doctoral dissertation, UCL (University College London)). https://discovery.ucl.ac.uk/id/eprint/1474036

Marinov, G., Strijkova, V., Vasileva, M., Madjarova, V., Malinowski, N., & Babeva, T. (2018). Effect of substrate temperature on the microstructural, morphological, and optical properties of electrosprayed ZnO thin films. Advances in Condensed Matter Physics, 2018. https://doi.org/10.1155/2018/8957507

Martínez-Bautista, R., Fernández-Valverde, S. M., Tejeda-Cruz, A., & Chávez-Carvayar, J. A. (2019). Structural, morphological and electrical characterization of ceria-based nanostructured thin films obtained by ultrasonic spray pyrolysis. Boletín de la Sociedad Española de Cerámica y Vidrio, 58(1), 38-47. https://doi.org/10.1016/j.bsecv.2018.06.004

Mishra, M., Kuppusami, P., Sairam, T. N., Singh, A., & Mohandas, E. (2011). Effect of substrate temperature and oxygen partial pressure on microstructure and optical properties of pulsed laser deposited yttrium oxide thin films. Applied surface science, 257(17), 7665-7670. https://doi.org/10.1016/j.apsusc.2011.03.156

Mitridis, S. (2008). Determination of lattice site location of impurities in compound semiconductors, by transmission electron microscopy. Physics of Advanced Materials Winter School, 2008(1). https://www.researchgate.net/publication/274719826

Mo, J., Steen, S. M., & Zhang, F. Y. (2014). X-Ray Diffraction Studies on Material Corrosions in Renewable Energy Storage Electrolyzers. In Journal of Physics: Conference Series (Vol. 548, No. 1, p. 012061). IOP Publishing. http://dx.doi.org/10.1088/1742-6596/548/1/012061

Mrabet, C., Amor, M. B., Boukhachem, A., Amlouk, M., & Manoubi, T. (2016). Physical properties of La-doped NiO sprayed thin films for optoelectronic and sensor applications. Ceramics International, 42(5), 5963-5978. https://doi.org/10.1016/j.ceramint.2015.12.144

Mwakikunga, B. W. (2014). Progress in ultrasonic spray pyrolysis for condensed matter sciences developed from ultrasonic nebulization theories since michael faraday. Critical reviews in solid state and materials sciences, 39(1), 46-80. https://doi.org/10.1080/10408436.2012.687359

Nair, S., Wirth, S., Friedemann, S., Steglich, F., Si, Q., & Schofield, A. J. (2012). Hall effect in heavy fermion metals. Advances in Physics, 61(5), 583-664. https://doi.org/10.1080/00018732.2012.730223

Orton, J. W., & Powell, M. J. (1980). The Hall effect in polycrystalline and powdered semiconductors. Reports on Progress in Physics, 43(11), 1263. http://dx.doi.org/10.1088/0034-4885/43/11/001

Panta, G. P., & Subedi, D. P. (2012). Electrical characterization of aluminum (Al) thin films measured by using four-point probe method. Kathmandu University journal of science, Engineering and technology, 8(2), 31-36. https://doi.org/10.3126/kuset.v8i2.7322

Parida, S., Satapathy, A., Sinha, E., Bisen, A., & Rout, S. K. (2015). Effect of neodymium on optical bandgap and microwave dielectric properties of barium zirconate ceramic. Metallurgical and Materials Transactions A, 46(3), 1277-1286. https://doi.org/10.1007/s11661-014-2725-z

Perednis, D., & Gauckler, L. J. (2005). Thin film deposition using spray pyrolysis. Journal of electroceramics, 14, 103-111. https://doi.org/10.1007/s10832-005-0870-x

Picollo, M., Aceto, M., & Vitorino, T. (2018). UV-Vis spectroscopy. Physical sciences reviews, 4(4), 20180008. https://doi.org/10.1515/psr-2018-0008

Piriyawong, V., Thongpool, V., Asanithi, P., & Limsuwan, P. (2012). Preparation and characterization of alumina nanoparticles in deionized water using laser ablation technique. Journal of Nanomaterials, 2012, 1-6. https://doi.org/10.1155/2012/819403

Powell, R. J., & Spicer, W. E. (1970). Optical properties of NiO and CoO. Physical Review B, 2(6), 2182. https://doi.org/10.1103/PhysRevB.2.2182

Purica, M., Budianu, E., Rusu, E., Danila, M. A., & Gavrila, R. (2002). Optical and structural investigation of ZnO thin films prepared by chemical vapor deposition (CVD). Thin Solid Films, 403, 485-488. https://doi.org/10.1016/S0040-6090(01)01544-9

Rahal, A. (2017). Optimisation des conditions opératoires des couches minces de SnO_2 élaborées par ultra son (Doctoral dissertation, Université Mohamed Khider-Biskra). http://thesis.univ-biskra.dz/id/eprint/2997

Remadevi, A., Kesavapillai Sreedeviamma, D., & Surendran, K. P. (2018). Printable hierarchical nickel nanowires for soft magnetic applications. ACS omega, 3(10), 14245-14257. https://doi.org/10.1021/acsomega.8b01422

Roffi, T. M. (2016). Development of Metal Organic Vapor Phase Epitaxy for the Growth of Single Crystal NiO and Its Characterization (Doctoral dissertation, The University of Electro-Communications). https://ci.nii.ac.jp/naid/500000984333/

Sagadevan, S., & Podder, J. (2015). Optical and electrical properties of nanocrystalline SnO2 thin films synthesized by chemical bath deposition method. http://dx.doi.org/10.4236/snl.2015.54007

Shimanovich, K. (2015). Combinatorial approach for development of new metal oxides materials for all oxide photovoltaics. arXiv preprint arXiv:1508.04626. https://doi.org/10.48550/arXiv.1508.04626

Tadjarodi, A., Imani, M., & Kerdari, H. (2013). Application of a facile solid-state process to synthesize the CdO spherical nanoparticles. International Nano Letters, 3(1), 1-6. https://doi.org/10.1186/2228-5326-3-43

Taeño González, M., Maestre Varea, D., & Cremades Rodríguez, A. I. (2022). An approach to emerging optical and optoelectronic applications based on NiO micro-and nanostructures. Ene, 12, 25. https://doi.org/10.1515/nanoph-2021-0041

Taeño, M., Maestre, D., & Cremades, A. (2021). An approach to emerging optical and optoelectronic applications based on NiO micro-and nanostructures. Nanophotonics, 10(7), 1785-1799. https://doi.org/10.1515/nanoph-2021-0041

Talebian, N., & Kheiri, M. (2014). Sol–gel derived nanostructured nickel oxide films: effect of solvent on crystallographic orientations. Solid state sciences, 27, 79-83. https://doi.org/10.1016/j.solidstatesciences.2013.11.010

Tauc, J., Grigorovici, R., & Vancu, A. (1966). Optical properties and electronic structure of amorphous germanium. physica status solidi (b), 15(2), 627-637. https://doi.org/10.1002/pssb.19660150224

Turgut, G. Ü. V. E. N., Sonmez, E., & Duman, S. (2015). Determination of certain sol-gel growth parameters of nickel oxide films. Ceramics International, 41(2), 2976-2989. https://doi.org/10.1016/j.ceramint.2014.10.133

Twagirayezu, F. J. (2017). Theoretical and Experimental Determination of Properties of NiO and Fe-doped NiO. https://digital.library.txstate.edu/handle/10877/6815

Ukoba, K. O., Eloka-Eboka, A. C., & Inambao, F. L. (2018). Review of nanostructured NiO thin film deposition using the spray pyrolysis technique. Renewable and Sustainable Energy Reviews, 82, 2900-2915. https://doi.org/10.1016/j.rser.2017.10.041

Vallikkodi, M. (2018). Synthesis, growth and characterization of piperazinium P-aminobenzoate and piperazinium P-chlorobenzoate nonlinear optical single crystals. Alagappa University, Karaikudi, India. http://dx.doi.org/10.13140/RG.2.2.16046.82243

Vanalakar, S. A., Agawane, G. L., Shin, S. W., Suryawanshi, M. P., Gurav, K. V., Jeon, K. S., Patil, P. S., Jeong, C. W., Kim, J. Y., & Kim, J. H. (2015). A review on pulsed laser deposited CZTS thin films for solar cell applications. Journal of Alloys and Compounds, 619, 109-121. https://doi.org/10.1016/j.jallcom.2014.09.018

Venter, A., & Botha, J. R. (2011). Optical and electrical properties of NiO for possible dielectric applications. South African Journal of Science, 107(1), 1-6. https://hdl.handle.net/10520/EJC97115

Waghmare, M., Sonone, P., Patil, P., Kadam, V., Pathan, H., & Ubale, A. (2018). Spray pyrolytic deposition of zirconium oxide thin films: influence of concentration on structural and optical properties. Engineered Science, 5(2), 79-87. http://dx.doi.org/10.30919/es8d622

Wang, F., Zhao, X., Duan, L., Wang, Y., Niu, H., & Ali, A. (2015). Structural, optical and electrical properties of Hf-doped ZnO transparent conducting films prepared by sol–gel method. Journal of Alloys and Compounds, 623, 290-297. https://doi.org/10.1016/j.jallcom.2014.10.117

Wang, J., Hao, J., Zhang, Y., Wei, H., & Mu, J. (2016). Molecular beam epitaxy deposition of Gd2O3 thin films on SrTiO3 (100) substrate. Physica E: Low-dimensional Systems and Nanostructures, 80, 185-190. https://doi.org/10.1016/j.physe.2016.02.002

Waremra, R. S., & Betaubun, P. (2018). Analysis of electrical properties using the four point probe method. In E3S Web of Conferences (Vol. 73, p. 13019). EDP Sciences. https://doi.org/10.1051/e3sconf/20187313019

Waseda, Y., Matsubara, E., & Shinoda, K. (2011). X-ray diffraction crystallography: introduction, examples and solved problems. Springer Science & Business Media. https://doi.org/10.1007/978-3-642-16635-8

Yin, X., Guo, Y., Xie, H., Que, W., & Kong, L. B. (2019). Nickel oxide as efficient hole transport materials for perovskite solar cells. Solar Rrl, 3(5), 1900001. . https://doi.org/10.1002/solr.201900001

Zahedi, F., Dariani, R. S., & Rozati, S. M. (2013). Effect of substrate temperature on the properties of ZnO thin films prepared by spray pyrolysis. Materials Science in Semiconductor Processing, 16(2), 245-249. https://doi.org/10.1016/j.mssp.2012.11.005

Zaouche, C. (2021). The role of Ni and Zn on diluted magnetic semiconductor Ni1-x Znx O thin films (Doctoral dissertation, Université de mohamed kheider biskra). http://thesis.univ-biskra.dz/id/eprint/5465

Zhao, Y., Wang, H., Wu, C., Li, W., Gao, F., Wu, G., Zhang, B., & Du, G. (2015). Study on the electroluminescence properties of diodes based on n-ZnO/p-NiO/p-Si heterojunction. Optics Communications, 336, 1-4. https://doi.org/10.1016/j.optcom.2014.09.021

Chapter 2 : Nonlinear Optical Responses in Materials

2.1 Introduction

Non-linear optical (NLO) phenomena are a fascinating aspect of materials science, as they involve the interaction between light and matter in ways that are not linear. These phenomena can lead to a wide range of intriguing effects, such as second and third harmonic generation, difference frequency generation, sum frequency generation, the intensity dependence of the complex refractive index, light-by-light scattering, and stimulated light scattering. In this chapter, we will explore the basics of non-linear optics, focusing on the nonlinear wave equation, polarization of matter, linear optics, and nonlinear susceptibilities.

2.1.1 Overview of Non-linear Optical (NLO) Materials

NLO materials exhibit an anisotropic crystal structure in the presence of electromagnetic radiation. The importance of nonlinear optics lies in understanding nonlinearity within induced polarization, as well as analyzing and managing its impact on light propagation in materials. NLO materials can be categorized into various classes, including crystals, polymers, and nanomaterials. Crystalline materials often exhibit strong non-linear responses due to their specific crystal symmetries, making them suitable for various applications in photonic system including high-speed optical modulators, ultrafast optical switches, and high-density optical storage media. However, Several factors influence the non-linear optical response of materials. The bandgap, crystal symmetry, and electronic and vibrational transitions play crucial roles in determining the extent of non-linearity. Understanding these factors is essential for tailoring materials to exhibit desired non-linear optical properties (Darabi et al., 2019; Givens, 1958).

2.1.2 Classification of NLO Materials

NLO materials can be classified based on their nonlinear susceptibilities, which determine the strength of the nonlinear response to an applied electric field. Commonly, materials are classified into three categories (Darabi et al., 2019; Givens, 1958):

1. **Linear materials**: These materials exhibit a linear response to an applied electric field, with their polarization proportional to the electric field strength.

2. **Quasi-linear materials**: These materials exhibit a nonlinear response to an applied electric field, but their nonlinear susceptibility is relatively small compared to other NLO materials.

3. **Nonlinear materials**: These materials exhibit a strong nonlinear response to an applied electric field, with their polarization being a power series in relation to the electric field strength.

2.1.3 Matter-Light Interaction

Matter interacts with the electromagnetic field of light via both its electric and magnetic components. This interaction has the greatest impact on the charged particles within the substance. In the world of nonlinear optics, the electric field has a substantially greater influence on matter than the magnetic field, which is the case in most practical scenarios. Non-linear optics is concerned with the interaction between electromagnetic radiation fields (light) with matter, which results in the formation of a novel field with changes in phase, frequency, polarization, or direction from the original field(s). The intensity of the incoming light is proportional to the square of the electric field's amplitude, indicated as E. The light's fluctuating electric field (E) causes charged particles such as dipoles, ions, atomic nuclei, and electrons to be displaced inside the material. As a result, this process generates a dipole, and the induced dipole per unit volume is known as the polarization (P) (Kauranen et al., 1997; Wolff and Wortmann, 1999).

2.2 Non-linear Optical Phenomena

2.2.1 Maxwell's Equations

The theoretical framework for non-linear optical phenomena is rooted in Maxwell's equations. These equations describe the propagation of electromagnetic waves through a medium and include terms related to the polarization of the material. These equations are given by the following four equations (Dehghan and Salehi, 2014; Ebrahimijahan et al., 2022; Ren et al., 2020):

$$\vec{\nabla} \times \vec{E} = -\frac{1}{c}\frac{\partial \vec{B}}{\partial t} \tag{2-1}$$

$$\vec{\nabla}.\vec{E} = 4\pi\rho \tag{2-2}$$

$$\vec{\nabla} \times \vec{B} = \frac{4\pi}{c}\vec{J} + \frac{1}{c}\frac{\partial \vec{E}}{\partial t} \tag{2-3}$$

$$\vec{\nabla}.\vec{B} = 0 \tag{2-4}$$

With E the electric field, B the magnetic field, ρ the electric charge density and J the current density. ϵ_0 is the vacuum permittivity and μ_0 the vacuum permeability. The wave equation, which describe the propagation of the electric vector field of light in non-linear optical media, can be derived from above Maxwell's equations. The displacement D in linear optics is given as(Wolff and Wortmann, 1999):

$$D = \epsilon_0 E + P \tag{2-5}$$

where ε_0 is the vacuum permittivity, E is the electric field and $P = (P_L + P_{NL})$ is the polarization vector, where P_L and P_{NL} are linear and nonlinear polarization, respectively. Also,

$$P_L = \epsilon_0 \chi^{(1)} E \tag{2-6}$$

Therefore

$$D = \epsilon_0 \left(1 + \chi^{(1)}\right) E + P_{NL} \tag{2-7}$$

$$D = \epsilon E + P_{NL} \tag{2-8}$$

Now from linear optics,

$$\nabla \times E = -\frac{\partial B}{\partial t} \tag{2-9}$$

$$\nabla \times H = \frac{\partial D}{\partial t} \tag{2-10}$$

Using both sides of equation

$$\nabla \times \nabla \times E = -\partial(\nabla \times B)/\ \partial t \tag{2-11}$$

$B = \mu o H$, this implies that

$$\nabla \times \nabla \times E = -\mu o \frac{\partial(\nabla \times H)}{\partial t} = -\mu o \frac{\partial^2 D}{\partial t^2} \tag{2-12}$$

Through substitutions and simplification, we arrived at the nonlinear wave equation as(Evans, 2013; Wolff and Wortmann, 1999).

$$\nabla^2 E - \frac{\mu o \epsilon\, \partial^2 E}{\partial t^2} = \frac{\mu o\, \partial^2 P_{NL}}{\partial t^2} \tag{2-13}$$

2.2.2 Linear Optics: Linear Susceptibility ($\chi^{(1)}$)

Linear susceptibility ($\chi^{(1)}$) describes the linear response of a material to an applied electric field, relating the induced polarization to the electric field. It is connected to the refractive index and the medium's absorption energy from electric field, determining the optical propagation velocity and the medium's response to changes in a first-order way. The output of a linear-optical system with constant parameters will have the same frequency if monochromatic light is fed into it. For instance, red light that enters a lens will remain red after leaving the lens. The linear susceptibility $\chi^{(l)}$ indicates how a medium responds to changes in a first-order way and varies with frequency. In a physical medium, $\chi^{(l)}$ can be considered a scalar quantity. For such a linear medium, this quantity is also linked to the dielectric constant, and there is an equation that describes this relationship is given by (Marder, 2016; Noblet and Humbert, 2019; Vivas et al., 2020):

$$P_L = \epsilon_0 \chi^{(1)} E \tag{2-6}$$

Susceptibility in mathematical processing is considered as having a real and imaginary component. While the imaginary portion of susceptibility is connected to the medium's absorption energy from electric field due to dipole motion of particles in material, the real portion of susceptibility determines the optical propagation velocity in the medium. The refractive index is closely connected to linear susceptibility, which may be calculated using the following equation(Abdel-Galil et al., 2020):

$$\chi^{(1)} = (n^2 + 1)/4\pi \tag{2-14}$$

The output of a linear-optical system with constant parameters will have the same frequency if monochromatic light is fed into it. For instance, red light that enters a lens will remain red after leaving the lens. Figure 2.1 displays images demonstrating the linear optics phenomena (Noblet and Humbert, 2019).

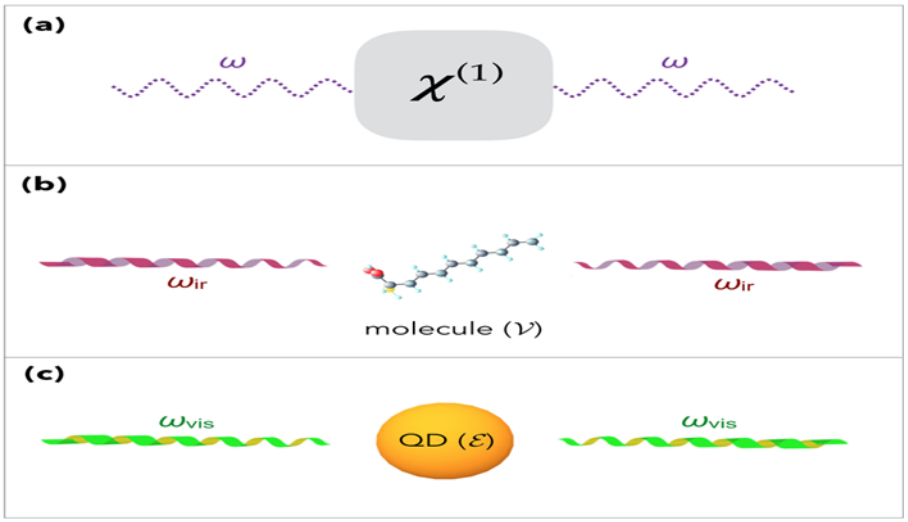

Figure 2.1. Fundamentals of linear optics. a) Geometry of the interaction of a wave with a medium characterized by susceptibility $\chi^{(1)}$. b) Principle of application of infrared radiation to an organic system. c) Principle of application of ultraviolet radiation to an inorganic system (Noblet and Humbert, 2019**).**

The linear susceptibility $\chi^{(l)}$ indicates how a medium responds to changes in a first-order way and varies with frequency. In a physical medium, $\chi^{(l)}$ can be considered a scalar quantity. For such a linear medium (where $\nabla \times E = 0$) given that $\nabla \times \nabla \times E = \nabla (\nabla.E) - \Delta E$ one obtains wave Eq (2-12) of the following form (Evans, 2013; Wolff and Wortmann, 1999):

$$\Delta E - \mu_0 \epsilon_0 \left(\chi^{(1)}(\omega) + 1\right) \frac{\partial^2 E}{\partial t^2} = 0 \tag{2-15}$$

Within somewhat absorbent materials, potential solutions to this differential equation include planar waves traveling in the z-direction, (Wolff and Wortmann, 1999)

$$E(t) = E^{\omega} \exp\left(-\frac{1}{2}\alpha^{\omega} Z\right) \cos(\omega t - k^{\omega} Z) \tag{2-16}$$

In this context, E^{ω} represents the amplitude of the field, while α^{ω} signifies the absorption coefficient and k^{ω} stands for the wave's vector at the frequency ω. The values of α^{ω} and k^{ω} are connected to the real and imaginary components of the linear susceptibility through equations (2-17)–(2-19) (Peiponen et al., 2004; Wolff and Wortmann, 1999).

$$\alpha^{\omega} = \frac{\omega \, \mathrm{Im}\{\chi^{(1)}\}}{c^{\omega} n^{\omega}} \tag{2-17}$$

$$n^{\omega} = \sqrt{1 + \mathrm{Re}\chi^{(1)}} \tag{2-18}$$

$$k^{\omega} = \frac{\omega}{c^{\omega}} = \frac{n^{\omega}}{c_0} = \frac{2\pi n^{\omega}}{\lambda_0} \tag{2-19}$$

where c_0 and λ_o are the speed of light and wavelength in vacuum, respectively.

At large electric field intensities E, it makes intuitive sense that the linear relationship (2-6) would no longer hold true. Anharmonic polarization terms become more significant in optically non-linear media. High electric field strengths caused by high light intensities cause this to happen. The intensity I^{ω} (irradiance, W m^{-2}) carried by an electromagnetic wave in a plane of amplitude E^{ω} is given by (Evans, 2013; Wolff and Wortmann, 1999)

$$I^{\omega} = \frac{1}{2}\epsilon_0 c_0 n^{\omega} |E^{\omega}|^2 \tag{2-20}$$

For instance, E^{ω} is approximately 3×10^{6}V m^{-1} for a pulsed Nd:YAG laser with I^{ω} = 1 MW cm^{-2} of irradiation. Comparing this electric field to usual intramolecular fields that affect electrons and nuclei, it is still tiny. However, a number of non-linear optical processes can develop in the medium as a result of the high-power lasers' huge field strengths.

2.2.3 Nonlinear Susceptibilities ($\chi^{(n)}$)

The electromagnetic response of an optical medium, particularly at optical frequencies, is essentially determined by its polarization, indicated as P(t). A nonlinear polarization may be produced by moving atoms and electrons, which is made possible by the powerful electric fields produced by lasers. To explore the nonlinear reaction of an optical medium, an approach involves expressing the medium's polarization as a power series in relation to the electric field, (Panoiu et al., 2018; Prylepa et al., 2018; Bano et al., 2021)

$$P(t) = \epsilon_0\left[\chi^{(1)}E(t) + \chi^{(2)}E(t)^2 + \chi^{(3)}E(t)^3 + \cdots\right] \tag{2-21}$$

where $\chi^{(i)}$ is the susceptibility of the order of (i + 1) and ε_0 is the permittivity of a vacuum.

The medium's polarization can be separated into linear and nonlinear components, $P(t) = P_L(t) + P_{NL}(t)$, based on its power dependency on the electric field, where

$$P_{NL}(t) = \epsilon_0\chi^{(2)}E(t)^2 + \epsilon_0\chi^{(3)}E(t)^3 + \cdots = P^{(2)}(t) + P^{(3)}(t) + \cdots \tag{2-22}$$

In the above equation, polarizations of second and third order are shown, respectively.

where $\chi^{(i)}$ is the i-th-order NLO susceptibility. The first term $\chi^{(1)}$ expresses the linear optical response. On the other hand, higher-order components ($i \geq 2$) become relevant if the visual field is strong enough or the NLO susceptibility is high (Boyd et al., 2008; Autere et al., 2018), it may result in radiation at frequencies (such as the sum of the input light signals'

frequencies) differing from the frequency of the incoming light. The effects of nonlinear optics at the second order, which encompass phenomena like second-harmonic generation (SHG), as well as sum- and difference-frequency generation (SFG, DFG), are commonly explained using the second-order nonlinear susceptibility denoted as $\chi^{(2)}$ in Equation (2-21). Whereas third-order NLO phenomena (such as third harmonic generation (THG), four-wave mixing (FWM) and saturable absorption (SA)) often arise from the effect of NLO susceptibility $\chi^{(3)}$. Conversely, multiphoton absorption and scattering, and higher harmonic generation are defined using the i-th-order NLO susceptibility $\chi^{(i)}$, where i is often more than 5. The nonlinear processes interaction potency often declines as (i) increases (Boyd et al., 2008; Autere et al., 2018). As a result, second and third-order nonlinear processes are the most visible phenomena making them prevalent in many applications(such as imaging (Zipfel et al., 2003), frequency conversion, (Boyd et al., 2008; Ghotbi et al., 2006) and ultrafast lasers (Li, 2017; Wooten et al., 2000), etc. Figure 2.2).

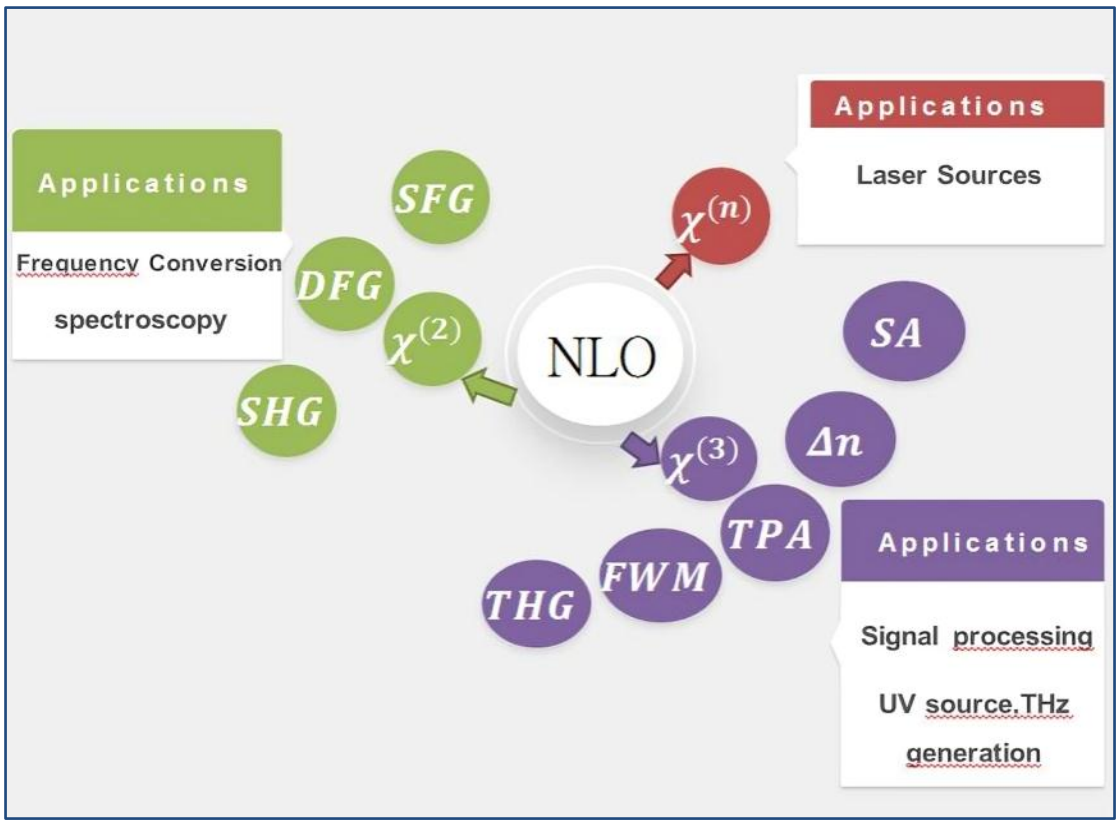

Figure 2.2. Nonlinear optical principles. Various NLO uses are illustrated. TPA refers to two-photon absorption, while Δn expresses the refractive index variation based on the intensity(Autere et al., 2018).

2.2.4 Descriptions of Nonlinear Optical Processes

Nonlinear optical processes describe the wide range of events that occur when strong light interacts with a material and causes effects that are incompatible with the strength of the incoming light. The electromagnetic field of light interacts with the material's electric dipoles or electronic structure, leading to nonlinear optical processes. These interactions can result in a variety of intriguing occurrences, including:

2.2.4.1 Second-order processes

The second-order NLO susceptibility $\chi^{(2)}$ relates to the second-order NLO phenomena as second harmonic generation (SHG), difference frequency generation (DFG), and sum frequency generation (SFG). With SHG, an input wave with frequency ω generates an output signal with twice the frequency 2ω. In both DFG and SFG, a new photon may be created from two input photons with frequencies ω_1 and ω_2. The SFG process produces a brand-new photon with the frequency ($\omega_3 = \omega_1 + \omega_2$). On the other hand, in the DFG process, the annihilation of pump photons with frequencies of ω_1 and ω_2 results in a photon with frequency ($\omega_3 = \omega_1 - \omega_2$), as seen in Figure 2.3(Kalsoom et al., 2021; Panoiu et al., 2018).

Let's take a second-harmonic generation, which is schematically depicted in Figure 2.3, as an illustration of NLO interaction. The electric field strength of a laser beam is depicted here as (Boyd, 2020),

$$E(t) = Ee^{-i\omega t} + c.c \tag{2-23}$$

The nonlinear polarization produced by a non-zero $\chi^{(2)}$ crystal following the application of electric intensity is given as (Kalsoom et al., 2021; Boyd, 2020):

$$P^{(2)}(t) = 2\epsilon_0\chi^{(2)}EE^* + \left(\epsilon_0\chi^{(2)}E^2e^{-i2\omega t} + c.c.\right) \tag{2-24}$$

Second harmonic generation (SHG) is caused when $\omega_1 = \omega_2 = \omega$ and $\omega_3 = 2\omega$ by the polarization P($\omega_3 = 2\omega$). Franken et al. (Franken et al., 1961) focused a ruby laser's 694.3 nm output onto a quartz crystal to produce a very weak output at 347.15 nm, which they used to make the first observation of this phenomenon. As a result, the frequency of the incoming light is doubled,, allowing one to use lasers with wavelengths that reach into the blue and ultraviolet regions of the spectrum. The laser-induced nuclear fusion process, which seems to be more

effective at higher optical frequencies, is one significant use of SHG (Boyd et al., 2008; Arivuoli, 2001).

Next, let's look at the case when the optical field impinge on a second-order nonlinear optical material has two separate frequency elements, which we express as follows (Vyas et al., 2022; Boyd, 2020):

$$E(t) = E_1 e^{-i\omega_1 t} + E_2 e^{-i\omega_2 t} + c.c. \tag{2-25}$$

And as we know earlier from Eq. (2-25) that the second-order component of the nonlinear polarization follows the pattern:

$$P^{(2)}(t) = \epsilon_0 \chi^{(2)} E(t)^2 \tag{2-26}$$

According to Equations (2-25) and (2-26), the second-order nonlinear polarization produced within this medium is determined as follows (Panoiu et al., 2018; Vyas et al., 2022; Boyd, 2020):

$$P^{(2)}(t) = \epsilon_0 \chi^{(2)} \left[E_1^2 e^{-2i\omega_1 t} + E_2^2 e^{-2i\omega_2 t} + 2E_1 E_2 e^{-i(\omega_1+\omega_2)t} + 2E_1 E_2^* e^{-i(\omega_1-\omega_2)t} + c.c. \right] + 2\epsilon_0 \chi^{(2)} [E_1 E_1^* + E_2 E_2^*] \tag{2-27}$$

The various variables in Equation (2-27) represent four distinct second-order NLO processes. Second-harmonic generation (SHG), which is illustrated in the first and second phrases. Sum-frequency generation (SFG) and differential frequency generation (DFG) are denoted by the third and fourth components, respectively. The final phrase stands for optical rectification (OR) (Panoiu et al., 2018; Vyas et al., 2022).

This finding may be easily expressed by using the notation (Panoiu et al., 2018; Boyd, 2020):

$$P^{(2)}(t) = \sum_n P(\omega_n) e^{-i\omega_n t} \tag{2-28}$$

The nonlinear polarizations that describe many second-order nonlinear optical phenomena can be stated as follows (Panoiu et al., 2018; Boyd, 2020):

$$P_{SHG}^{(2)}(2\omega_1) = \epsilon_0 \chi^{(2)} E_1^2 \tag{2-29}$$

$$P_{SHG}^{(2)}(2\omega_2) = \epsilon_0 \chi^{(2)} E_2^2 \tag{2-30}$$

$$P_{SFG}^{(2)}(\omega_1 + \omega_2) = 2\epsilon_0 \chi^{(2)} E_1 E_2 \tag{2-31}$$

$$P_{DFG}^{(2)}(\omega_1 - \omega_2) = 2\epsilon_0\chi^{(2)}E_1E_2^* \quad (2\text{-}32)$$

$$P_{OR}^{(2)}(0) = 2\epsilon_0\chi^{(2)}[E_1E_1^* + E_2E_2^*] \quad (2\text{-}33)$$

Figure 2.3 presents a schematic illustration of the three most prevalent second-order NLO phenomena represented by the foregoing equations, namely SHG, SFG, and DFG (Panoiu et al., 2018). Each of these processes has its practical applications. These nonlinear optical processes, for instance, are used in several wavelength conversion systems. The generation of new coherent light components can occur at wavelengths that are either shorter (SHG, SFG) or longer (DFG) than those of the incident beams (Vyas et al., 2022).

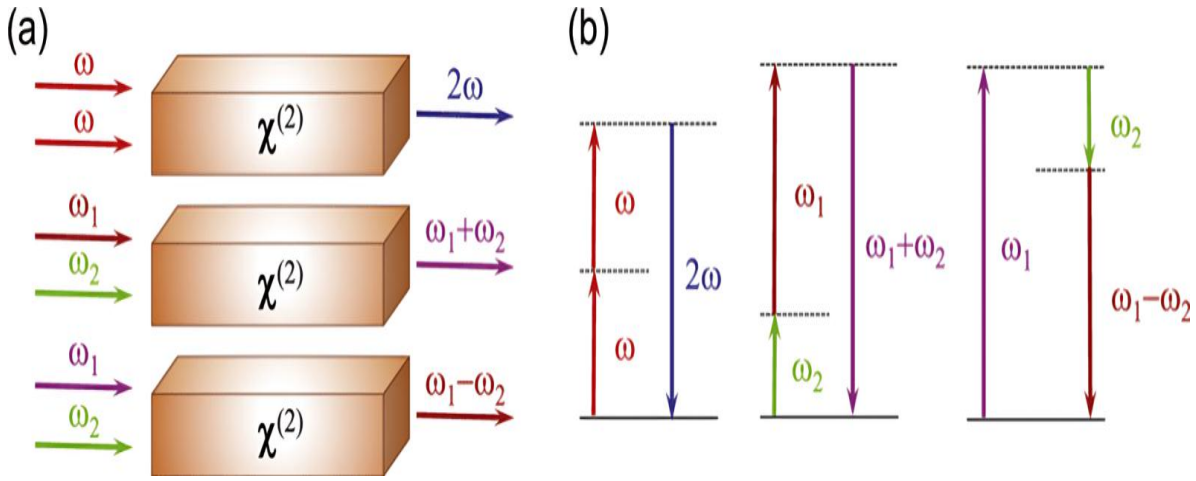

Figure 2.3. Visual representation of second-order NLO processes. (a) Depicting SHG, SFG, and SDG sequentially from top to bottom. (b) Arranging energy-level diagrams from left to right to portray SHG, SFG, and SDG, respectively (Panoiu et al., 2018).

2.2.4.2 Third-order processes

Third-order nonlinear optical phenomena emerge due to the presence of the third component in Equation (2-21). It should be observed that $\chi^{(2)}$ disappears for materials having a center of symmetry, but odd terms, such as $\chi^{(3)}$, are nonzero for all media (Kodikara et al., 2018). Nonlinear optical (NLO) interactions in crystals via third-order susceptibility $\chi^{(3)}$ are of tremendous study and practical interest due to their applicability to diverse optical systems and optical information processing. Optical harmonic production is a well-established spectroscopic technique to learn important details about the materials' NLO properties (Shanon et al., 2016). Third-order susceptibility is crucial in photonics because it exhibits a large variety of switching-related phenomena. This becomes clear when considering an electric field E that consists of three distinct frequency components ω_k (Vyas et al., 2022; Ahmed and Glesk, 2015):

$$E(t) = E_1 e^{-i\omega_1 t} + E_2 e^{-i\omega_2 t} + E_3 e^{-i\omega_3 t} + c.c. \quad (2\text{-}34)$$

We then take into account the nonlinear polarization's third-order impact.

$$P^3(t) = \epsilon_0 \chi^{(3)} E(t)^3 \quad (2\text{-}35)$$

The third-order polarization $P^{(3)}(t)$, which has 44 distinct frequency components, may be determined by using the third term in Equation (2-21) and assuming the electric field as E. Within these, the terms associated with frequencies $3\omega_1$, $3\omega_2$ and $3\omega_3$ delineate the phenomenon known as third-harmonic generation (THG). Additionally, third-order nonlinear effects encompass other processes such as four-wave mixing (FWM), alterations in refractive index dependent on intensity and saturable absorption). These effects generally originate from the third-order NLO susceptibility $\chi^{(3)}$ (Vyas et al., 2022; Autere et al., 2018).

2.2.4.2.1 Third-Harmonic Generation (THG)

One type of third-order nonlinear effect is THG. Similar to SHG, the third harmonic is created by the interaction of three photons with the same frequency (ω), which is seen in Figure 2.4. This interaction results in the creation of a single photon with the frequency of 3ω, or $\omega_{THG} = 3\omega$. THG is not dependent on centered inversion symmetry breaking, but rather on a medium's third-order NLO susceptibility and limited phase-matching in the excitation area. In light of this, THG can be produced whether the material is centrosymmetric or not. While THG has a cubic dependence on the intensity of the excitation light, its function is comparable to that of SHG (Welford, 1985; Boyd et al., 2008; Zhou et al., 2020).

Higher-order harmonics are often weaker than lower-order ones (Wen et al., 2019). To form a THG photon, which has a lower probability than the two photon scenario in SHG, three photons must emerge simultaneously. THG, however, was substantially more potent than SHG in monolayer MoS_2 under (1560 nm) stimulation, according to two studies (Säynätjoki et al., 2017; Woodward et al., 2016).

THG is important for frequency conversion and grain boundary identification. Karvonen et al revealed that the contrast between the borders and the grains in THG imaging was substantially higher than in traditional SHG, Raman, and PL mapping, making it a strong tool for the quick and sensitive characterisation of materials (Karvonen et al., 2017).

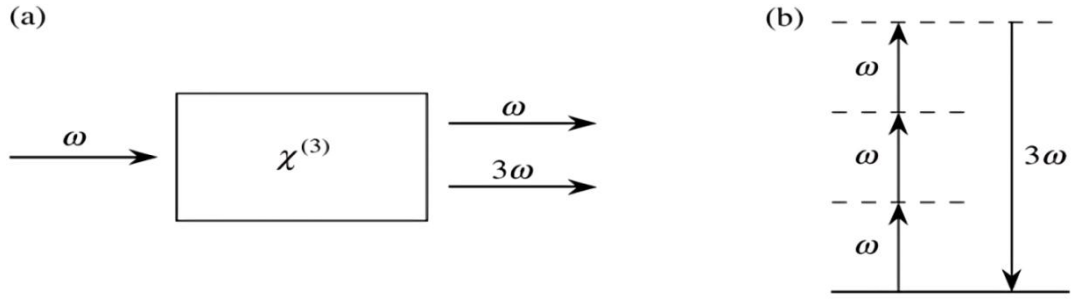

Figure 2.4. Third-harmonic generation. (a) A look of the interaction's geometry. (b) A description of energy levels (Boyd, 2020).

2.2.4.2.2 Four-Wave Mixing (FWM)

FWM is a third-order nonlinearity in which the interaction of two or three photons with distinct wavelengths results in the production of two or a single photon with novel wavelengths. No matter if the material is inversion symmetric, FWM is a third-order NLO process. So, theoretically, FWM may be produced in any material. FWM often comes in a wide variety of forms, one of which is seen in Figure 2.5. This energy curve is consistent with the equation ($w_4 = w_1 + w_2 - w_3$). FWM is widely utilized in a variety of applications, including imaging, wavelength conversion, and numerous other types of optical processing (Welford, 1985; Boyd et al., 2008; Zhou et al., 2020).

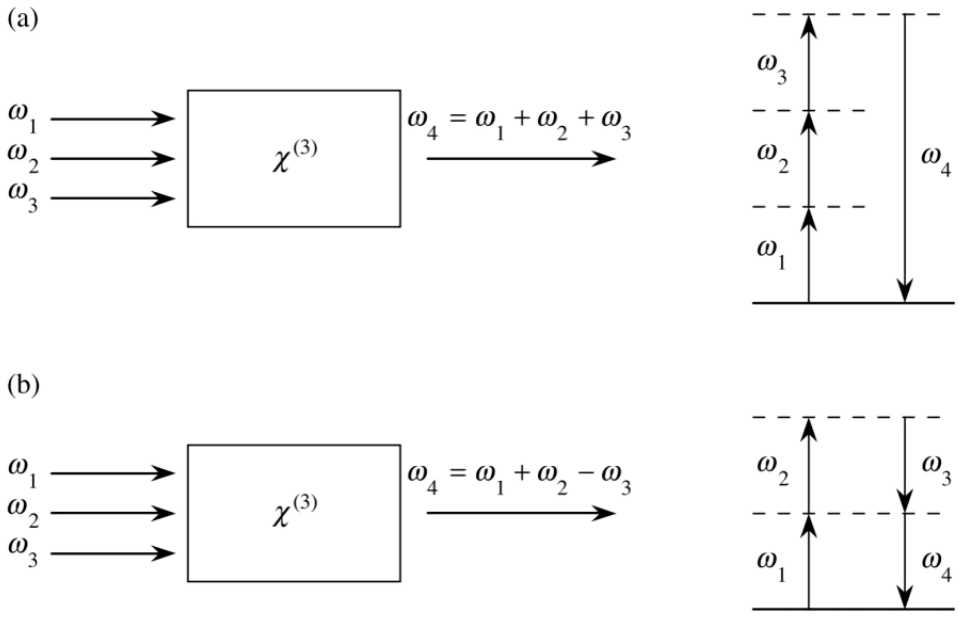

Figure 2.5. Two potential mixing mechanisms can be delineated. This phenomenon arises through the interaction of three incident waves within a medium distinguished by the susceptibility $\chi^{(3)}$ (Boyd, 2020).

2.2.4.2.3 Intensity-Dependent Refractive Index

The most common third-order NLO phenomenon that has been studied in nonlinear plasmons and nonlinear optics more broadly is the Kerr effect. When a nonlinear optical medium interacts with an optical field, its refractive index changes. The Kerr effect is described by a nonlinear polarization of the third order, which can be written as (Panoiu et al., 2018; Boyd et al., 2008):

$$P_{NL}(\omega) = 3\epsilon_0\chi^{(3)}|E(\omega)|^2E(\omega) \tag{2-36}$$

Given the limits of equation (2-21), the total polarization (P_{TOT}) can be expressed as follows (Boyd et al., 2008):

$$P_{TOT}(\omega) = \epsilon_0\left[\chi^{(1)}E(\omega) + 3\chi^{(3)}|E(\omega)|^2E(\omega)\right] = \epsilon_0\chi_{eff}E(\omega) \tag{2-37}$$

where $\chi_{eff} = (\chi^{(1)} + 3\chi^{(3)}|E(\omega)|^2)$ is the effective susceptibility.

We see that in general, there is a relationship between nonlinear susceptibility $\chi^{(3)}$ and nonlinear refractive index n^2 which is as follows (Boyd et al., 2008):

$$n^2 = 1 + 4\pi\chi_{eff} \tag{2-38}$$

While the refractive index of various materials may be explained by the relationship (Panoiu et al., 2018; Boyd et al., 2008):

$$n = n_0 + 2\tilde{n}_2|E(\omega)|^2 \tag{2-39}$$

where n_0 is the linear refractive index and $\tilde{n}_2$ is a new optical constant that indicates how high the refractive index rises when the optical density increases. By integrating equation (2-39) on the left side and the effective susceptibility formula on the right side of equation (2-38), we find that

$$[n_0 + 2\tilde{n}_2|E(\omega)|^2]^2 = 1 + 4\pi\chi^{(1)} + 12\pi\chi^{(3)}|E(\omega)|^2 \tag{2-40}$$

Consequently, by matching, we find

$$n_0 = \left(1 + 4\pi\chi^{(1)}\right)^{1/2} \tag{2-41}$$

And

$$\tilde{n}_2 = \frac{3\pi}{n_0}\chi^{(3)} \tag{2-42}$$

When a coherent laser beam passes through a nonlinear material, the refractive index is altered (or modified). Nonlinear refractive index (n_2) is one of the most significant third-order nonlinear optical characteristics of a photonic material. This non-linear refractive index defines the optical Kerr effect, wherein the refractive index (n) varies in accordance with the intensity (I) of the incident light, as expressed by (Vyas et al., 2022):

$$n = n_0 + n_2 I \tag{2-43}$$

where $I = (n_0 c/4\pi)E^2$ is the intensity of the incident wave (Boyd et al., 2008).

Given that the overall refractive index n remains constant under both characterizations of the nonlinear contribution, a comparison of Equations (2-39) and (2-43) reveals that (Panoiu et al., 2018):

$$2\tilde{n}_2|E(\omega)|^2 = n_2 I \tag{2-44}$$

so that $\tilde{n}_2$ and n_2 are connected by (Boyd et al., 2008):

$$n_2 = \frac{4\pi}{n_0 c}\tilde{n}_2 \tag{2-45}$$

Where by entering equation (2-42) in (2-45) we find that n_2 is connected to $\chi^{(3)}$ by (Evans and Mazur, 2012; Boyd et al., 2008):

$$n_2 = \frac{12\pi^2}{n_0^2 c}\chi^{(3)} \tag{2-46}$$

Since it is frequently more practical to express I in quantities of W/cm^2, n_2 is therefore expressed in units of cm^2/W. We then determine that numerically (Evans and Mazur, 2012):

$$n_2\left(\frac{cm^2}{w}\right) = \frac{12\pi^2}{n_0^2 c}10^7\chi^{(3)}(esu) \tag{2-47}$$

Table 2.1 reveals the ranges of n_2 values for certain materials (Li, 2017).

Table 2.1. n_2 values ranges for some materials (Li, 2017).

number	Material	Range / cm^2W^{-1}
1	glass	10^{-16}-10^{-14}
2	Doped - glass	10^{-14}-10^{-7}
3	Organic - material	10^{-18}-10^{-8}
4	semiconductor	10^{-10}-10^{-2}

2.2.4.2.4 Saturable absorption (SA)

Saturable absorption is an illustration of a nonlinear optical phenomenon. Many material systems possess the feature that when tested with a high laser intensity, their absorption coefficient falls. A common formulation for the relationship between the observed absorption coefficient and the incident laser radiation's intensity is (Boyd, 2020) :

$$\alpha = \frac{\alpha_0}{1+I/I_S} \tag{2-48}$$

Here, α_0 represents the absorption coefficient at low intensities and I_s signifies the saturable intensity, which denotes the intensity corresponding to half of the maximum absorption.

Saturable absorption is an NLO feature of materials that happens in the presence of high-intensity light sources such as lasers. The Pauli-blocking effect causes saturable absorption, which occurs when a transition state is completely occupied and can no longer take incoming electrons (Schröder et al., 1980). When a light beam interacts with NLO material, electrons in the valence band absorb incoming photons and are stimulated to the conduction band. Figure 2.6a illustrates how most photons are absorbed at low incoming intensities, leading to limited transmission. Conversely, when subjected to relatively elevated intensities of incident laser beams, a significant quantity of electrons becomes excited, populating the conduction band of a saturable absorption (SA) specimen with a ground state cross-section smaller than that of the excited states. As a result, the majority of incoming photons are not absorbed and pass through the material, resulting in high transmission, as seen in Figure 2.6b (Wang et al., 2019).

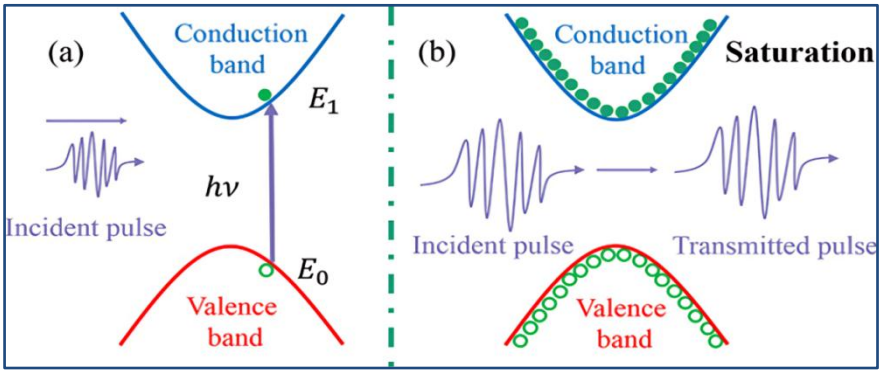

Figure 2.6. The theory of saturable absorption owing to Pauli-blocking. (a) A low-intensity laser beam is impinge on a nonlinear optical medium with a poor transmission. (b) The interaction of a high-intensity laser beam with a nonlinear optical material results in high transmission (Wang et al., 2019).

2.2.4.2.5 Two-Photon Absorption (TPA)

A further nonlinear process that results from the imaginary portion of $\chi^{(3)}$ is two-photon absorption. TPA is the process by which two photons with the same or different frequency are simultaneously absorbed by a molecular system, stimulating it to change its electronic state. During this process, the system initially takes in one photon and is excited to a virtual state. After that, before returning to its original state, it rapidly absorbs a second photon, culminating in its elevation to the final state. Figure 2.7 depicts a visual illustration of the TPA procedure (Rumi and Perry, 2010; Alam et al., 2014).

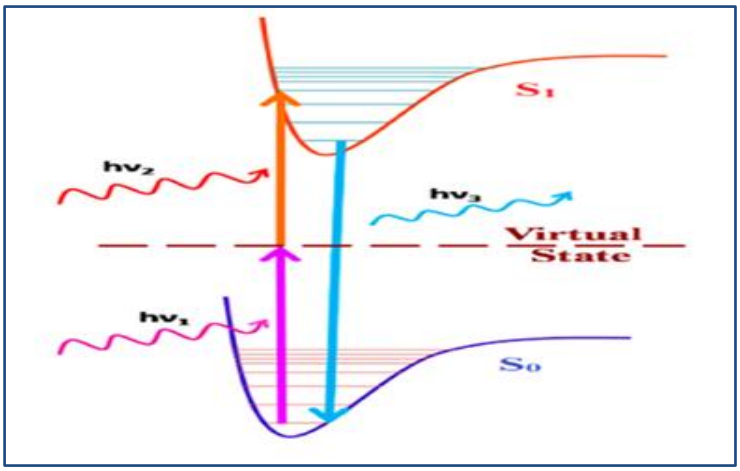

Figure 2.7. Pictorial representation of two-photon absorption process(Alam et al., 2014).

Another crucial factor for assessing a nonlinear photonic device is the TPA coefficient (α_2), which pertains to the TPA phenomenon involving electronic transitions due to the concurrent absorption of two photons. Given the presence of TPA, the intensity-dependent nonlinear absorption coefficient (α) is as follows (Vyas et al., 2022; Sun et al., 2006):

$$\alpha = \alpha_0 + \alpha_2 I \tag{2-49}$$

where α_0 is the linear absorption coefficient and α_2 is the nonlinear absorption coefficient.

Third-order optical susceptibility is correlated with a nonlinear index of refraction as well as a nonlinear absorption coefficient. From experimentally determining n_2 and α_2 in accordance with the following relationships, the results of the real and imaginary portions of the third-order nonlinear optical susceptibility $\chi^{(3)}$ were found (Sun et al., 2006; Shanon et al., 2016):

$$\mathrm{Re}\chi^{(3)} = \left(\frac{\epsilon_0 c^2}{10^4 \pi}\right) n_0^2 n_2 \tag{2-50}$$

$$\mathrm{Im}\chi^{(3)} = \left(\frac{\epsilon_0 c^2}{4\times10^2\pi^2}\right) n_0^2 \lambda \alpha_2 \quad (2\text{-}51)$$

Here, c denotes the velocity of light in a vacuum (3×10^8 m/s), ε_0 is the vacuum permittivity (8.854×10^{-12} F/m).

2.2.4.3 Higher-order processes

The high-order NLO susceptibility $\chi^{(n)}$ is a good indicator of HHG and high-order multiphoton scattering, absorption, and luminescence. Because the intensity of nonlinear process interactions often diminishes with n, the high-order NLO effects, including HHG, are relatively weak and insignificant. However, given the length restrictions of this study, a detailed explanation of their few applications in the characterization of materials will not be provided. The prominent and most frequently noticed phenomena in nonlinear systems that we shall concentrate on are the second and third-order NLO effects (Zhou et al., 2020).

The lower-order processes often predominate in nonlinear interactions, making fourth, fifth, and higher-order nonlinear optical processes the subject of few experiments. However, there exists an exception known as three-photon absorption (3PA), which is a fifth-order nonlinear optical process that concurrently absorbs three photons during an electronic transition. In instances involving 3PA, the intensity-dependent absorption coefficient can be expressed as $\alpha = \alpha_0 + \alpha_3 I^2$, where ($\alpha_3$) is the 3PA coefficient (Vyas et al., 2022; Aitchison et al., 1997).

2.3 Non-linear Phenomena in NiO Thin Films

Thin films are materials with a thickness ranging from a few nanometers to several micrometers. Their optical properties are influenced by quantum effects, surface states, and the nature of the interfaces. I addition, theirs properties are distinct from those of bulk materials, owing to quantum confinement effects and altered electron-photon interactions. A critical aspect is the modification of the non-linear susceptibility (χ) due to the confined nature of electrons and photons in thin films. Hence, it present a unique platform for studying non-linear optical phenomena. The thickness-dependent non-linear susceptibility reveals the intricate relationship between the thickness of a thin film and its non-linear optical response. As the film thickness decreases, the quantum confinement effects become more pronounced, affecting the electronic structure and, consequently, the non-linear optical behavior (Semin et al., 2021).

NiO thin films, composed of nickel oxide, are of particular interest due to their pronounced non-linear optical properties. Understanding the structural and optical properties of NiO thin films is essential for correlating their behavior with non-linear optical phenomena. NiO thin films, with their tailored non-linear optical properties, find applications in sensing and imaging technologies. Their use in nonlinear microscopy and sensing of environmental changes showcases the versatility of NiO thin films in real-world applications.

Several synthesis methods are employed to fabricate NiO thin films, each influencing the resulting material properties. Techniques such as physical vapor deposition, chemical vapor deposition, and sol-gel processes offer varying levels of control over film thickness, crystallinity, and morphology. The choice of synthesis method is crucial in tailoring NiO thin films for specific applications.

2.4 Conclusion

This section provided an in-depth exploration of the nonlinear reaction of materials when subjected to light. It also delved into second- and third-order nonlinear optical processes, which fall within the realm of nonlinear optical phenomena. The subsequent chapter will encompass two phases: the initial stage will delve into the experimental procedures employed to acquire NiO thin films, while the second stage will concentrate on characterizing the films using diverse techniques tailored to the specific properties.

References

Abdel-Galil, A., Assiri, M. A., & Yahia, I. S. (2020). Optical analysis of methyl violet thin films/polymeric substrate for flexible organic technology. Optical and Quantum Electronics, 52, 1-20. https://doi.org/10.1007/s11082-020-02491-6

Ahmed, M. S., & Glesk, I. (2015). Photonic platform and the impact of optical nonlinearity on communication devices. acta physica slovaca, 65(2), 65-152. https://strathprints.strath.ac.uk/id/eprint/53580

Aitchison, J. S., Hutchings, D. C., Kang, J. U., Stegeman, G. I., & Villeneuve, A. (1997). The nonlinear optical properties of AlGaAs at the half band gap. IEEE Journal of Quantum Electronics, 33(3), 341-348. https://doi.org/10.1109/3.556002

Alam, M. M., Chattopadhyaya, M., Chakrabarti, S., & Ruud, K. (2014). Chemical control of channel interference in two-photon absorption processes. Accounts of Chemical Research, 47(5), 1604-1612. https://doi.org/10.1021/ar500083f

Arivuoli, D. (2001). Fundamentals of nonlinear optical materials. Pramana, 57, 871-883. https://doi.org/10.1007/s12043-001-0004-1

Autere, A., Jussila, H., Dai, Y., Wang, Y., Lipsanen, H., & Sun, Z. (2018). Nonlinear optics with 2D layered materials. Advanced Materials, 30(24), 1705963. https://doi.org/10.1002/adma.201705963

Bano, R., Asghar, M., Ayub, K., Mahmood, T., Iqbal, J., Tabassum, S., Zakaria, R., & Gilani, M. A. (2021). A theoretical perspective on strategies for modeling high performance nonlinear optical materials. Frontiers in Materials, 8, 783239. https://doi.org/10.3389/fmats.2021.783239

Boyd, R. W. (2020). Nonlinear Optics (4th ed.). Academic Press. https://doi.org/10.1016/B978-0-12-811002-7.00010-2

Boyd, R. W., Gaeta, A. L., & Giese, E. (2008). Nonlinear optics. In Springer Handbook of Atomic, Molecular, and Optical Physics (pp. 1097-1110). Cham: Springer International Publishing. https://doi.org/10.1007/978-3-030-73893-8_76

Darabi, H., Adelifard, M., & Rajabi, Y. (2019). Characterization of nonlinear optical refractive index for graphene oxide–silicon oxide nanohybrid composite. Journal of Nonlinear Optical Physics & Materials, 28(01), 1950005. https://doi.org/10.1142/S021886351950005X

Dehghan, M., & Salehi, R. (2014). A meshless local Petrov–Galerkin method for the time-dependent Maxwell equations. Journal of Computational and Applied Mathematics, 268, 93-110. https://doi.org/10.1016/j.cam.2014.02.013

Ebrahimijahan, A., Dehghan, M., & Abbaszadeh, M. (2022). Simulation of Maxwell equation based on an ADI approach and integrated radial basis function-generalized moving least squares (IRBF-GMLS) method with reduced order algorithm based on proper orthogonal decomposition. Engineering Analysis with Boundary Elements, 143, 397-417. https://doi.org/10.1016/j.enganabound.2022.06.020

Evans, C. C. (2013). Nonlinear optics in titanium dioxide: from bulk to integrated optical devices (Doctoral dissertation, Harvard University). http://nrs.harvard.edu/urn-3:HUL.InstRepos:11181139

Evans, C. C., & Mazur, E. (2012). Nanophotonics: Linear and Nonlinear Optics at the Nanoscale. In Nano-Optics for Enhancing Light-Matter Interactions on a Molecular Scale: Plasmonics, Photonic Materials and Sub-Wavelength Resolution (pp. 119-176). Dordrecht: Springer Netherlands. https://doi.org/10.1007/978-94-007-5313-6_7

Franken, E. P., Hill, A. E., Peters, C. W., & Weinreich, G. (1961). Generation of optical harmonics. Physical review letters, 7(4), 118. https://doi.org/10.1103/PhysRevLett.7.118

Ghotbi, M., Sun, Z., Majchrowski, A., Michalski, E., Kityk, I. V., & Ebrahim-Zadeh, M. (2006). Efficient third harmonic generation of microjoule picosecond pulses at 355nm in BiB3O6. Applied Physics Letters, 89(17). https://doi.org/10.1063/1.2364880

Givens, M. P. (1958). Optical properties of metals. In Solid State Physics (Vol. 6, pp. 313-352). Academic Press. https://doi.org/10.1016/S0081-1947(08)60729-8

Kalsoom, U. E., Yi, R., Qu, J., & Liu, L. (2021). Nonlinear optical properties of CdSe and CdTe core-shell quantum dots and their applications. Frontiers in Physics, 9, 612070. https://doi.org/10.3389/fphy.2021.612070

Karvonen, L., Säynätjoki, A., Huttunen, M. J., Autere, A., Amirsolaimani, B., Li, S., Norwood, R. A., Peyghambarian, N., Lipsanen, H., Eda, G., Kieu, K., & Sun, Z. (2017). Rapid visualization of grain boundaries in monolayer MoS2 by multiphoton microscopy. Nature communications, 8(1), 15714. https://doi.org/10.1038/ncomms15714

Kauranen, M., Maki, J. J., Verbiest, T., Van Elshocht, S., & Persoons, A. (1997). Quantitative determination of electric and magnetic second-order susceptibility tensors of chiral surfaces. Physical Review B, 55(4), R1985. https://doi.org/10.1103/PhysRevB.55.R1985

Kodikara, M. S., Stranger, R., & Humphrey, M. G. (2018). Computational studies of the nonlinear optical properties of organometallic complexes. Coordination Chemistry Reviews, 375, 389-409. https://doi.org/10.1016/j.ccr.2018.02.007

Li, C. (2017). Nonlinear Optics: Principles and Applications. Springer : Shanghai Jiao Tong University Press. https://doi.org/10.1007/978-981-10-1488-8

Li, C., & Li, C. (2017). All-optical switch based on nonlinear optics. Nonlinear Optics: Principles and Applications, 279-386. https://doi.org/10.1007/978-981-10-1488-8_10

Marder, S. R. (2016). Materials for third-order nonlinear optics. MRS Bulletin, 41(1), 53-62. https://doi.org/10.1557/mrs.2015.310

Noblet, T., & Humbert, C. (2019). Sum-frequency generation through a unique Feynman diagram formalism: the case of bipartite organic/inorganic complexes. arXiv preprint arXiv:1906.03197. https://doi.org/10.48550/arXiv.1906.03197

Panoiu, N. C., Sha, W. E., Lei, D. Y., & Li, G. C. (2018). Nonlinear optics in plasmonic nanostructures. Journal of Optics, 20(8), 083001. https://doi.org/10.1088/2040-8986/aac8ed

Peiponen, K. E., Lucarini, V., Saarinen, J. J., & Vartiainen, E. (2004). Kramers—Kronig Relations and Sum Rules in Nonlinear Optical Spectroscopy. Applied spectroscopy, 58(5), 499-509. https://doi.org/10.1366/000370204774103309

Prylepa, A., Reitböck, C., Cobet, M., Jesacher, A., Jin, X., Adelung, R., Schatzl-Linder, M., Luckeneder, G., Stellnberger, K. H., & Stifter, D. (2018). Material characterisation with methods of nonlinear optics. Journal of Physics D: Applied Physics, 51(4), 043001. https://doi.org/10.1088/1361-6463/aa9df4

Ren, H., Zhuang, X., & Rabczuk, T. (2020). A higher order nonlocal operator method for solving partial differential equations. Computer Methods in Applied Mechanics and Engineering, 367, 113132. https://doi.org/10.1016/j.cma.2020.113132

Rumi, M., & Perry, J. W. (2010). Two-photon absorption: an overview of measurements and principles. Advances in Optics and Photonics, 2(4), 451-518. https://doi.org/10.1364/AOP.2.000451

Säynätjoki, A., Karvonen, L., Rostami, H., Autere, A., Mehravar, S., Lombardo, A., Norwood, R. A., Hasan, T., Peyghambarian, N., Lipsanen, H., Kieu, K., Ferrari, A.C., Polini, M., & Sun, Z. (2017). Ultra-strong nonlinear optical processes and trigonal warping in MoS_2 layers. Nature communications, 8(1), 893. https://doi.org/10.1038/s41467-017-00749-4

Schröder, W. U., Birkelund, J. R., Huizenga, J. R., Wilcke, W. W., & Randrup, J. (1980). Effect of Pauli blocking on exchange and dissipation mechanisms operating in heavy-ion reactions. Physical Review Letters, 44(5), 308. https://doi.org/10.1103/PhysRevLett.44.308

Semin, S., Li, X., Duan, Y., & Rasing, T. (2021). Nonlinear optical properties and applications of fluorenone molecular materials. Advanced Optical Materials, 9(23), 2100327. https://doi.org/10.1002/adom.202100327

Shanon, Z. S., Alnayli, R. S., & Tahir, K. J. (2016). Study of the second and third harmonics generation in lithium triborate single crystal. International Journal of science and Research (IJSR), 1614-161. https://doi.org/10.21275/ART20161209

Sun, X. B., Wang, X. Q., Ren, Q., Zhang, G. H., Yang, H. L., & Feng, L. (2006). Third-order nonlinear optical properties of bis (tetrabutylammonium) bis (4, 5-dithiolato-1, 3-dithiole-2-thione) copper. Materials research bulletin, 41(1), 177-182. . https://doi.org/10.1016/j.materresbull.2005.07.021

Vivas, M. G., da Silva, D. L., Mendonca, C. R., & De Boni, L. (2020). First-order hyperpolarizability of organic molecules: hyper-Rayleigh scattering and applications. In Molecular and Laser Spectroscopy (pp. 275-314). Elsevier. https://doi.org/10.1016/B978-0-12-818870-5.00008-3

Vyas, K., Espinosa, D. H., Hutama, D., Jain, S. K., Mahjoub, R., Mobini, E., ... & Dolgaleva, K. (2022). Group III-V semiconductors as promising nonlinear integrated photonic platforms. Advances in Physics: X, 7(1), 2097020. https://doi.org/10.1080/23746149.2022.2097020

Wang, G., Baker-Murray, A. A., & Blau, W. J. (2019). Saturable absorption in 2D nanomaterials and related photonic devices. Laser & Photonics Reviews, 13(7), 1800282. https://doi.org/10.1002/lpor.201800282

Welford, W. T. (1985). The Principles of Nonlinear Optics. Physics Bulletin, 36(4), 178. https://doi.org/10.1088/0031-9112/36/4/046

Wen, X., Gong, Z., & Li, D. (2019). Nonlinear optics of two-dimensional transition metal dichalcogenides. InfoMat, 1(3), 317-337. https://doi.org/10.1002/inf2.12024

Wolff, J. J., & Wortmann, R. (1999). Organic materials for second-order non-linear optics. Advances in physical organic chemistry, 32, 121-217. https://doi.org/10.1016/S0065-3160(08)60007-6

Woodward, R. I., Murray, R. T., Phelan, C. F., De Oliveira, R. E. P., Runcorn, T. H., Kelleher, E. J. R., ... & De Matos, C. J. S. (2016). Characterization of the second-and third-order nonlinear optical susceptibilities of monolayer MoS_2 using multiphoton microscopy. 2D Materials, 4(1), 011006. https://doi.org/10.1088/2053-1583/4/1/011006

Wooten, E. L., Kissa, K. M., Yi-Yan, A., Murphy, E. J., Lafaw, D. A., Hallemeier, P. F., Maack, D. R., Attanasio, D. V., Fritz, D. J., McBrien, G. J., & Bossi, D. E. (2000). A review of lithium niobate modulators for fiber-optic communications systems. IEEE Journal of selected topics in Quantum Electronics, 6(1), 69-82. https://doi.org/10.1109/2944.826874

Zhou, L., Fu, H., Lv, T., Wang, C., Gao, H., Li, D., ... & Xiong, W. (2020). Nonlinear optical characterization of 2D materials. Nanomaterials, 10(11), 2263. https://doi.org/10.3390/nano10112263

Zipfel, W. R., Williams, R. M., & Webb, W. W. (2003). Nonlinear magic: multiphoton microscopy in the biosciences. Nature biotechnology, 21(11), 1369-1377. https://doi.org/10.1038/nbt899

Chapter 3 : Production and Characterization of NiO Thin Films

3.1 Introduction

Nickel oxide is one of the most common transition metal oxides, with p-type semiconductivity and a large band gap ranging from 3.6 to 4.0 eV (Taşköprü et al., 2015). To acquire diverse properties and applications for NiO, researchers have undertaken the process of doping in NiO. The incorporation of impurity atoms into NiO has contributed to its extensive use in various technological applications in microelectronics and optoelectronics. Recently, lithium (Li) and other transition metal (TM)-doped NiO nanomaterials have garnered attention from several researchers. However, the nonlinear optical properties of thin films, which are particularly interesting as building blocks for optoelectronic applications, have not received attention in many papers on thin films containing Li-doped NiO (Gandhi et al., 2013; Shaaban et al., 2016). This work employed spray pyrolysis to develop nickel oxide thin films doped with lithium (Li). NiO nanoparticles made by spray pyrolysis were examined for their optical and structural characteristics. Additionally, UV-Vis spectroscopy is used to discuss a variety of linear and nonlinear optical characteristics.

3.2 Fabrication of Nickel Oxide (NiO) Thin Films

3.2.1 Setup of Spray Pyrolysis Technique

Spray pyrolysis is an important technique in which a thin film is deposited on the substrate by spraying a precursor solution on a heated surface. A large amount of the work reported using this technique is concerned with semiconductors, metal and transparent conductive oxides (TCO's) related to their electrical conductivity characteristics. In particular, in the case of TCO's and their relevance for photovoltaic applications, a considerable amount of effort was set to optimize their optical transparency in the visible and electrical conductivity characteristics. This was the case for NiO. To obtain thin layers of NiO, we used the existing laboratory-scale SPT system (VTRS) at Echahid Hamma Lakhdar University - El Oued - as shown in Figure 3.1. Here's a general outline of how to set up an SPT system:

- **Substrate**: Thin-film components are constructed upon this base. Thin films are usually deposited over a wide variety of substrates such as glass, concrete, or metal, which are examples of common solid substrates that the film can be deposited on. Glass slides measuring 75 x 25 x 1 mm^3 are the substrates employed in our work since they are readily available, reasonably priced, and enable us to examine film characteristics, particularly optical ones. However, the glass has a thermal expansion coefficient similar to that of nickel oxide

(NiO), which lessens the surface stresses transferred to the produced film from the substrate's surface (Ghougali, 2019).

- **Spray Nozzle:** It is the source that is utilized to spray the first solution, which is converted into tiny droplets known as aerosols by the nozzle. The substrates that have been warmed are exposed to these aerosols.
- **Precursor Solution:** The chemical component required to form the thin film should be present in the original solution. The intended thin film determines how the solution forms.
- **Heating Source:** A heat source to enable the sprayed precursor solution's thermal decomposition, such as an oven or hot plate.
- **Gas Source:** A gas source to assist in spraying the solution.
- **Pressure Control System:** To adjust the gas flow.
- **Temperature Controller:** It is used to control and monitor the heating temperature.
- **Exhaust System:** It is used to direct any by-product gases resulting from the pyrolysis reaction.

Figure 3.1. Experimental setup of spray pyrolysis Technique.

3.2.2 Steps for Thin Film Deposition

Thin film deposition is the sequence process of creating and depositing thin film coatings onto a substrate material.

- **Substrate Preparation:** The glass substrates need to be cleaned and cleared of any debris, grease, and scratches before the deposition of pure and doped NiO thin layers. Preparing the substrates for deposit is crucial as it affects the adhesion, homogeneity, and uniformity of the deposited layers' thicknesses.
- **Preparation of Precursor Solution:** The necessary chemical components are dissolved in an appropriate solvent to create the deposition solution, and the mix of this solution needs to match the material that is going to be deposited as thin films.
- **Spraying Process:** First the appropriate distance must be determined between the sprayer and the glass substrate which is then heated to the desired temperature. After that, the spraying procedure may be started, allowing a thin coating of the intended material to remain on the substrate after the solvent in the precursor solution evaporates.
- **Film Growth:** To get the optimum growth and quality of the intended film, keep spraying the solution. The starting concentration of the solution and the spraying period can also be used to adjust the film thickness.
- **Cooling and Annealing:** To enhance the film quality, the substrate should be cooled and solidified at a particular temperature once film deposition is finished.
- **Characterization:** Lastly, the prepared thin layer was examined and its physical and chemical characteristics were studied utilizing a variety of analysis techniques, including UV-visible microscopy, X-ray diffraction, and other approaches.

3.2.3 Experimental conditions (Deposition Parameters)

For many years, spray pyrolysis has been a process used to produce thin films onto various substrates. The deposition rate is controlled by several spray parameters The spray parameters encompass the following: The type of substrate on which the thin films are to be deposited; the system and substrate temperatures; the distance between the atomizer and the substrate; the amount of initial solution; the duration of the deposition process; the volume and concentration of the solution; and the airflow (Ejaz et al., 2022).

During this work, there are a set of conditions that we have set to obtain nickel oxide layers of good quality. These conditions are:

- The Substrate temperature: 420-500 °C.
- The Quantity of the primary solution: 5 ml.
- Pressure: 1-2 bar
- Sprayer-Substrate distance: 15-25 cm.
- The Deposit time: 15-20 min.

3.2.4 Experimental Methodology

3.2.4.1 Preparation of Solutions

As we've seen previously, during the precursor solution preparation phase, which is the initial stage in the deposition of NiO thin films, some variables, including molarities, solvents, and precursors, can influence the quality of the obtained thin films. The major precursors for NiO thin film deposition include nickel chloride, nickel acetate, nickel nitrate, nickel hydroxide, nickel sulfate, and nickel formate. The three most popular and widely accessible precursors are nickel chloride, nickel nitrate, and nickel acetate (see Table 3.1). The pyrolytic decomposition for NiO film formation for a various precursor is provided by the following equations.

- **Nickel chloride precursors**

The pyrolytic decomposition for NiO film formation for a chloride precursor is given by the equation below (Kamal et al., 2005):

$$NiCl_2.6H_2O \xrightarrow{heat} NiO\downarrow + 2HCl\uparrow + 5H_2O\uparrow \quad (3\text{-}1)$$

- **Nickel nitrate precursors**

The pyrolytic decomposition for NiO film formation for a nitrate precursor is given by the equation below (Juybari et al., 2011):

$$Ni(NO_3)_2.6H_2O \xrightarrow{heat} NiO\downarrow + 2NO_2\uparrow + \frac{1}{2}O_2\uparrow + 6H_2O\uparrow \quad (3\text{-}2)$$

- **Nickel acetate precursors**

The reaction process is expressed as decomposition of nickel acetate to clusters of nickel oxide in the presence of water and air oxygen as given in the following equation (Mrabet et al., 2016):

$$Ni(CH_3COO)_2.4H_2O \xrightarrow{heat} NiO\downarrow + 4CO_2\uparrow + 6H_2O\uparrow \quad (3\text{-}3)$$

Table 3.1. information of Nickel types (Zaouche, 2021).

Molecule	chemical formula	Molar mass	Density	Solubility in water
Nickel Chloride	$NiCl_2$	129.5994 g/mol	3.55 g/cm^3	67.5 g/100 mL (25°C)
Nickel Nitrate	$Ni(NO_3)_2$	182.703 g/mol	2.05 g/cm^3	243 g/100 mL (0 °C)
Nickel Acetate	$C_4H_6NiO_4$	176.781 g/mol	1.798 g/cm^3	Easily soluble in cold water, hot water

In this work, a mixed solution was prepared as a NiO precursor by adding a known quantity of nickel (II) hexahydrate [$Ni(NO_3)_2.6\ H_2O$] (which had been weighed using an electronic scale) in a specific volume of double-distilled water (H_2O). Subsequently, the solution underwent extensive agitation using a magnetic stirrer for thirty minutes until obtaining a uniform and transparent green solution. (as seen in Figure 3.2). Subsequently, the solution was applied onto a glass substrate heated to 480°C. The solution then becomes usable for the SPT.

The mass of nickel (II) nitrate hexahydrate [$Ni(NO_3)_2.6\ H_2O$] is calculated using the expression (3-4), which yields the mass of nickel nitrate (g) as a function of the molar mass M(g/mol), the molar concentration C (mol/L) of nickel nitrate and the volume of double distilled water V(L).

$$m = M.C.V \tag{3-4}$$

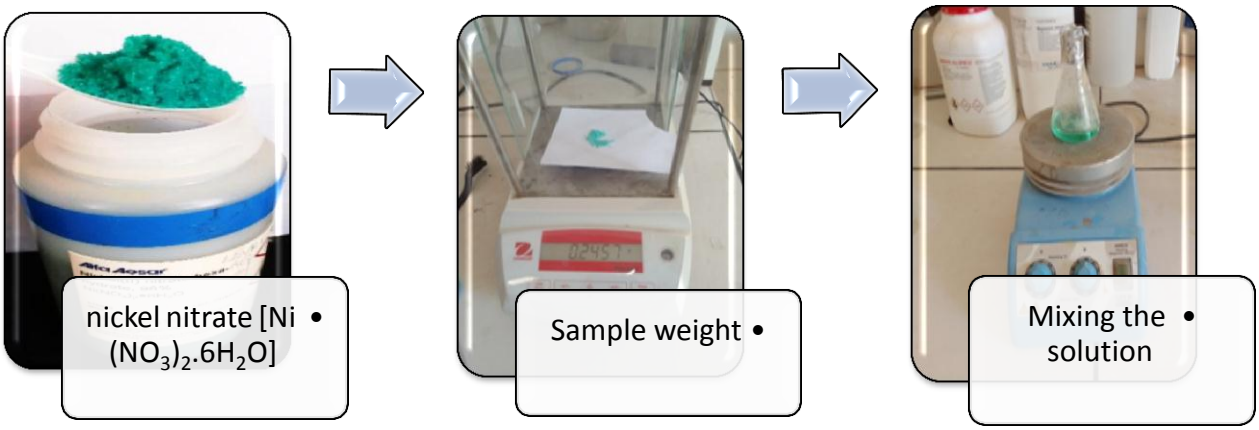

Figure 3.2. Steps to prepare the solution.

3.3 Films Characterization

The films are made nearly identically, with few minor variations in the deposing settings. NiO thin films, both doped and undoped, were deposited on glass substrates. Then, the films were examined by different methods and devices, it has been reported and discussed below.

3.3.1 Effect of Lithium doping NiO thin films

The effects of Li doping on the optical and structural properties of NiO have been briefly studied (Gandhi et al., 2013; Ibrahim et al., 2013). Consequently, it is imperative to investigate the structural, linear, and nonlinear optical (NLO) characteristics of NiO thin films in detail. Li-doped NiO thin films were prepared with SPT in this part. Thin films have been doped at certain atomic ratios to improve their physical properties. The consequences of this doping on the films' structural and optical characteristics have been investigated and are presented in the following.

3.3.1.1 Preparation of samples

In this investigation, and in order to precipitate NiO and Li-doped NiO thin films on glass substrates using nickel nitrate [Ni $(NO_3)_2.6H_2O$], spray pyrolysis was employed. To obtain 0.5 mol\L solution concentration, 0.025 M nickel nitrate was dissolved in 50 ml of distilled water to prepare the spray solution. Various concentrations of (CH_3COOLi) precursor (1, 2, 3, and 5 at %) were used to prepare Li-doped NiO solutions. A uniform and green solution was obtained, and the combined solution was agitated for thirty minutes using a magnetic stirrer. Then comes deposition onto a glass layer that changes in temperature and is controlled by a digital controller to remain at 480°C. For optimal film uniformity, the solution was sprayed via a nozzle with a uniform flow while compressed air was held at a constant pressure. After deposition, the prepared samples are lastly allowed to settle to the proper temperature and complete the crystal growth process, which produces a film with fewer crystal flaws.

3.3.1.2 Devices and measurements

An essential part of thin film science and technology is the convenient characterization of the film properties, which extends from scientific study to quality control in industry. The properties of thin films often differ considerably from the properties of bulk materials of the same nominal composition. An overview of thin film properties is presented in this chapter and the techniques available to characterize them. Two groups of properties are discussed: First, structural properties (thickness, topography, crystal structure, microstructure, chemical

composition) of pure and Li-doped NiO thin films, in the present work, the measurements were carried out using X-ray diffractometer (Philips X'pert pro-2-X). The diffractometer's radiation (λ = 0.15405 nm˚ /Cu Kα) and energy incidence (30 kV and 30 mA), the angle scanning (2θ) value was between (20 - 80˚). Second, optical properties (Absorbance, transmittance, reflectance, gab and Urbach energies, refractive index). The Shimadzu (UV-VIS Spectrophotometer) (Model 1800) working with wavelength range 200-900 nm was used to examine the optical characteristics of the films that were obtained. Based on the optical data, various linear and nonlinear optical properties will be calculated and discussed.

3.3.1.3 Results and discussions

3.3.1.3.1 Structural properties

The crystalline structure of the undoped and Li-doped Nio thin films was investigated using X-ray diffraction in the range of 2θ = 20° − 80°. Where Figure 3.3 displays the XRD results. Diffraction peaks were registered and compared to the (ICDD Card No. 00-047-1049) reference data file. It is worth noting that no peaks related to other crystalline phase (such as Ni_2O_3) are found in these spectra at the resolution limit of the apparatus, indicating that the structures of Li-doped NiO are not altered by the incorporation of lithium. Also, there are no peaks related to other phases such as lithium oxide in these XRD spectra which is probably related to low Li content. In addition to employing Bragg's law, the lattice constants were determined to be a=b=c= 4.1766 Å, 4.1821 Å, 4.1821 Å, 4.1829 Å, and 4.1839 Å for pure and 1, 2, 3, and 5 at% Li samples. These values align closely with those reported in earlier reports (ICDD 00-047-1049). As a consequence, the belonging of the deposited thin film structure to the cubic crystal system was emphasized with the space group (Fm-3m). A noticeable increase in the lattice constant values was observed upon introducing Li doping into the host grid. This phenomenon can be attributed to the substitution of nickel (Ni^+) ions with lithium (Li^+) ions, seen to the verity that the ionic radius of Li^+ (76 pm) is large compared to that of Ni^+ (69 pm) (Shkir et al., 2020). Additionally, this study shows that in all the prepared thin films, there are two principal deviation peaks, the first emerged at 2θ = 37° corresponding to the (111) crystal plane, and a second peak at 2θ = 43° corresponding to the (200) crystal plane. It was clear that the doping level increases the intensity of the peaks. It was also noticed that the reflection peak at (200) is higher intensity than others, suggesting that thin film deposition and growth were occurring at this plane. These experiments have demonstrated that the degree of crystallization increases with increasing doping concentration.

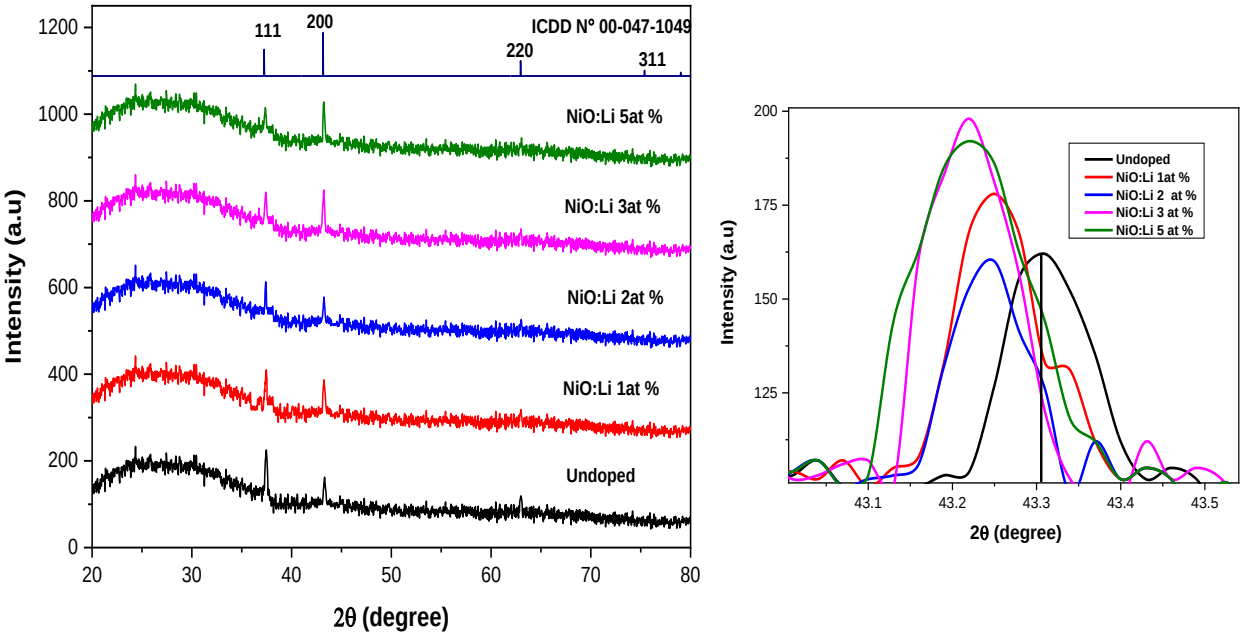

Figure 3.3. XRD pattern of the undoped and Li-doped NiO thin films.

Based on the above observations, it seems that the addition of Li doping has an insignificant impact on the NiO structure, except for the variations in peak intensity and full width at half-maximum (FWHM). Furthermore, there is a tiny variation in the apex location, which is predicted to be caused by the surface thickness, film composition, and grain boundaries, as all of these variables affect the experimental results (Shkir et al., 2020). The incorporation of Li in the NiO network causes an internal micro-strain and microstructural disorder, exposing the XRD diffraction peaks and lowering the grain growth (Shkir et al., 2020; Shaaban et al., 2016). Utilizing the XRD data, other various parameters such as lattice strain, crystallite size, and dislocation density can be calculated using respectively the following formulas (El-Bana et al., 2017; Shkir et al., 2017; Alfaify and Shkir, 2019):

$$D = \frac{0.9\lambda}{\beta \cos(\theta)} \tag{3-5}$$

$$\varepsilon = \frac{\beta \cos\theta}{4} \tag{3-6}$$

$$\delta = \frac{1}{D^2} \tag{3-7}$$

Here β is (FWHM), λ is X-ray wavelength and θ denotes the Bragg angle.

All the parameters are registered in Table 3.2. An increase in the size of the crystallites in the NiO lattice has been observed at Li doping concentrations of 1 at% and 2 at%. This verity suggests that crystallization is improved, which may be explained by the fact that Li^{+} is slightly larger and has a lower charge than Ni^{2+} (Bhatt et al., 2020). In the films prepared under these conditions, we also observed a significant decrease in lattice strain and dislocation density. For thin films fabricated with 3 at% and 5 at% Li contents as dopants. It should be noted that the average D value decreases as the sample's micro strain increases. This suggests that there are more defects and dislocations in the deposited films (Shkir et al., 2020; Shaaban et al., 2016).

Table 3.2. Structure parameters for undoped and doped prepared samples.

Sample (doping %)	2θ (°)	hkl	FWHM	Crystallite size D (nm)	Lattice strain, ε ($\times10^{-4}$)	Dislocation density, δ ($\times10^{-4}$ nm^{-2})	A (Å)	V $(Å)^3$
ICDD 00-047-1049	43.276	2 0 0	-	-	-	-	4.1771	72.882
Pure NiO	43.306	2 0 0	0.122	70.061	4.947	2.037	4.1766	72.857
1 % Li–NiO	43.249	2 0 0	0.113	75.626	4.583	1.748	4.1821	73.146
2 % Li–NiO	43.244	2 0 0	0.115	74.309	4.664	1.810	4.1821	73.146
3 % Li–NiO	43.219	2 0 0	0.133	64.247	5.395	2.422	4.1829	73.190
5 % Li–NiO	43.223	2 0 0	0.137	62.372	5.575	2.570	4.1839	73.243

Figure 3.4 illustrates the unfavorable impact of crystalline defects, including strains and dislocations, on the average crystallite size at different Li doping concentrations. A noticeable correlation exists between alterations in mean strain and dislocation. Both have a detrimental effect on the crystallization of the prepared thin films.

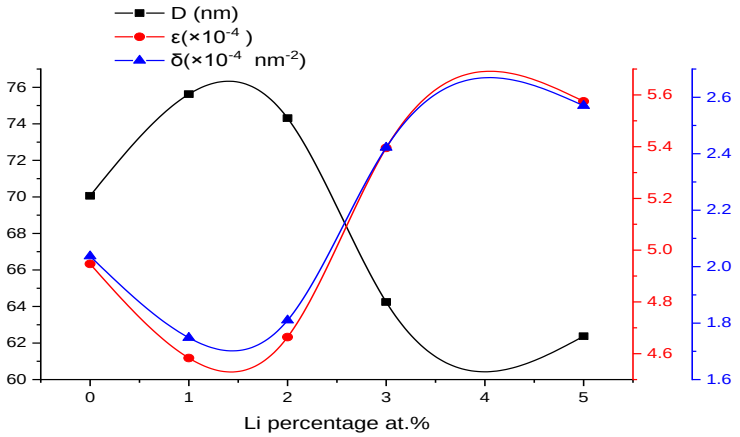

Figure 3.4. Correlation among crystallite size, lattice strain, and dislocation density in Li:NiO films with Li content.

3.3.1.3.2 Linear Optical Properties

a) Absorbance, transmittance and reflectance analyses

As is well known, exploration of optical properties, such as absorbance, transmission and reflectance is essential for optoelectronic materials. Figure 3.5 shows the transmittance spectra of the elaborated NiO thin films undoped and doped with Lithium. The transmittance spectrum of the films shows an important value ranging from 60% to 80% depending upon the doping concentration in the visible region. The average optical transmittance in the visible region found its value in the range of 80% for pure NiO, then decreases gradually for samples of Li-doping NiO to reach 60% for NiO doped with 2at% and then increases for the sample with 5at %, which exhibits better transparency. Several previous studies have shown this behavior (Ibrahim et al., 2013; Liu et al., 2011). In addition to the crystalline structure and sample thickness, which both significantly alter the optical transmittance, other parameters that may affect the transmittance of the doped thin layer include flaws resulting from sample preparation. The reduced transparency may be attributed to the surface defects and structural factors already mentioned previously in the structural study and included in Table 3.2, or may be attributed, to the increased scattering of photons by an increase in roughness of surface morphology (Shkir et al., 2020). While the large increase in transmission for 5 at% Li:NiO thin film may be resulted from the impact of micro strain, the reduction in crystallite size (Table 3.2), and the excitation of plasma on the films (Yang et al., 2016).

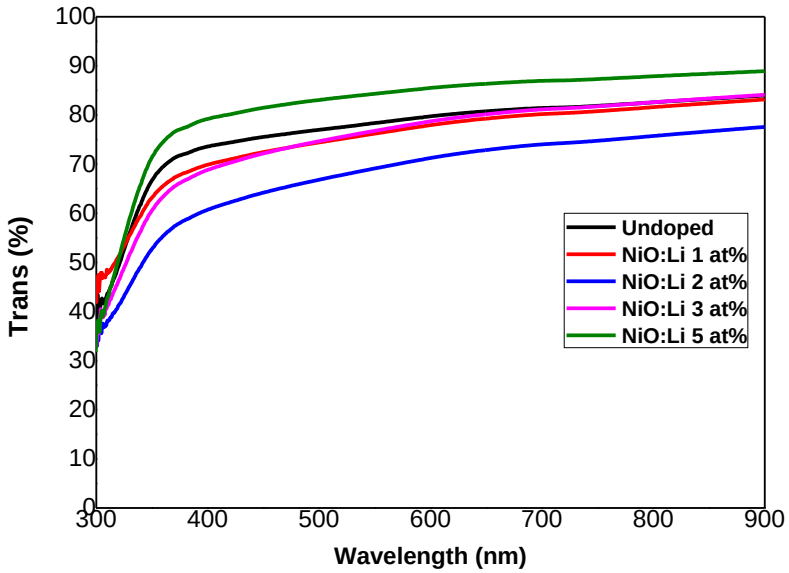

Figure 3.5. The optical transmittance of pure and Li-doped NiO thin films.

In visible and near-infrared regions, all films exhibit excellent optical transparency or very little absorption and reflection. It is evident that when the concentration of Li doping level increases, the permeability falls, whereas Figure 3.6 shows that the reflectivity and absorption exhibit the opposite behavior of optical transmittance (Ibrahim et al., 2013; Liu et al., 2011). Regarding the absorption of the thin NiO films in the UV, as shown by the statement in Fig. 3.6 (a-b), it is associated with the absorption of the optical bandgap in the NiO, as the absorption was roughly in the wavelength range of 350–400 nm. Doping Li with level ranging from 0 to 3 at% results in an increase in absorption, which declines at 5 at%.

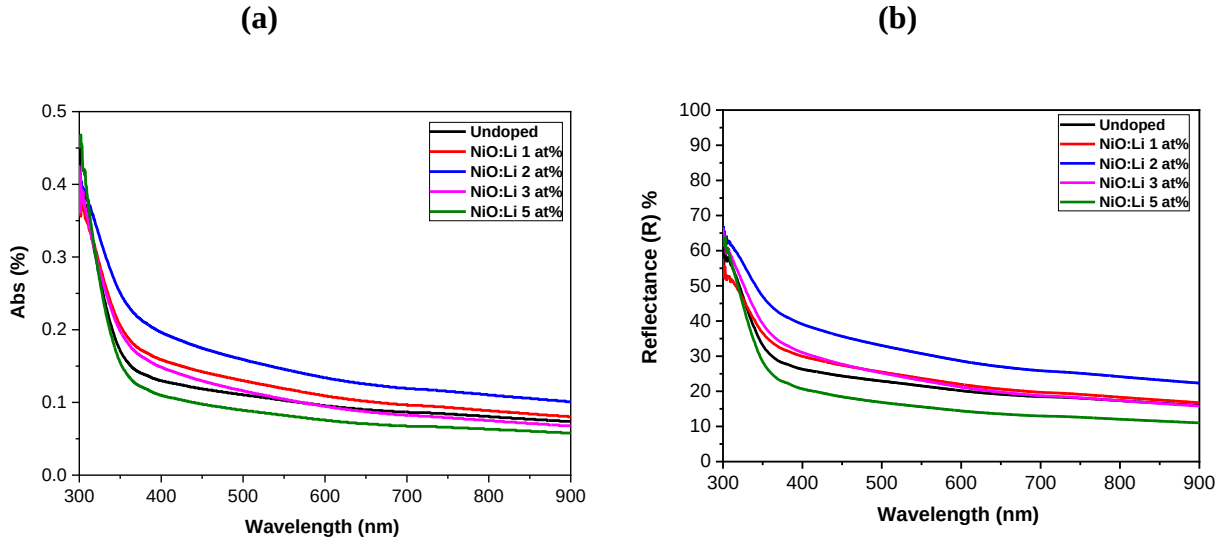

Figure 3.6. (a) The absorption spectra of the undoped and Li-doped NiO thin films, (b) The reflectance spectra of the undoped and Li-doped NiO thin films.

b) Optical bandgap and Urbach energy analysis

The band gap energy of a semiconductor describes the energy needed to excite an electron from the valence band to the conduction band. Thin films band gap's is a fundamental property that characterizes the component material for many optoelectronic applications. The optical band gap of undoped and doped NiO thin films can be estimated from the plot of $(\alpha h\nu)^2$ as a function of photon energy (hv). According to Tauc's relation for direct bang gap semiconductor as we have seen previously (Shkir et al., 2018).

The optical band gap (Eg) for pure and doped NiO films values were determined by extrapolating the straight-line portion, of the plot $(\alpha h\nu)^2$ versus (hv) to the energy axis $(\alpha h\nu)^2 = 0$ (where α is the absorption coefficient and hv is the photon energy) as illustrated in Figure 3.7. The linearity of the graph suggests the presence of the direct allowed transitions. The obtained

band gap values for pure NiO films and NiO doped with various lithium percentages are summarized in Table 3.3.

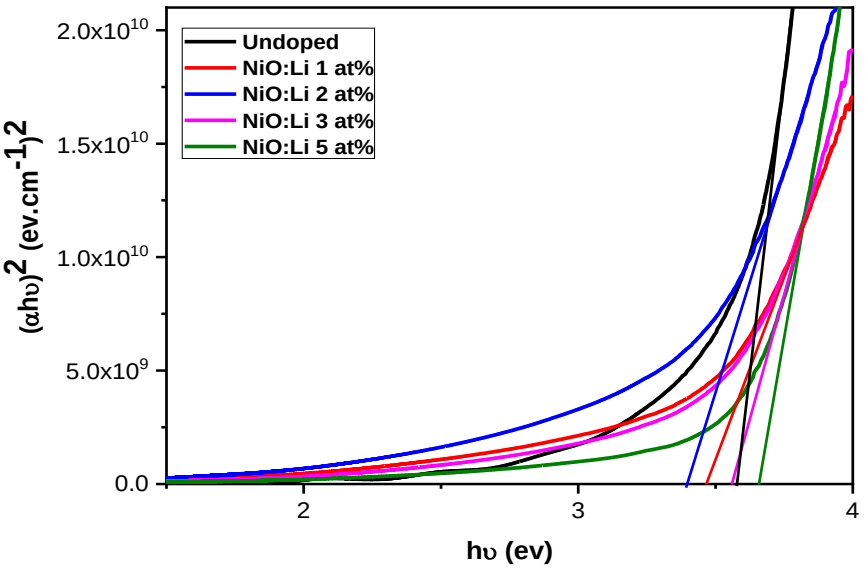

Figure 3.7. Plot of $(\alpha h\nu)^2$ versus incident photon energy (hv) of undoped and Li-doped NiO thin films with different lithium percentages.

Table 3.3. Optical gap values of Li doped NiO thin films.

Sample	Eg (eV)
Pure NiO	3.59
1% Li–NiO	3.46
2% Li–NiO	3.38
3% Li–NiO	3.56
5% Li–NiO	3.66

As can be seen from the Table 3.3, the direct bandgap values of the deposited films were determined, and were fond to be in the range of 3.38 - 3.66 eV, as recorded in Table 3.3. These values clearly suggest a reduction in the bandgap value for Li-doped NiO films at 1% and 2%. This decrease is anticipated due to the larger crystallite size, compared with Li-doped NiO films at 3% and 5%, where a decline in crystallite size was noted, resulting in an augmentation of the bandgap. The variation in the bandgap is also affected by the number of charge carriers, disturbances, and defects (Table 3.2) (El Radaf et al., 2019). Furthermore, reducing the bandgap

might result in raising the Urbach energy. To this end, Urbach energy (E_u) has been derived using Urbach's empirical formula (Igweoko et al., 2018):

$$\alpha = \alpha_0 \exp\left(\frac{h\vartheta}{E_u}\right) \quad (3\text{-}8)$$

Where hv is photon energy, α represents the experimentally deduced from optical absorption profile, α_0 is a characteristic constant of matter, and (E_u) is the band tail width commonly called Urbach energy. The band tail width is also related to the disorder in the film network. Graphical representation of the function Ln(α) as a function of (hν) (Fig. 3.8) is used to calculate E_u values, and Table 3.4 presents the obtained values, these values are calculated from the inverse slope of the linear plot of ln(α) versus (hν). Figure 3.9 displays the bandgap and Urbach energy variations as a function of lithium doping concentration. The bandgap and Urbach energy have been demonstrated to be inversely related (El Radaf et al., 2019). This behavior indicates that the obtained optical band gaps are governed essentially by the disorder variations in such films.

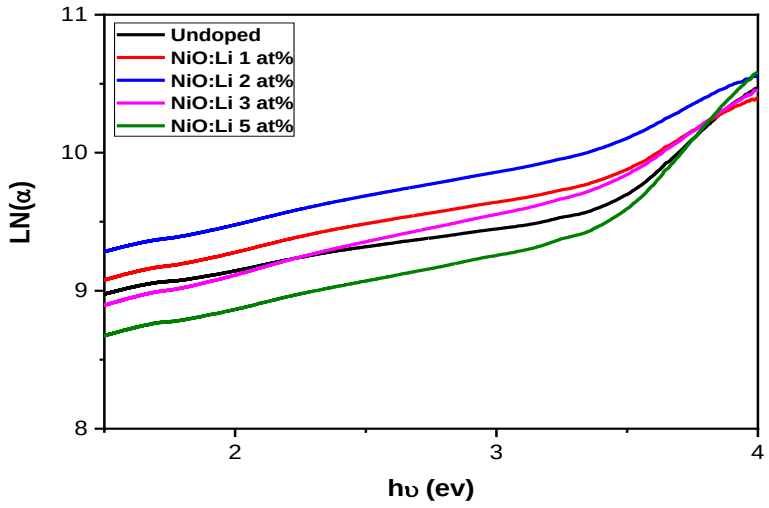

Figure 3.8. Plot of Ln(α) versus (hν) of undoped and Li-doped NiO thin films with different lithium percentages.

Table 3.4. Estimated values of Urbach energy and optical bandgap.

Sample	E_u (ev)	E_g (ev)
Pure NiO	0.22	3.59
1% Li–NiO	0.23	3.46
2% Li–NiO	0.24	3.38
3% Li–NiO	0.19	3.56
5% Li–NiO	0.18	3.66

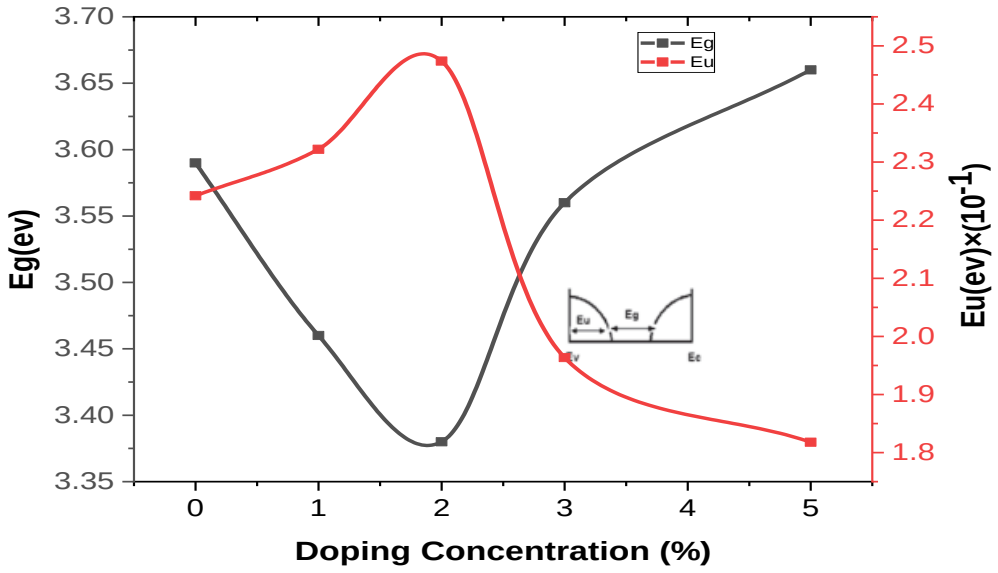

Figure 3.9. Variations of the Optical band gap (Eg) and Urbach energy (E_u) with Li content.

c) Refractive index and extinction coefficient analyses

Refractive index (n) and extinction coefficient (k) are two optical parameters of importance that were measured to obtain much better information and insight on the polarization and structural changes in the produced films as a result of doping (Shkir et al., 2018). The extinction coefficient k expresses the attenuation of light in the medium and is a key factor in determining several/many optical parameters, such as light absorption and dielectric constants in a medium. The equation used to calculate the extinction coefficient (k) for pure and Li-doped NiO films using the wavelength and absorption coefficient values as below (El Radaf et al., 2019):

$$k = \alpha\lambda/4\pi \tag{3-9}$$

The relationship that exists between extinction (K) and reflection (R) was also used to calculate the refractive index (n) (El Radaf et al., 2019).

$$n = \frac{(1+R)}{(1-R)} + \sqrt{\frac{4R}{(1-R)^2} - K^2} \tag{3-10}$$

Figure 3.10, exhibits the plots of variation of (a) extinction coefficient (k) and (b) refractive index (n) as function of the wavelength. Both curves indicate a similar behavior. It is observed in Figure 3.10a that the extinction coefficient (K) value decreases with wavelength increasing and increases with concentration (1, 2, and 3 at%) of the Li doping content. The values of k range between approximately 0.11 and 0.01, illustrating the impact of Li doping on

NiO thin films. The lower values of (k) show the absence of significant flaws on the surface of the thin film. Because this type of quality permits the production of less faulty films, it may be widely used in energy devices like solar cells and photovoltaic systems (Taşköprü et al., 2016). It is observed in Figure 3.10b that the refractive index (n) increased when adding lithium doping and decreased when the wavelength raised, which represents a normal dispersion . A higher refractive index is achieved with a 2 at% Li content in the NiO thin film. This is attributed to the increased polarization of lithium atoms within the host lattice matrix of NiO. A similar outcome was also reported by Shaaban et al. in Co-doped ZnO thin films (Shaaban et al., 2016).

(a) **(b)**

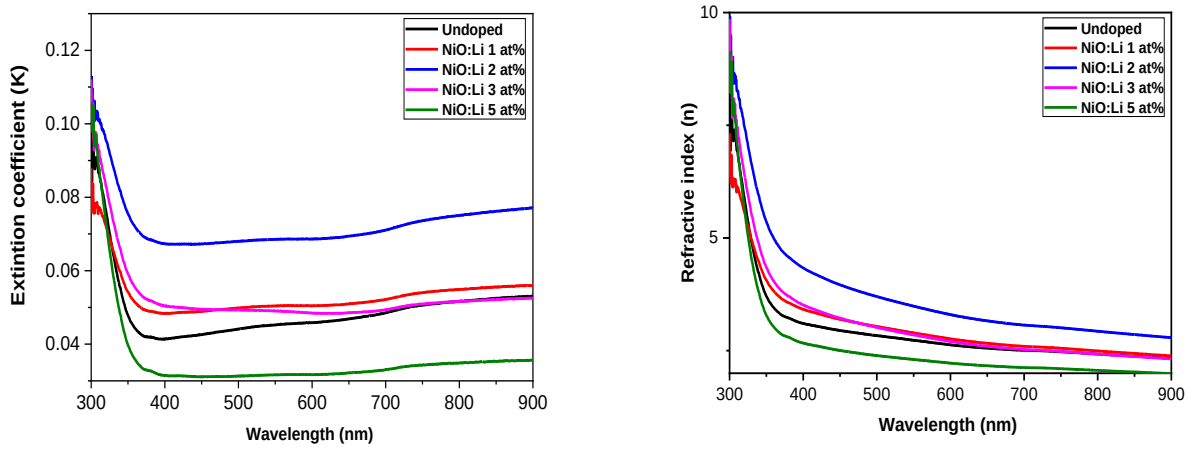

Figure 3.10. Variation of (a) extinction coefficient and (b) refractive index for undoped and Li-doped NiO films.

3.3.1.3.3 Dielectric studies

Any material's thin film electron excitation spectrum may be explained by the real (ε_1) and imaginary (ε_2) components of the optical dielectric constant. The complex dielectric constant, ($\varepsilon = \varepsilon_1 + \varepsilon_2$), was used to calculate these constants. The reduction in light speed and absorption of energy from the electric field owing to the dipole motion of particles in a material is represented by (ε_1) and (ε_2) (Usha et al., 2013). The relations listed below were utilized to compute the aforementioned parameters (Kim et al., 2012):

$$\varepsilon_1 = n^2 - k^2 \quad (3\text{-}11)$$

$$\varepsilon_2 = 2nk \quad (3\text{-}12)$$

Figure 3.11(a-b), displays the variation of ε_1 and ε_2 as a function of Li: NiO thin film concentrations. This graph demonstrates that these parameters ε_1 and ε_2 behave like (n) and (k). They have larger values at shorter wavelengths and are constant at longer wavelengths. As a result, it is possible to consider this good optical response to films (Usha et al., 2013). We observe that when the doping ratio increases, the dielectric constant of the produced films increases, demonstrating the effect of Li in pure NiO.

(a)

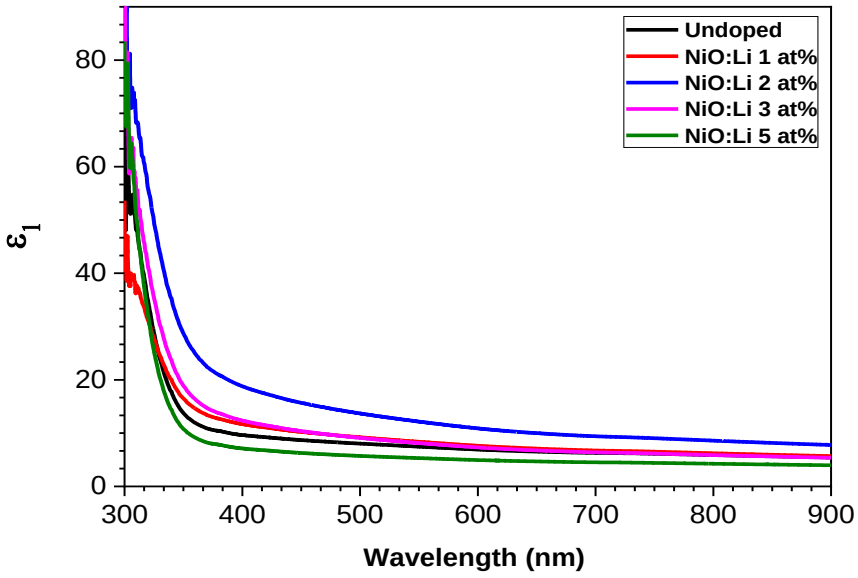

(b)

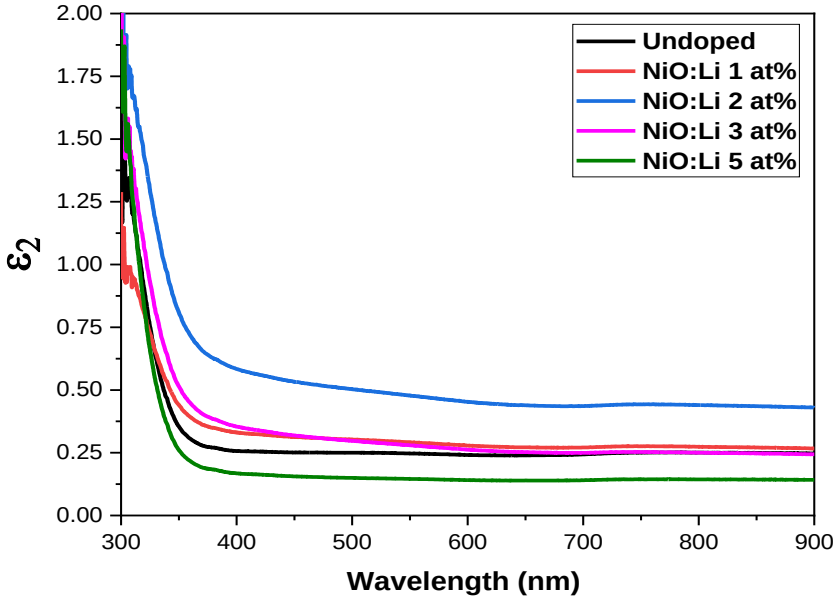

Figure 3.11. (a) and (b) Variations in ε_1 and ε_2, respectively, of NiO thin films as a function of wavelength.

3.3.1.3.4 Refractive index dispersion analyses

The collected refractive index data can be analyzed using the Wemple-DiDomenico single oscillator model which describes the dielectric response for transitions below the optical gap. In this model, the refractive index varies with incident photon energy, according to (Caglar et al., 2007; Borah and Mostako, 2020):

$$n^2(h\vartheta) = 1 + \frac{E_d E_0}{(E_0^2 - (h\vartheta)^2)} \quad (3\text{-}13)$$

The WDD model provides a physical interpretation of the sample through the constants E_0 and E_d. Here, $h\vartheta$ is the incident photon energy, E_0 represents the average bandgap parameter, also known as the single oscillator energy, while E_d is the dispersion energy which is a measure of the strength of inter-band optical transitions. The plotting of $(n^2\text{-}1)^{-1}$ versus $(hv)^2$ (Fig. 3.12) permits us to determine these oscillator parameters. by that means, the values of E_0 and E_d were calculated from the slope of the linear relation corresponds to $(E_0E_d)^{-1}$, and the intersection with the vertical axis represents (E_0/E_d). Additionally, the static refractive index "n_0" and the bandgap of Wemple-DiDomenico were determined using the following relationships (El Radaf et al., 2019):

$$n_0 = \sqrt{1 + \frac{E_d}{E_0}} \quad (3\text{-}14)$$

$$E_g^{wmp} = \frac{E_0}{2} \quad (3\text{-}15)$$

The acquired values of E_g, E_d, E_0, n_0, E_g^{wmp} (measured from wimple), and the E_0/E_g ratio of the films are shown in Table 3.5. These findings indicate that the values of the dispersion coefficients E_g, E_d, E_0 and n_0 reduced proportionally when the concentration of lithium in the NiO films increased. This might be because of variations in the ionicity bonds.

Moreover, it is found that the values of dispersive energy are lower than those attained for the undoped film. This behavior can be explained by the change in the type and number of chemical bonds and their bonding energy caused by the doping Li ions incorporation in the host lattice.

In addition to the dependence of the E_d parameter with Li concentration, the value of the single oscillator energy E_0 of the films, representing the average energy gap as reported in various sources, is closely correlated with the optical energy gap through an empirical formula:

$E_0 \approx 1.3Eg$. This result aligns with the relationship attained by the single oscillator model ($E_0 \approx 1.4Eg$) (Caglar et al., 2007; Borah and Mostako, 2020).

Using the dispersion energy E_d and the oscillator energy E_0, the optical spectra moments M_{-1} and M_{-3} for both undoped and Li-doped NiO films are calculated using the following equations (El Radaf et al., 2019):

$$M_{-1} = \frac{E_d}{E_0} \qquad M_{-3} = \frac{M_{-1}}{E_0^2} \qquad (3\text{-}16)$$

The moment values of the films have been calculated and presented in Table 3.5. From this Table, we observe that the moments of the optical spectra M_{-1} and M_{-3} increase progressively with Li doping concentrations of (1 and 2 at%). But they decrease when the Li percentages added are (3 and 5 at%).

Table 3.5. Parameters of a single oscillator applicable to all Li-doped NiO films.

Li at%	E_d (ev)	E_0 (ev)	n_0	M_{-1}	M_{-3} (ev^{-2})	E_g^{wmp}	E_0/E_g
0	207.07	4.599	6.784	45.026	2.128	2.299	1.28
1	202.86	4.286	6.951	47.325	2.575	2.143	1.24
2	348.12	4.693	8.670	74.178	3.368	2.346	1.39
3	182.84	4.143	6.718	44.132	2.571	2.071	1.17
5	124.5	4.295	5.476	28.987	1.571	2.147	1.18

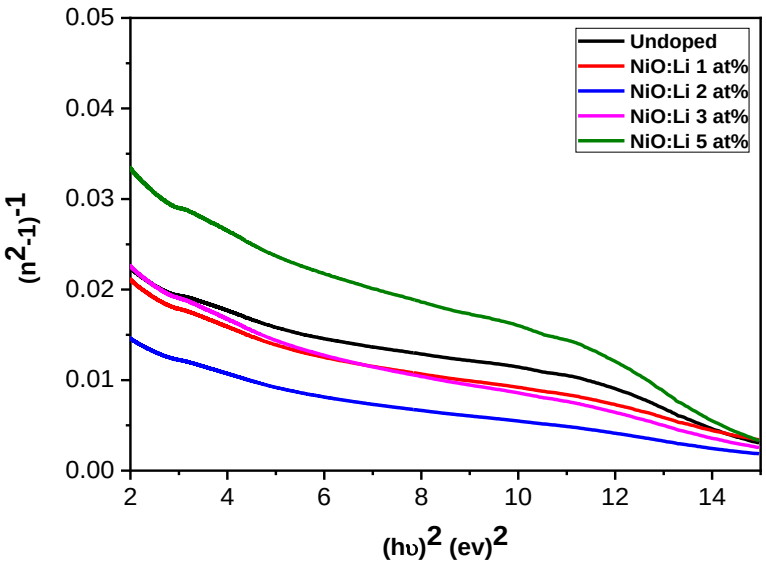

Figure 3.12. Variation of $(n^2\text{-}1)^{-1}$ versus $(h\nu)^2$ for all Li-doped and undoped NiO films.

3.3.1.3.5 Nonlinear Optical Properties

Materials exhibit nonlinear optical properties caused by variation of induced electronic polarization with the applied electric field. In the optoelectronic systems domain, the nonlinear optical parameters have attracted significant attention. This nonlinear optical behavior of a material is reflected in its changes in optical reflectivity, absorption, refractive index, etc., with incident light intensity. The two main parameters that characterize the nonlinear properties of the studied material are the nonlinear refractive index (n_2) and the third-order nonlinear susceptibility (χ^3). The nonlinear response of the material's polarization to the electric field can be explained in terms of the third-order nonlinear susceptibility. On the other hand, the nonlinear refractive index provides a disproportionate response for the material subjected to an electric field (Shkir et al., 2018; El Radaf et al., 2019). To comprehend the nonlinear behavior of the manufactured thin films and observe the impact of Li doping, we have computed the aforementioned parameters.

- **Linear susceptibility $\chi^{(1)}$**

Linear Susceptibility ($\chi^{(1)}$) is associated with the susceptibility of electrons as they move in response to the propagation of light through a medium, referred to as the dipole moment. The electrons within the molecular structure of an atom oscillate in reaction to an oscillating electric field. When a molecule experiences a linear restoring force concerning its electrons around the nucleus, the response will exhibit linearity. In mathematical terms, susceptibility is considered to have both real and imaginary components. The complex dielectric is defined as $\varepsilon = \varepsilon_1 + i\varepsilon_2$, where $\varepsilon_1 = n^2 - k^2$ and $\varepsilon_2 = 2nk$ are the real and imaginary parts respectively. While the imaginary component of susceptibility is linked to the absorption of the medium, the real component of susceptibility determines the optical propagation velocity in the medium. The refractive index is closely tied to linear susceptibility and can be calculated using the following equation (Noblet and Humbert, 2019; Abdel-Galil et al., 2020):

$$\chi^{(1)} = (n^2 + 1)/4\pi \qquad (3\text{-}17)$$

Figure 3.13 depicts the (χ^1) graph as a function of energy. Analysis of this graph reveals a consistent trend among all samples, wherein the χ^1 value increases with rising incident photon energy, ultimately reaching saturation at a specific wavelength. Furthermore, these sensitivities exhibit an augmentation with higher concentrations of Li doping. The observed χ^1 values fell within the range of 4 to 25 esu. In comparison to previously published results on other thin films,

the measured linear optical parameter is rather high, suggesting that Li is significantly influencing NiO and being beneficial for a variety of optical device applications (Alfaify and Shkir, 2019).

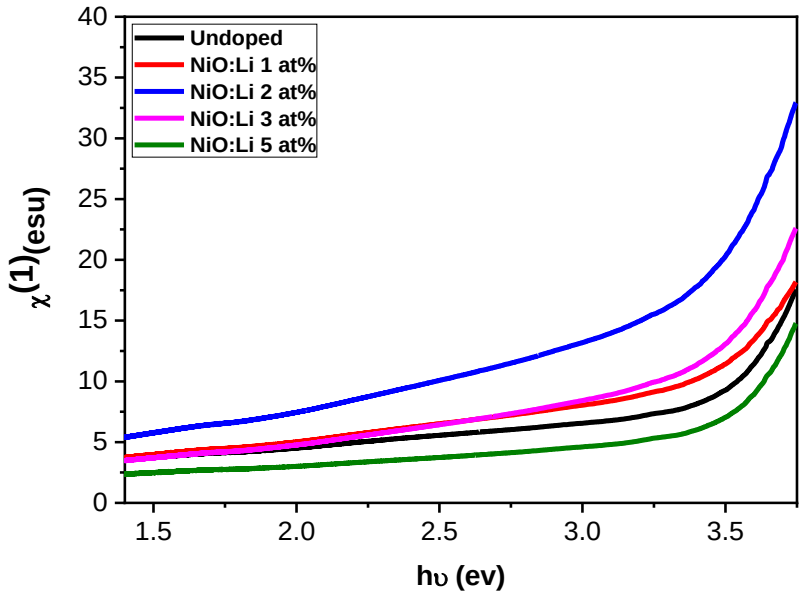

Figure 3.13. Variation of Linear Susceptibility versus photon energy of all Li: NiO films.

- **Third-order nonlinear optical susceptibility $\chi^{(3)}$**

Media with optical nonlinearity are defined by a non-linear reaction of the medium to the electric field. Nonlinear optical (NLO) interactions in crystals involving third-order susceptibility $\chi^{(3)}$ are extensively studied and practically valuable due to their relevance to various optical systems and optical information processing. Third-order susceptibility plays a vital role in photonics as it manifests a wide range of phenomena related to switching. Utilizing the formula for linear susceptibility (χ^1), the determination of nonlinear susceptibility (χ^3) can be achieved through the following relationship (Shkir et al., 2018):

$$\chi^3 = A\left[\chi^{(1)}\right]^4 \tag{3-18}$$

The constant A is mentioned in various references as 1.7×10^{-10} esu.

The nonlinear susceptibility of NiO nanoparticles is illustrated in Figure 3.14. It is observed that χ^3 starts to rise from 5×10^{-7} to 7×10^{-6} esu, with an increase in photon energy from 1.5 eV to 3.6 eV. The fluctuation of third-order nonlinear optical susceptibility values for NiO films deposited with various concentrations of Li (1, 2, 3, and 5 at%) concerning the

incoming beam is shown in Figure 3.14. A greater nonlinear susceptibility is achieved with a 2% Li content in the NiO thin film. This can be attributed to the increased polarization of Li atoms within the host lattice matrix of NiO. It is demonstrated that an increase in Li doping concentration results in a corresponding enhancement of the third-order susceptibility. According to the analyses, Li-doped NiO films may be technologically essential for laser systems and shorter pulse production (Chtouki et al., 2021).

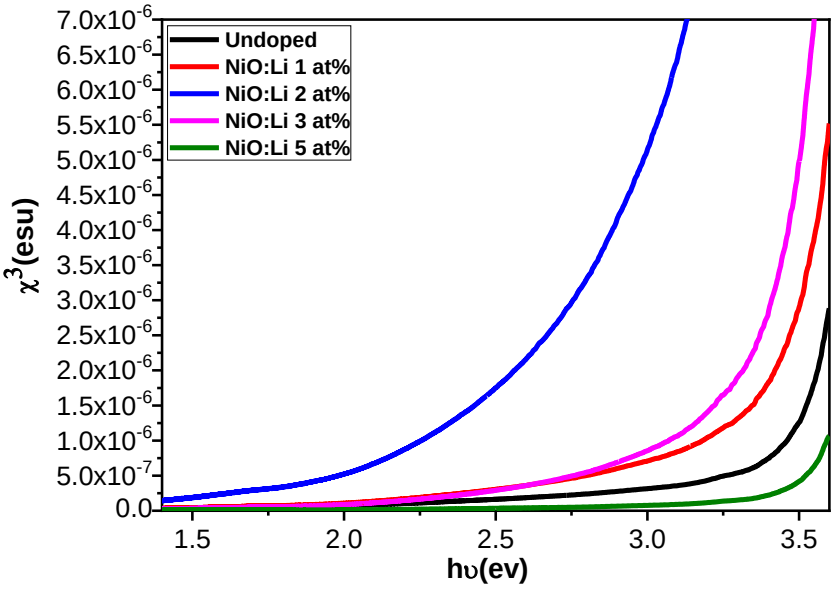

Figure 3.14. Variation of Nonlinear Susceptibility versus energy (hν) of all Li: NiO films.

- **Nonlinear refractive index n_2**

A feature of a substance that explains how it reacts at high-intensity light is called the nonlinear refractive index, or (n_2). It measures the variation in the material's refractive index caused by the intensity of the incoming light. To comprehend the nonlinear optical behavior of materials, one important metric to know is the nonlinear refractive index. The relationship below may be used to compute the nonlinear refractive index (n_2) (Shkir et al., 2021; El Radaf et al., 2019):

$$n_2 = \frac{12\pi\chi^3}{n} \qquad (3\text{-}19)$$

Figure 3.15 displays the plots the variation of the nonlinear refractive index (n_2) versus the photon energy. The nonlinear refractive index values were first discovered to be constant, but when the photon energy roses, they grew as well and eventually became saturated at a certain

wavelength. This kind of change might be brought about by light interactions that result in high polarization within that specific wavelength band. The values of (n_2) were obtained and analyzed based on the doping concentration, fluctuating between 6.5×10^{-6} esu and 4×10^{-4} esu. It was observed that these values increased proportionally with Li doping and exhibited a strong correlation with other properties.

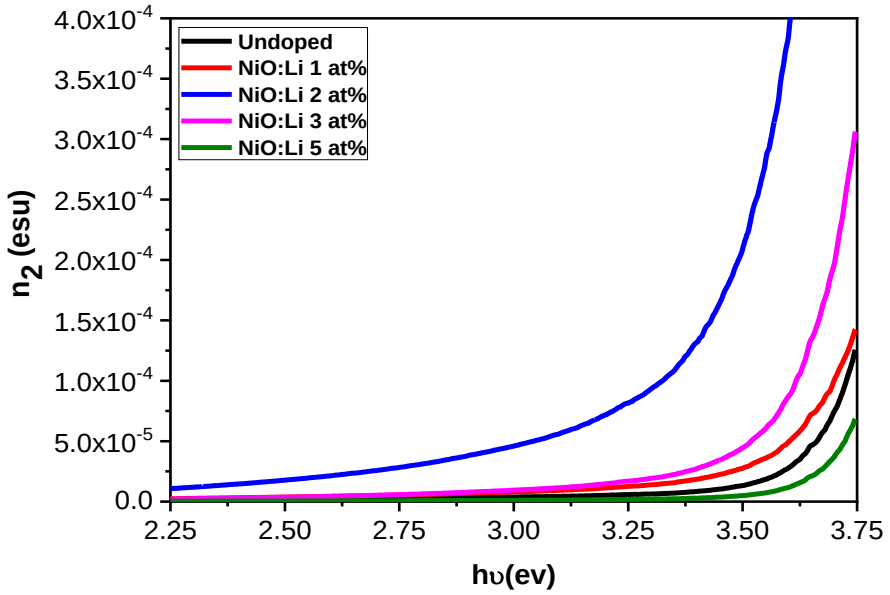

Figure 3.15. Plots of Nonlinear refractive index versus energy (hv) for all Li:NiO films.

3.4 Conclusion

This chapter examined the effect of different concentrations of lithium (Li) on the structural and optical properties of nickel oxide (NiO) thin films generated by spray pyrolysis technology. XRD analysis discloses a polycrystalline cubic structure in the films, primarily growing along the (200) planes. The increase in Li concentration results in a reduction in crystal size but an enhancement in lattice strain, indicating the presence of lattice defects. Optical evaluations, conducted through absorbance and transmittance tests, showcase transmittance levels ranging from 60% to 80% over the 200-900 nm wavelength spectrum. The direct bandgap (Eg) values span from 3.66 to 3.38 eV. Parameters such as n, k, and dielectric constants exhibit a consistent increasing pattern with the addition of Li. The elevation in refractive index is attributed to the integration of lithium into the NiO lattice. Furthermore, the assessment includes the computation of oscillator parameters and refractive index dispersion using the Wemple DiDomenico (WDD) model. Non-linear studies reveal enhancements in χ^3 and n_2 values with Li doping, making them suitable for optoelectronic applications.

References

Abdel-Galil, A., Assiri, M. A., & Yahia, I. S. (2020). Optical analysis of methyl violet thin films/polymeric substrate for flexible organic technology. Optical and Quantum Electronics, 52, 1-20. https://doi.org/10.1007/s11082-020-02491-6.

Alfaify, S., & Shkir, M. (2019). A one pot room temperature synthesis of pure and Zn doped PbI_2 nanostructures and their structural, morphological, optical, dielectric and radiation studies. Journal of Nanoelectronics and Optoelectronics, 14(2), 255-260. https://doi.org/10.1166/jno.2019.2487.

Bhatt, A. S., Ranjitha, R., Santosh, M. S., Ravikumar, C. R., Prashantha, S. C., Maphanga, R. R., & Silva, G. F. L. E. (2020). Optical and electrochemical applications of Li-doped NiO nanostructures synthesized via facile microwave technique. Materials, 13(13), 2961. https://doi.org/10.3390/ma13132961.

Borah, D. J., & Mostako, A. T. T. (2020). Investigation on dispersion parameters of Molybdenum Oxide thin films via Wemple–DiDomenico (WDD) single oscillator model. Applied Physics A, 126(10), 818. https://doi.org/10.1007/s00339-020-03996-3.

Caglar, Y., Ilican, S., & Caglar, M. (2007). Single-oscillator model and determination of optical constants of spray pyrolyzed amorphous SnO_2 thin films. The European Physical Journal B, 58, 251-256. https://doi.org/10.1140/epjb/e2007-00227-y.

Chtouki, T., El Mrabet, M., Tarbi, A., Goncharova, I., & Erguig, H. (2021). Comprehensive review of the morphological, linear and nonlinear optical characterization of spin-coated NiO thin films for optoelectronic applications. Optical Materials, 118, 111294. https://doi.org/10.1016/j.optmat.2021.111294.

Ejaz, H. A. R. O. O. N., Hussain, S. H. A. B. B. I. R., Zahra, M. A. N. Z. A. R., Saharan, Q. M., & Ashiq, S. A. L. M. A. N. (2022). Several sputtering parameters affecting thin film deposition. Journal of Applied Chemical Science International, 13(3), 41-49. http://dx.doi.org/10.56557/jacsi/2022/v13i37590.

El Radaf, I. M., Hameed, T. A., & Dahy, T. M. (2019). Synthesis, structural, linear and nonlinear optical properties of chromium doped SnO_2 thin films. Ceramics International, 45(3), 3072-3080. https://doi.org/10.1016/j.ceramint.2018.10.189.

El-Bana, M. S., El Radaf, I. M., Fouad, S. S., & Sakr, G. B. (2017). Structural and optoelectrical properties of nanostructured $LiNiO_2$ thin films grown by spray pyrolysis technique. Journal of Alloys and Compounds, 705, 333-339. https://doi.org/10.1016/j.jallcom.2017.02.106.

Gandhi, T. I., Babu, R. R., & Ramamurthi, K. (2013). Structural, morphological, electrical and optical studies of Cr doped SnO_2 thin films deposited by the spray pyrolysis technique. Materials science in semiconductor processing, 16(2), 472-479. https://doi.org/10.1016/j.mssp.2012.07.008.

Ghougali, M. (2019). Elaboration and characterization of nanostructuring NiO thin films for gas sensing applications (Doctoral dissertation, University of Mohamed Khider, Biskra). http://thesis.univ-biskra.dz/id/eprint/4617.

Ibrahim, N. B., Abdi, M. H., Abdullah, M. H., & Baqiah, H. (2013). Structural and optical characterisation of undoped and chromium doped tin oxide prepared by sol–gel method. Applied surface science, 271, 260-264. https://doi.org/10.1016/j.apsusc.2013.01.171.

Igweoko, A. E., Augustine, C., Idenyi, N. E., Okorie, B. A., & Anyaegbunam, F. N. C. (2018). Influence of processing conditions on the optical properties of chemically deposited zinc sulphide (ZnS) thin film. Materials Research Express, 5(3), 036413. https://doi.org/10.1088/2053-1591/aab652.

Juybari, H. A., Bagheri-Mohagheghi, M. M., & Shokooh-Saremi, M. (2011). Nickel–lithium oxide alloy transparent conducting films deposited by spray pyrolysis technique. Journal of Alloys and Compounds, 509(6), 2770-2775. https://doi.org/10.1016/j.jallcom.2010.11.075.

Kamal, H., Elmaghraby, E. K., Ali, S. A., & Abdel-Hady, K. (2005). The electrochromic behavior of nickel oxide films sprayed at different preparative conditions. Thin solid films, 483(1-2), 330-339. https://doi.org/10.1016/j.tsf.2004.12.022.

Kim, M. S., Yim, K. G., Son, J. S., & Leem, J. Y. (2012). Effects of Al concentration on structural and optical properties of Al-doped ZnO thin films. Bulletin of the Korean Chemical Society, 33(4), 1235-1241. https://doi.org/10.5012/bkcs.2012.33.4.1235.

Liu, S. J., Chen, L. Y., Liu, C. Y., Fang, H. W., Hsieh, J. H., & Juang, J. Y. (2011). Physical properties of polycrystalline Cr-doped SnO_2 films grown on glasses using reactive dc magnetron co-sputtering technique. Applied Surface Science, 257(6), 2254-2258. https://doi.org/10.1016/j.apsusc.2010.09.083.

Mrabet, C., Amor, M. B., Boukhachem, A., Amlouk, M., & Manoubi, T. (2016). Physical properties of La-doped NiO sprayed thin films for optoelectronic and sensor applications. Ceramics International, 42(5), 5963-5978. https://doi.org/10.1016/j.ceramint.2015.12.144.

Noblet, T., & Humbert, C. (2019). Sum-frequency generation through a unique Feynman diagram formalism: the case of bipartite organic/inorganic complexes. arXiv preprint arXiv:1906.03197. https://doi.org/10.48550/arXiv.1906.03197.

Shaaban, E. R., El-Hagary, M., Moustafa, E. S., Hassan, H. S., Ismail, Y. A., Emam-Ismail, M., & Ali, A. S. (2016). Structural, linear and nonlinear optical properties of co-doped ZnO thin films. Applied Physics A, 122, 1-10. https://doi.org/10.1007/s00339-015-9551-z.

Shkir, M., Arif, M., Ganesh, V., Singh, A., Algarni, H., Yahia, I. S., & AlFaify, S. (2020). An effect of Fe on physical properties of nanostructured NiO thin films for nonlinear optoelectronic applications. Applied Physics A, 126(2), 119. https://doi.org/10.1007/s00339-020-3293-2.

Shkir, M., Ganesh, V., AlFaify, S., Yahia, I. S., & Zahran, H. Y. (2018). Tailoring the linear and nonlinear optical properties of NiO thin films through Cr^{3+} doping. Journal of Materials Science: Materials in Electronics, 29, 6446-6457. https://doi.org/10.1007/s10854-018-8626-y.

Shkir, M., Kilany, M., & Yahia, I. S. (2017). Facile microwave-assisted synthesis of tungsten-doped hydroxyapatite nanorods: a systematic structural, morphological, dielectric, radiation and microbial activity studies. Ceramics International, 43(17), 14923-14931. https://doi.org/10.1016/j.ceramint.2017.08.009.

Taşköprü, T., Bayansal, F., Şahin, B., & Zor, M. (2015). Structural and optical properties of Co-doped NiO films prepared by SILAR method. Philosophical Magazine, 95(1), 32-40. https://doi.org/10.1080/14786435.2014.984788.

Taşköprü, T., Turan, E., & Zor, M. (2016). Characterization of NiO films deposited by homemade spin coater. International Journal of Hydrogen Energy, 41(16), 6965-6971. https://doi.org/10.1016/j.ijhydene.2015.12.008.

Usha, K. S., Sivakumar, R., & Sanjeeviraja, C. (2013). Optical constants and dispersion energy parameters of NiO thin films prepared by radio frequency magnetron sputtering technique. Journal of Applied Physics, 114(12). https://doi.org/10.1063/1.4821966.

Yang, X., Gao, P., Yang, Z., Zhu, J., Huang, F., & Ye, J. (2017). Optimizing ultrathin Ag films for high performance oxide-metal-oxide flexible transparent electrodes through surface energy

modulation and template-stripping procedures. Scientific Reports, 7(1), 44576. https://doi.org/10.1038/srep44576.

Zaouche, C. (2021). The role of Ni and Zn on diluted magnetic semiconductor $Ni_{1-x}Zn_xO$ thin films (Doctoral dissertation, Université de mohamed kheider biskra). http://thesis.univ-biskra.dz/id/eprint/5465.

Chapter 4 : Exploring Calcium Doping Effects on NiO Thin Films

4.1 Introduction

Doping is a basic method for manipulating semiconductor characteristics and creating new, multipurpose technological materials. Many experiments have recently been conducted to dope NiO thin films with different elements in order to change their characteristics (Amor et al., 2014). In this work, we have used one of the transition metal elements, calcium (Ca), as a dopant to adjust the optical and structural characteristics of NiO thin films produced using the spray pyrolysis technique. To our knowledge, only limited investigations are available on the synthesis of NiO thin films doped with calcium through the spray method, specifically for optoelectronic applications. Therefore, in this study, we describe how to create and characterize Ca-doped NiO thin films using spray pyrolysis on tiny glass substrates at varying doping concentrations. The impact of calcium (Ca) doping on the structural, morphological, as well as linear and nonlinear optical properties of NiO thin films is examined and discussed.

4.2 Fabrication and characterization details

The precursor for preparing pure NiO and Ca:NiO thin films was nickel nitrate ($Ni(NO_3)_2.6H_2O$), the dopant source was calcium nitrate tetrahydrate ($Ca(NO_3)_2.4\ H_2O$), and the solvent was distilled water. Using the spray pyrolysis method, pure NiO and Ca:NiO thin films were formed on a glass substrate. Separately, $Ni(NO_3)_2.6H_2O$ and $Ca(NO_3)_2.4H_2O$ were dissolved in distilled water at a concentration of 0.1 M. In order to achieve different doping concentrations of Ca (0%, 1%, 2%, 4%, and 8%), the two starting solutions were mixed in the appropriate volumetric ratios to create the final desired solutions. The solution combinations underwent rigorous stirring for thirty minutes using a magnetic stirrer, resulting in the production of a uniform and transparent green solution. Pure NiO and Ca:NiO were formed by maintaining a constant temperature of 480ºC for the glass substrate during the film deposition process. The optimized conditions were determined with the following parameters: the deposit duration (20 min), the carrier gas pressure (1 bar), and the spray nozzle-substrate distance (15 cm), all of which were maintained consistently for each concentration.

X-ray diffraction (XRD; PROTO AXRD Benchtop) using CuKα radiation (λ=1.54056Å) operating at 30 keV and 20 mA was used to examine the crystal structures of the doped and undoped thin films. The morphological characteristics of the samples were analyzed with SEM-EDX microscopes (Zeiss Smart EDX) under a power supply of 20 kV. A Shimadzu UV-VIS spectrophotometer (Model 1800) within the wavelength range of 200-900 nm was used to

perform optical measurements. There will be calculations and discussions of different linear and nonlinear optical characteristics using the measured optical data.

4.3 Results and discussions

4.3.1 Structural properties

The structural characteristics of NiO thin films formed at 480 °C on glass substrates were examined using XRD analysis. The XRD patterns of NiO thin films with various calcium percentages are displayed in Figure 4.1. Prominent diffraction peaks of the NiO thin films are detected corresponding to the (111), (200), and (220) planes, aligning with the ICDD file (ICDD 00-047-1049). According to the XRD examination, the Ca-doped NiO thin films had a high purity phase with an FCC cubic structure as no other unwanted peaks were observed at any concentration. The peak at (111) exhibits the highest intensity, suggesting that the (111) growth orientation is the preferred one. Furthermore, it is evident from the obtained X-ray pattern that both pure and doped NiO exhibit a polycrystalline nature, with peak broadening being a characteristic of nanoparticle formation.

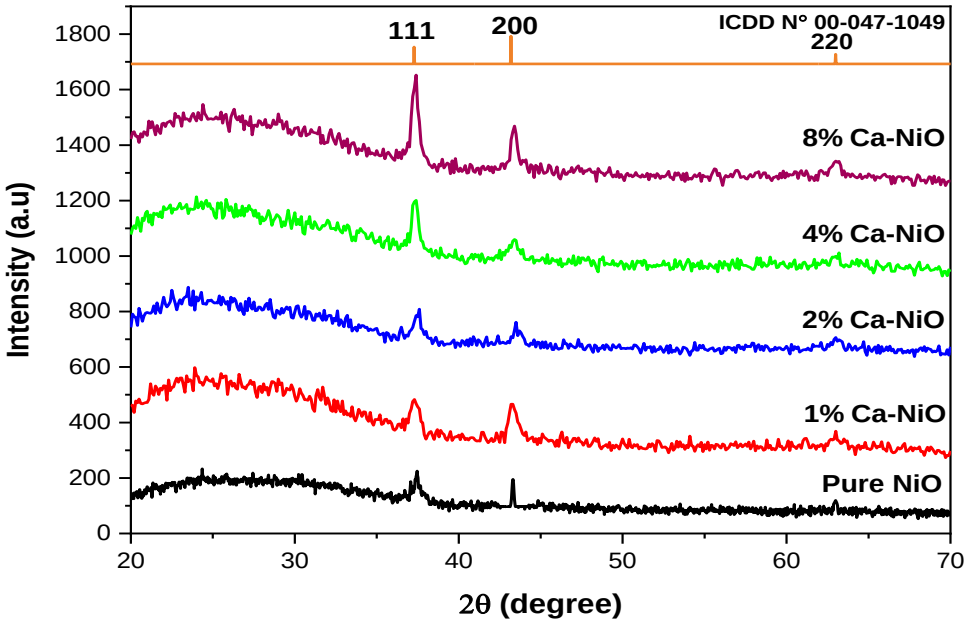

Figure 4.1. XRD pattern of Ca-doped NiO thin films.

Furthermore, as Ca-doped NiO thin films crystallizes in a cubic form, the interplanar spacing d_{hkl} values are estimated using the Bragg equation (Amor et al., 2014):

$$n\lambda = 2d_{hkl} \sin\theta \quad (4\text{-}1)$$

Similarly, employing the relationship of d_{hkl} for the cubic system and incorporating Miller indices for the crystalline plane (111), we derived the suitable lattice constant 'a' using the following relation (Amor et al., 2014):

$$\frac{1}{d^2} = \frac{h^2+k^2+l^2}{a^2} \quad (4\text{-}2)$$

Table 4.1 lists the computed values for d_{hkl}, FWHM and lattice constant (a) for Ca: NiO thin films made with different Ca concentrations. It is discovered that the lattice parameters for pure, 1, 2, 4 and 8 at% Ca-doped NiO thin films, as determined by the aforementioned equation, closely correspond with earlier findings (ICDD 00-047-1049). As can be seen in the Table 4.1, the estimated lattice parameters show that its value is comparatively higher than for pure film. This may be explained by the fact that the NiO lattice expands as a result of the large ionic radii of Ca^{2+} (0.99 Å) entering in substitution in the NiO lattice. The literature also reports similar behavours (Yang et al., 2011; Moghe et al., 2012).

Table 4.1. Structure parameters of undoped and Ca-doped NiO thin films.

Sample (doping %)	2θ (°)	hkl	d_{hkl} (Å)	FWHM	a (Å)	V (Å)^3
ICDD 00-047-1049	37.237	1 1 1	2.412	-	4.1790	72.9800
Pure NiO	37.443	1 1 1	2.401	0.266	4.1677	72.3931
1 % Ca–NiO	37.312	1 1 1	2.410	0.590	4.1757	72.8110
2 % Ca–NiO	37.469	1 1 1	2.40	0.590	4.1542	71.6929
4 % Ca–NiO	37.336	1 1 1	2.408	0.295	4.1704	72.5373
8 % Ca–NiO	37.334	1 1 1	2.408	0.393	4.1701	72.5191

Conversely, we have utilized the following relations to compute the crystallite size (D), lattice strain (ε), and dislocation density (δ) that represent the crystal structure of the films under study (Derbali et al., 2018):

$$D = \frac{0.9\lambda}{\beta \cos(\theta)} \quad (4\text{-}3)$$

$$\varepsilon = \frac{\beta \cos\theta}{4} \quad (4\text{-}4)$$

$$\delta = \frac{1}{D^2} \quad (4\text{-}5)$$

Where λ is the wavelength, β is the FWHM and θ is the angle of diffraction peaks. Table 4.2 contains a summary of all of the parameters described previously. Figure 4.2, shows the variation of these structural parameters as a function of Ca doping concentrations. Figure 4.2 demonstrates that as the Ca doping level increases moderately, lattice strain and dislocation density rise while grain size decreases. This is attributed to the incorporation of Ca into NiO through the formation of Ni–O–Ca bonds on the surface of small particles. This hinders the mobility of surface Ni atoms and the coarsening of particles by limiting direct contact between neighboring crystallites. Consequently, this prevents the agglomeration of NiO nanoparticles, thereby inhibiting their growth (El Radaf et al., 2019).

Table 4.2. Values of D, ε and δ for the (111) plane of NiO films in relation to the concentration of calcium.

Sample (doping %)	Crystallite size D (nm)	Lattice strain, ε ($\times10^{-3}$)	Dislocation density, δ ($\times10^{-3}$ nm^{-2})
Pure NiO	31.5342	1.0992	1.0056
1 % Ca–NiO	14.2116	2.4390	4.9512
2 % Ca–NiO	14.2182	2.4379	4.9466
4 % Ca–NiO	28.4252	1.2194	1.2376
8 % Ca–NiO	21.3369	1.6245	2.1965

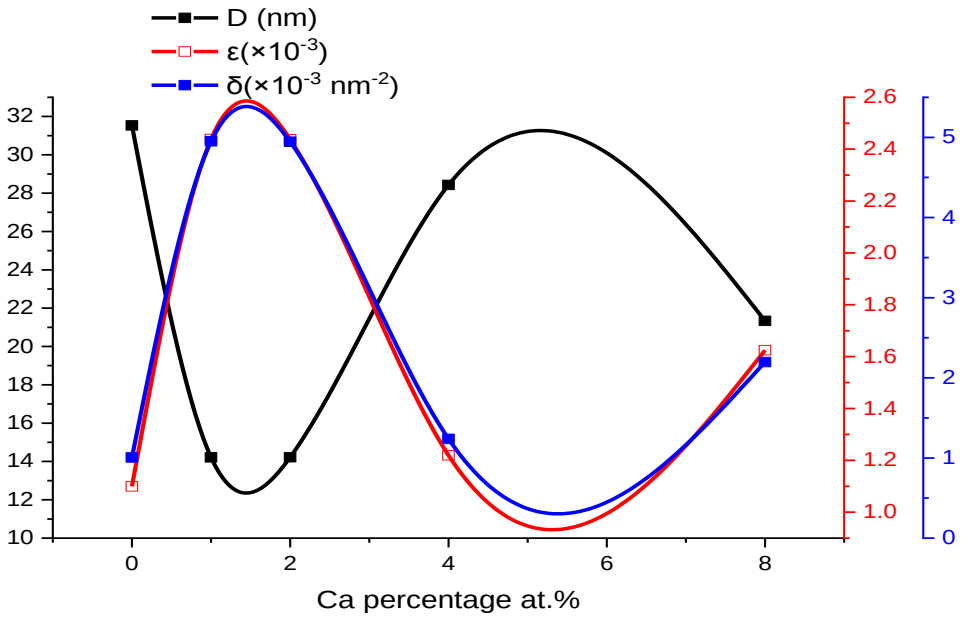

Figure 4.2 Correlation between crystallite size, lattice strain, and dislocation density in Ca:NiO films concerning Ca concentration.

4.3.2 EDX/SEM map analyses

The EDX technique is used analyzes the elemental composition of the grown thin films by detecting characteristic X-rays emitted when bombarded with high-energy X-rays. The EDX spectrum for Ca-doped NiO thin films are depicted in Figure 4.3. The findings revealed the presence of all anticipated elements (Ni, Ca, O) in the sample during preparation. The other peaks in the spectra are caused by the presence of glass substrate, which has also been reported earlier (Erdoğan et al., 2016; Adeoye et al., 2015). Furthermore, it is noted that the quantity of Ca rises proportionally with each concentration ratio, as indicated by EDX results table data in the inset of Figure 4.3 and are consistent with the measured spectrum.

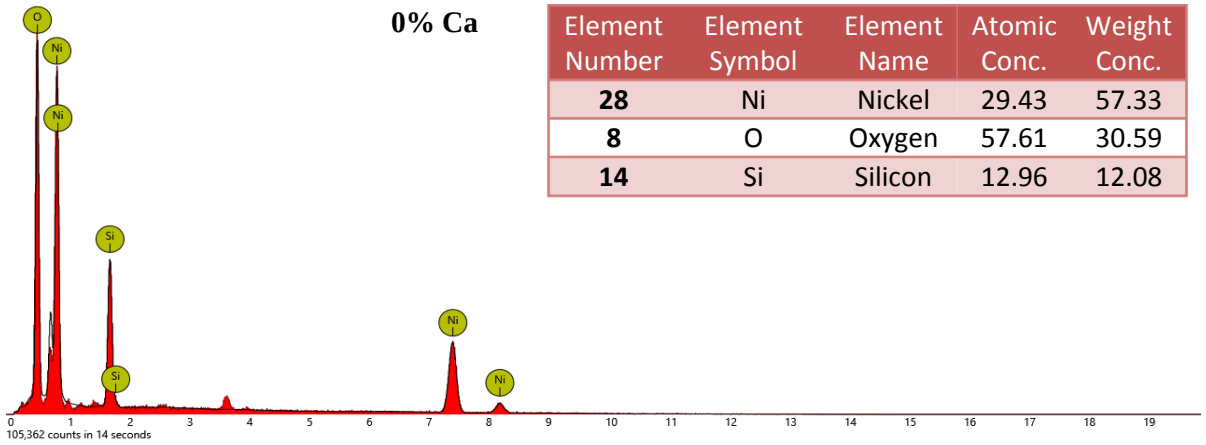

0% Ca

Element Number	Element Symbol	Element Name	Atomic Conc.	Weight Conc.
28	Ni	Nickel	29.43	57.33
8	O	Oxygen	57.61	30.59
14	Si	Silicon	12.96	12.08

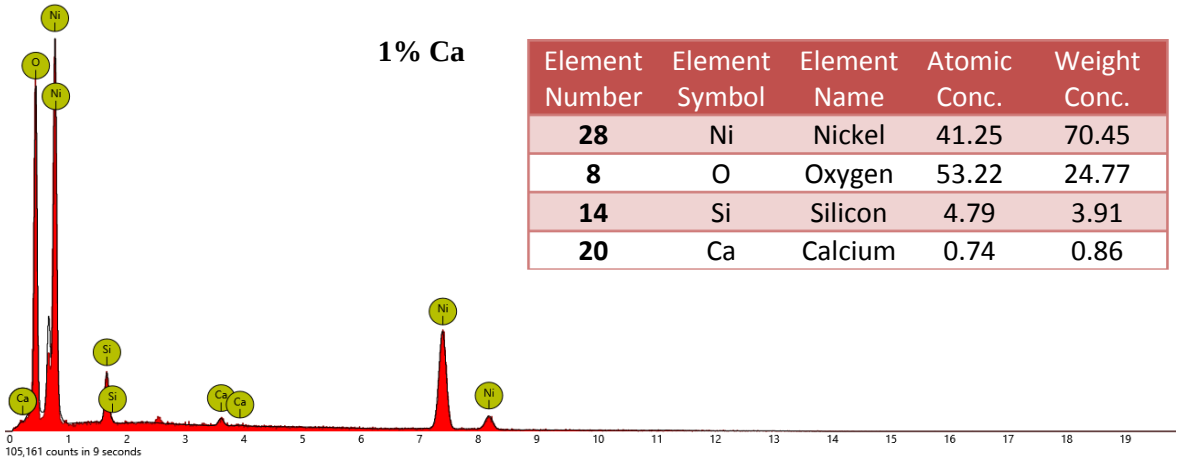

1% Ca

Element Number	Element Symbol	Element Name	Atomic Conc.	Weight Conc.
28	Ni	Nickel	41.25	70.45
8	O	Oxygen	53.22	24.77
14	Si	Silicon	4.79	3.91
20	Ca	Calcium	0.74	0.86

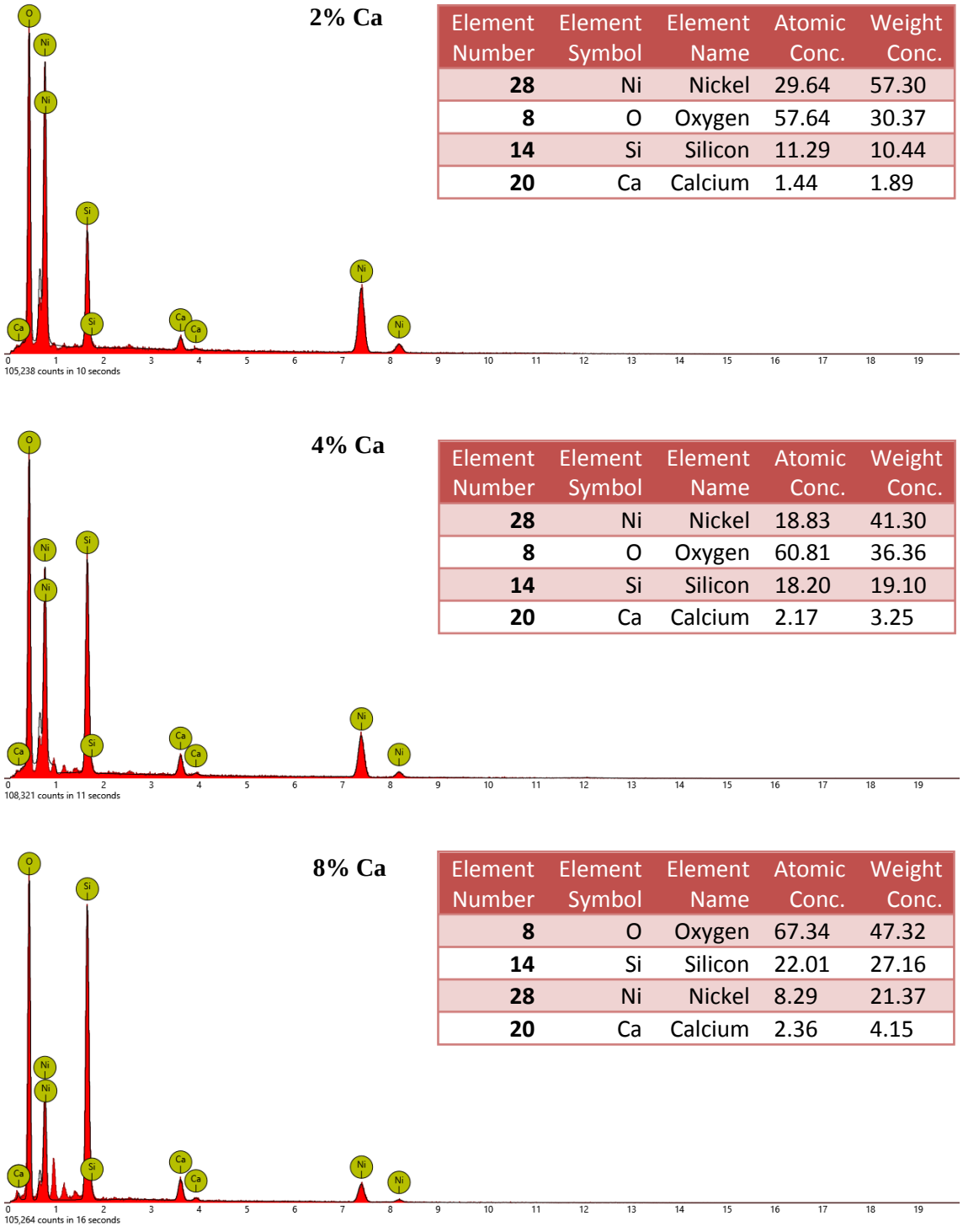

Element Number	Element Symbol	Element Name	Atomic Conc.	Weight Conc.
28	Ni	Nickel	29.64	57.30
8	O	Oxygen	57.64	30.37
14	Si	Silicon	11.29	10.44
20	Ca	Calcium	1.44	1.89

Element Number	Element Symbol	Element Name	Atomic Conc.	Weight Conc.
28	Ni	Nickel	18.83	41.30
8	O	Oxygen	60.81	36.36
14	Si	Silicon	18.20	19.10
20	Ca	Calcium	2.17	3.25

Element Number	Element Symbol	Element Name	Atomic Conc.	Weight Conc.
8	O	Oxygen	67.34	47.32
14	Si	Silicon	22.01	27.16
28	Ni	Nickel	8.29	21.37
20	Ca	Calcium	2.36	4.15

Figure 4.3. EDX spectra of pure and 1, 2, 4 & 8% Ca doped NiO thin films respectively

The SEM results enable us to characterize the diverse morphological features of NiO thin films, both for pure and doped with varying concentrations of Ca. Figure 4.4 demonstrates that the film samples had spherical or oval-shaped grains. In doped films, clusters of unevenly sized grains are evident. Furthermore, it is evident that when the dopant concentration rises, the form of clusters becomes more pronounced (Figure 4.4e) (Bhatt et al., 2020).

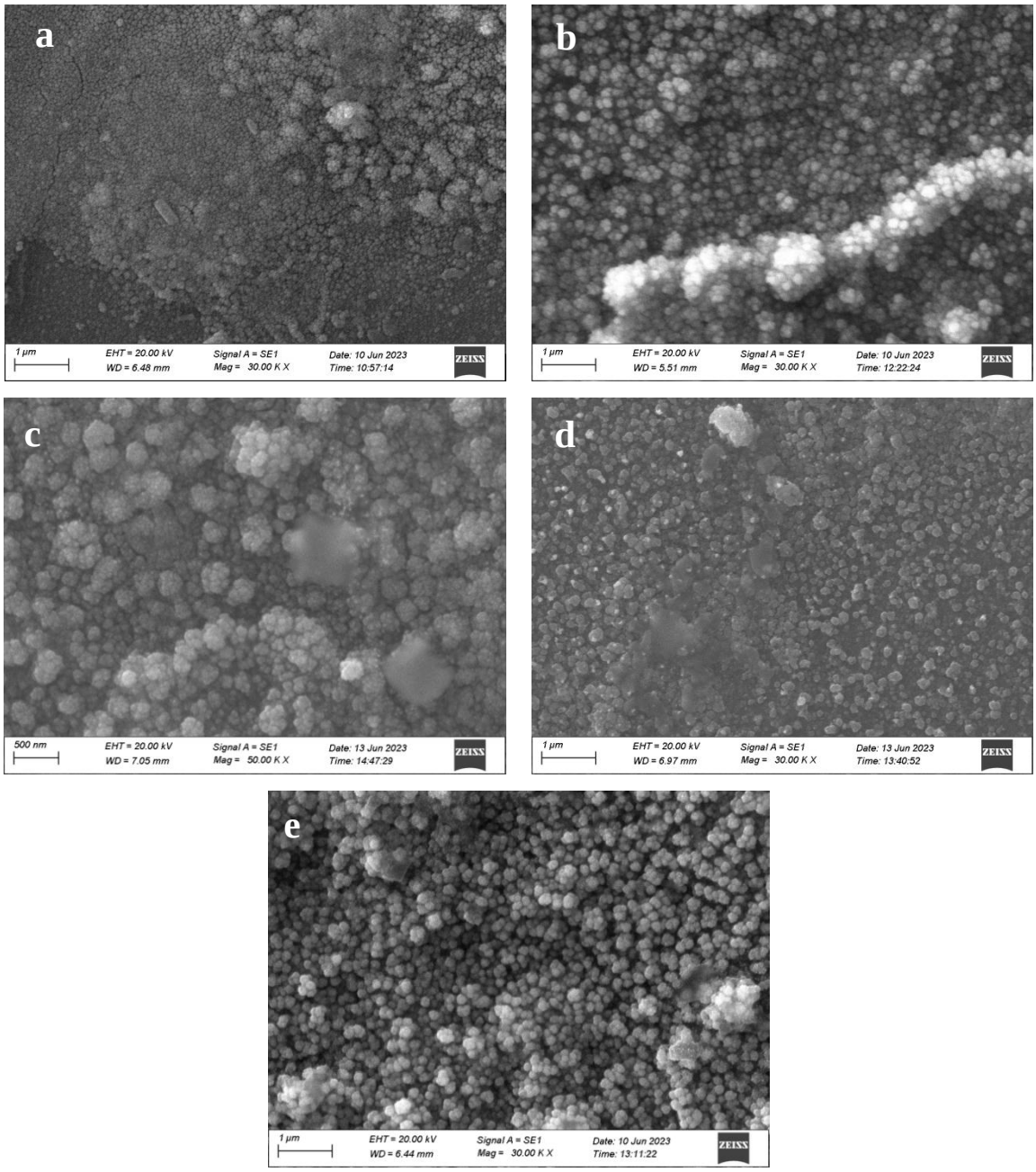

Figure 4.4 SEM micrographs of (a) 0% Ca (b) 1 % Ca(c) 2 % Ca (d) 4 % Ca and (e) 8 % Ca doped NiO thin films

4.3.3 Linear Optical Properties

UV-visible spectra were collected with an M1800 spectrophotometer. Figure 4.5 depicts the optical transmittance of pure NiO and Ca:NiO thin films. The spectral transmission measurements reveal that Ca doping alters the transparency of NiO films. All thin film transmittance rises with wavelength in the 310–400 nm region and then gradually increases at higher wavelengths. The transmittance range depicted by the spectrum falls within 30-65%, exhibiting a relatively modest level. The morphology, crystal structure, film thickness, and

defects created during thin film deposition are known to affect the optical transmittance of doped thin films (Sun et al., 2001). A comparative examination of all films demonstrated that the optical transparency reached its peak at approximately 60% for the film containing 8% Ca:NiO (refer to Fig. 4.5). Defects like microstrain, formed during thin film deposition, contribute to a decrease in film transparency. Specifically, in comparison to the 8% doping scenario, higher levels of microstrain are associated with reduced transparency in films doped at 1% and 2%. This observation suggests that films with higher Ca content exhibit superior transparency compared to those with lower Ca content. Furthermore, Figures 4.6 and 4.7 depict the absorbance and reflectance spectra of NiO thin films in their pure and Ca-doped forms, respectively, recorded across the range of 200 to 900 nm. As observed, the transmittance increased with the rise in the concentration of Ca doping, whereas absorption and reflection exhibited contrasting trends. The absorption characteristics of Ca-doped NiO thin films, depicted in Figure 4.6, are discernible in the UV region, aligning with the optical band gap absorption of NiO. Notably, there is a tendency for absorption to diminish with higher levels of Ca doping, as illustrated in Figure 4.6 (Sun et al., 2001; Ghougali, 2019).

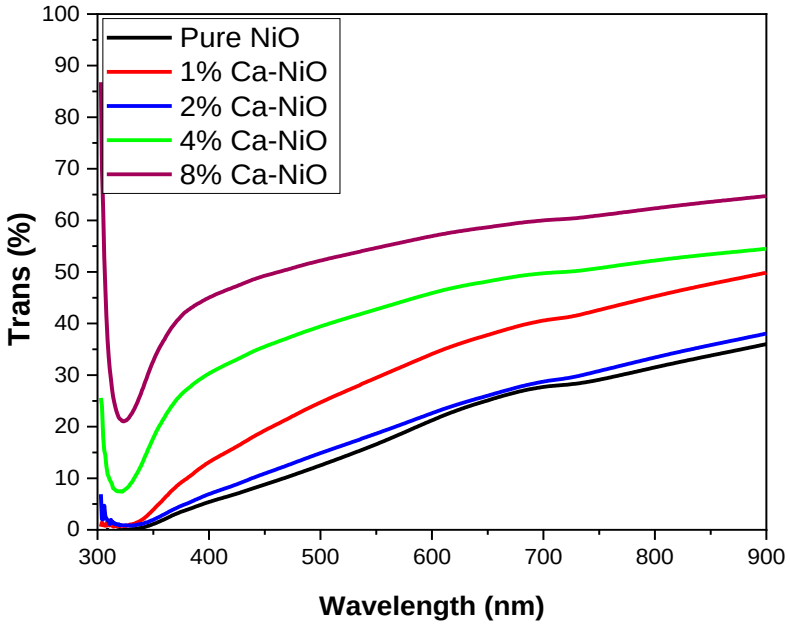

Figure 4.5. Transmittance spectra for all Ca: NiO films.

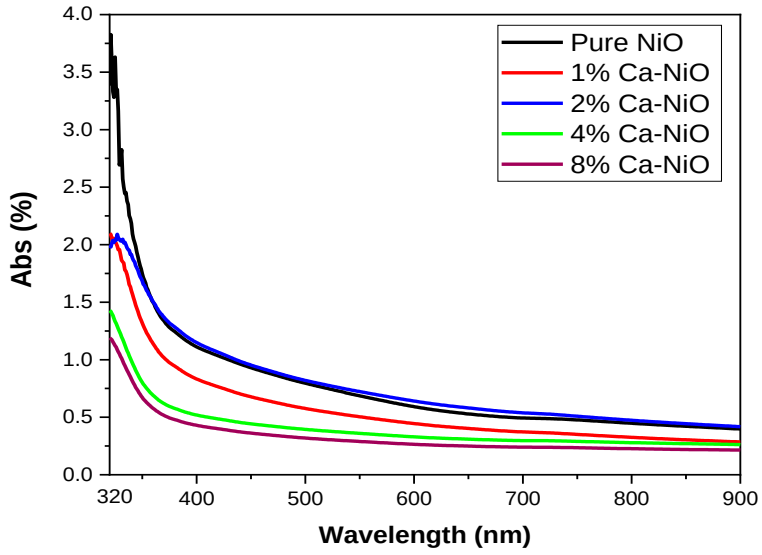

Figure 4.6. Absorbance spectra for all Ca: NiO films.

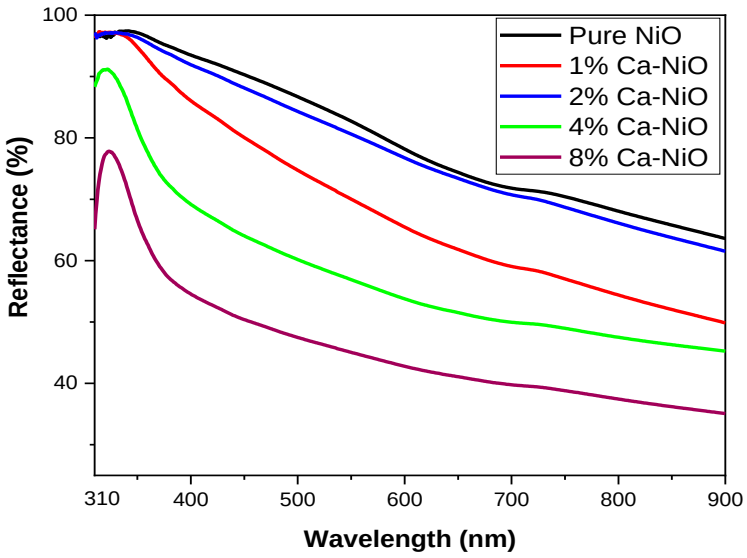

Figure 4.7. Reflectance spectra for all Ca: NiO films.

Exploring the band gap of thin films is crucial for understanding their potential in optoelectronic applications. Consequently, Tauc's equation was employed to investigate the band gap of our grown films (Mehta et al., 2009; Derbali et al., 2018):

$$\alpha h\vartheta = A\left(h\vartheta - E_g\right)^{1/2} \quad (4\text{-}6)$$

In this equation, α represents the absorption coefficient, A is a constant, Eg is the optical band gap and hv is photon energy.

The optical band gap is determined by extrapolating the linear portion of the curve to $(\alpha h\upsilon)^2=0$. The variation of the $(\alpha h\upsilon)^2$ curve and the extrapolation of its linear part of as a function of hυ are illustrated in Figure 4.8. The extracted band gap values, presented in Table 4.3, demonstrate a decrease from 3.43 to 3.30 eV with the rise in Ca doping content from 0 to 8 at%. This decline in the band gap could be attributed to several factors, including the reduction in grain size, the augmentation of disorders and defects, and an increase in the number of charge carriers. Analogous reductions in band gap have been documented in NiO films doped with Al, Co, Li, and Cu (Taşköprü et al., 2015; Moghe et al., 2012; Shkir et al., 2018).

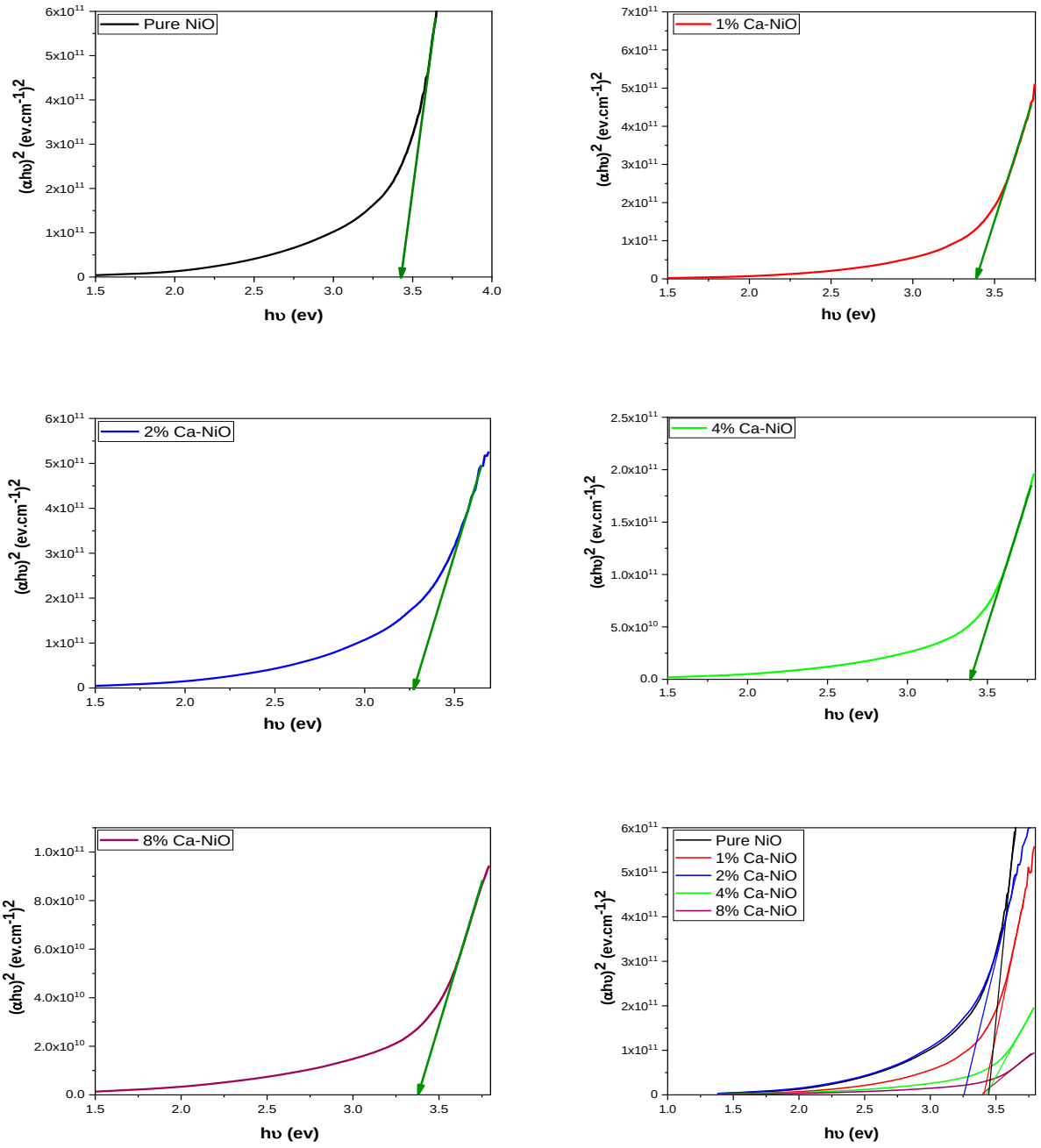

Figure 4.8. Direct band gap estimation for all Ca:NiO films.

Table 4.3. Estimated values of Urbach energy and optical bandgap.

Sample (doping %)	Eg (eV)	Eu (ev)
Pure NiO	3.43	0.142
1 % Ca–NiO	3.40	0.147
2 % Ca–NiO	3.30	0.208
4 % Ca–NiO	3.41	0.166
8 % Ca–NiO	3.39	0.263

Additionally, the band gap may reduce as a result of the expansion of band tails of Urbach energy (E_u) within the gap. The energy E_u was estimated using the Urbach's empirical relation (Urbach, 1953):

$$\alpha = \alpha_0 \exp\left(\frac{h\vartheta}{E_u}\right) \qquad (4\text{-}7)$$

where α_0 is a constant and E_u represents the Urbach energy, quantifying the width of the band tail associated with localized states within the optical energy gap. The Urbach energy for the studied films can be determined by creating a linear graph between ln(α) and hν, as demonstrated in Figure 4.9. Values for E_u were computed and presented in Table 4.3. It was observed that the Urbach energies increased with the addition of calcium content, providing further confirmation of the reduction in the bandgap. The acquired values of the band gap and Urbach energy were plotted as a function of calcium doping concentration, as shown in Figure 4.10 (El Radaf et al., 2019).

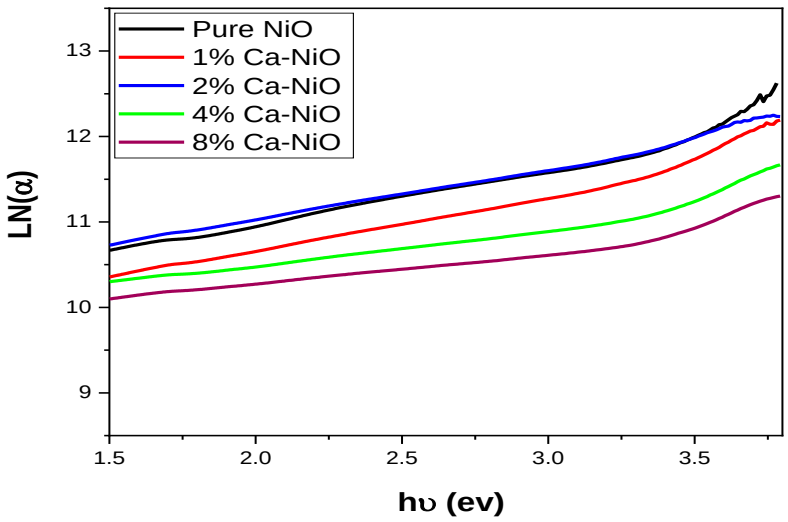

Figure 4.9. Plot of Ln(α) versus (hν) of Ca-doped NiO thin films at different calcium percentages.

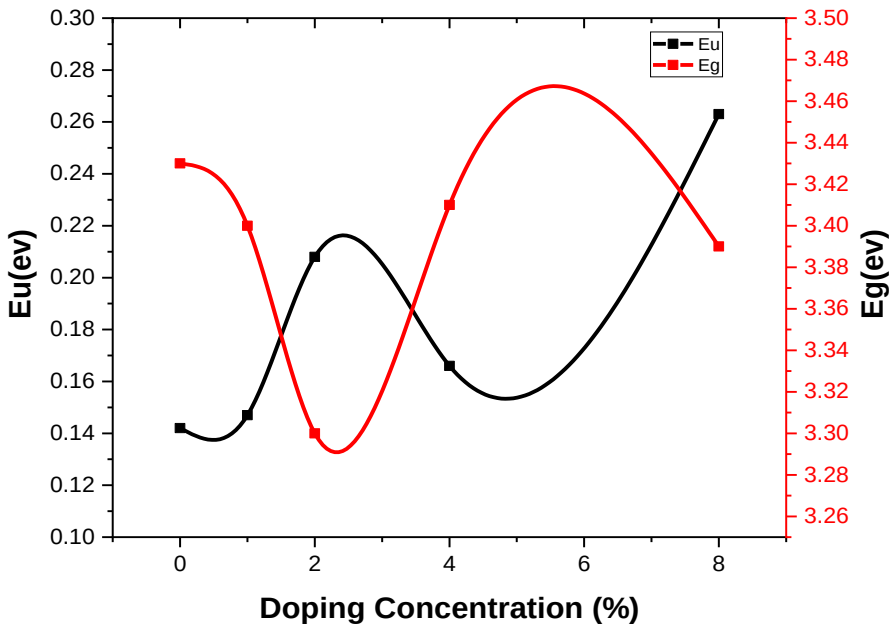

Figure 4.10 Plots of (E_g) and (E_u) at different calcium percentages for all Ca: NiO films.

The study of the linear refractive index (n) and extinction coefficient (k) is pertinent to optical qualities. They highlight the significance of structural alterations and polarization as function of doping concentrated when exposed to light. The formulas mentioned below were used to determine these parameters, k and n, respectively (Ganesh et al., 2018).

$$k = \alpha\lambda/4\pi \tag{4-8}$$

$$n = \frac{(1+R)}{(1-R)} + \sqrt{\frac{4R}{(1-R)^2} - K^2} \tag{4-9}$$

where R is the measured reflectance. [see Fig 4.7].

Thus, (k) and (n) for both doped and undoped NiO thin films were computed. These values were graphed against wavelength, as illustrated in Figure 4.11 and Figure 4.12. Figure 4.11 displays the computed values of k with respect to wavelength for each film. The values of k exhibit a range between approximately 0.8 and 0.15, indicating the impact of Ca doping on NiO thin films. It is discovered that as wavelength increases, k values drop. The low k values at high concentrations (4% and 8%) show that the films produced are free from surface defects and have good transparency. The refractive index n follows the same pattern, as seen in Figure 4.12. The figure clearly shows that the refractive index drops as wavelength increases and achieves a nearly constant value at high wavelengths (Ganesh et al., 2018).

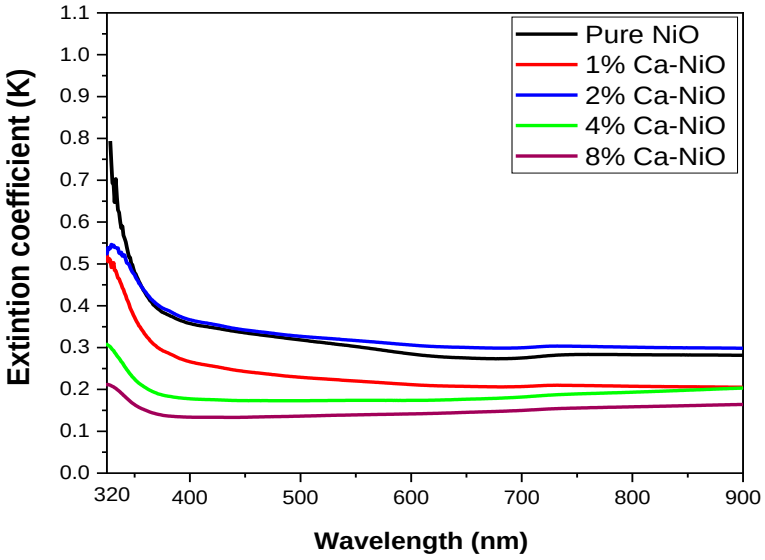

Figure 4.11 Variation of extinction coefficient for undoped and Ca-doped NiO films.

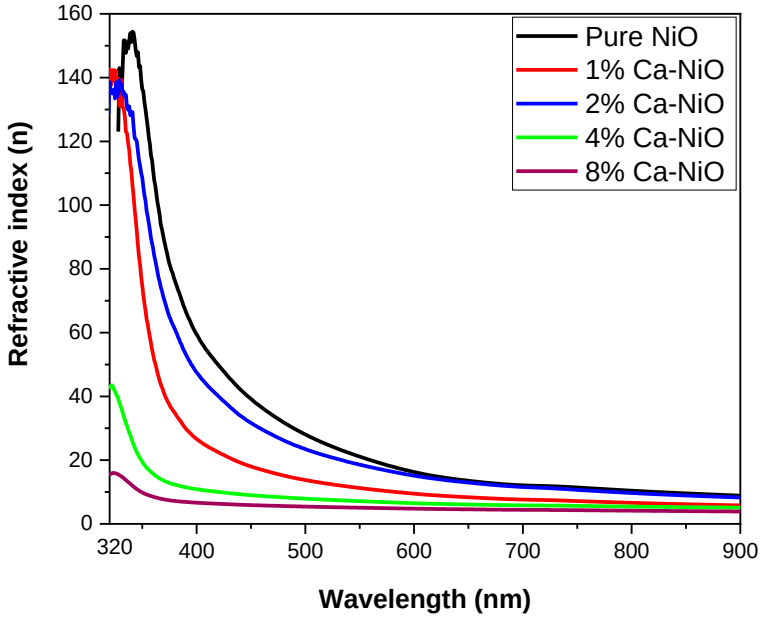

Figure 4.12 Variation of refractive index for undoped and Ca-doped NiO films.

4.3.4 Refractive index dispersion analyses

The refractive index dispersion in the Ca-doped NiO thin films as deposited with various Ca concentrations (0%, 1%, 2%, 4%, and 8%) can be analyzed using the single effective oscillator model proposed by Wemple DiDomenico (WDD). The model implies that the

refractive index n of the films may be connected with oscillator energy (E_o) and dispersion energy (E_d) using the following formula (Shaaban et al., 2016; El Radaf et al., 2019):

$$n^2(h\vartheta) = 1 + \frac{E_d E_0}{(E_0^2 - (h\vartheta)^2)} \quad (4\text{-}10)$$

Plotting the relationship between $(n^2\text{-}1)^{-1}$ and the square of the photon energy $(h\upsilon)^2$, as depicted in Figure 4.13. The values of E_o and E_d were directly determined from the slope and the intercept with the vertical axis of the straight line respectively. Furthermore, an additional examination of $(n^2\text{-}1)^{-1}$ versus $(h\upsilon)^2$ enables the determination of values such as n_0, Eg^{wmp}, M_{-1}, and M_{-3} using the relationships outlined in the previous chapter (Shaaban et al., 2016; El Radaf et al., 2019).

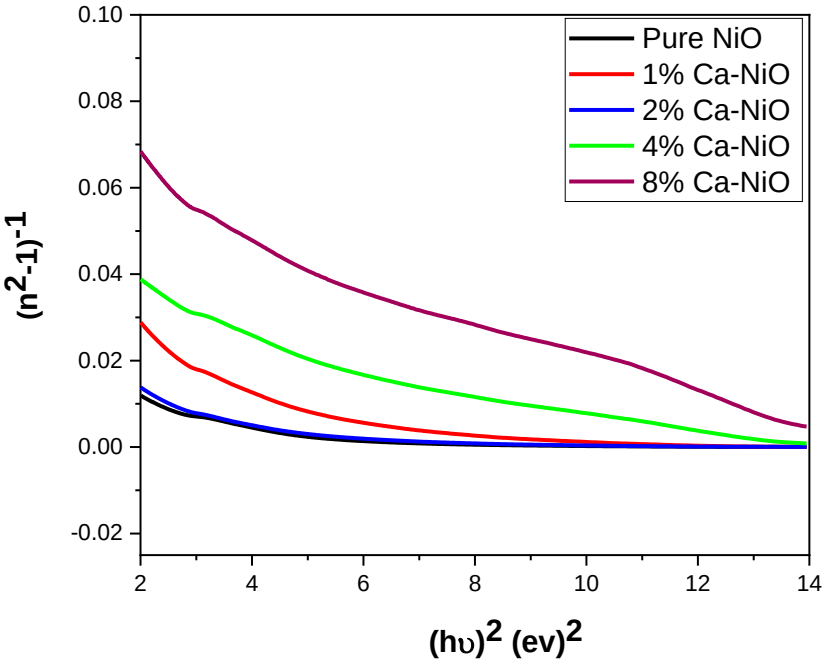

Figure 4.13 Variation of $(n^2\text{-}1)^{-1}$ against $(h\nu)^2$ for all Ca-doped NiO films.

Table 4.4 lists the obtained values for E_o, E_d, n_0, Eg^{wmp}, M_{-1}, and M_{-3}. It is evident that the increase in calcium concentration inside NiO films decreases the values of the dispersion parameters E_o, E_d, n_0, Eg^{wmp}, M_{-1}, and M_{-3}. This decline could stem from fluctuations in ionic bonding tendencies. It has been found that the relationship between Eo and Eg can be approximated as Eo ≈ 1.3 x Eg, aligning reasonably well with expectations from a single oscillator model (Caglar et al., 2007).

Table 4.4. Parameters for a single oscillator applicable to all Ca-doped NiO films.

Li at.%	E_d (ev)	E_0 (ev)	n_0	M_{-1}	M_{-3} (ev^{-2})	E_g^{wmp}
0	262.943	3.728	8.457	70.521	5.072	1.864
1	137.576	3.365	6.471	40.883	3.610	1.682
2	234.700	4.388	7.3807	53.475	2.776	2.194
4	94.350	3.667	5.1697	25.726	1.912	1.833
8	72.838	3.389	4.742	21.486	1.869	1.694

4.3.5 Nonlinear Optical Properties

Understanding the linear susceptibility (χ^1), third-order nonlinearity (χ^3), and nonlinear refractive index (n_2) of thin films is crucial for various applications. To understand the nonlinear behavior of the manufactured thin films and the influence of calcium doping on these properties, we calculated the above-mentioned parameters using the previously provided equations.

Figures 4.14 and 4.15 depict graphs of changes in linear and nonlinear optical susceptibilities. It has been noted that the optical sensitivity values, both linear and nonlinear, rise with increasing incident radiation energy and eventually become saturated at a certain wavelength (specific energy). This sort of change might be due to the interaction of light, which creates strong polarization in that specific wavelength region (Ganesh et al., 2017; Shkir et al., 2017). However, in Ca-doped NiO thin films, these values are found to decrease, possibly indicating that the interaction of light is causing lower polarization in the doped films.

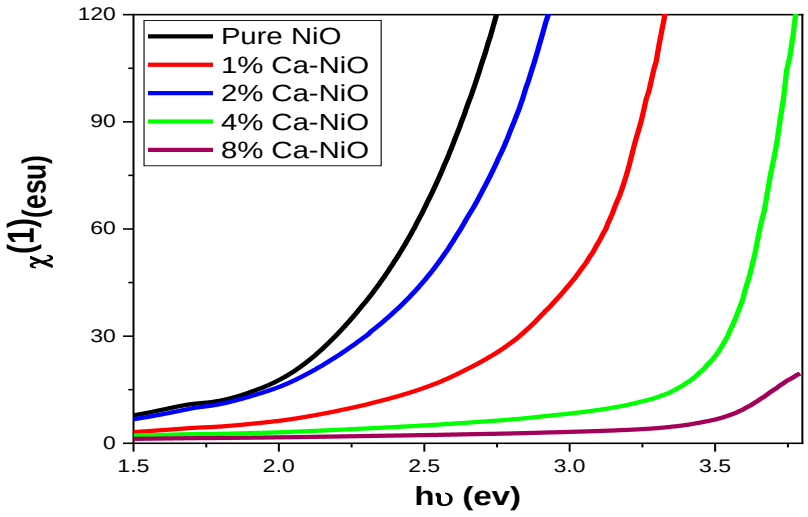

Figure 3.14. Variation of Linear Susceptibility versus photon energy of all Ca: NiO films.

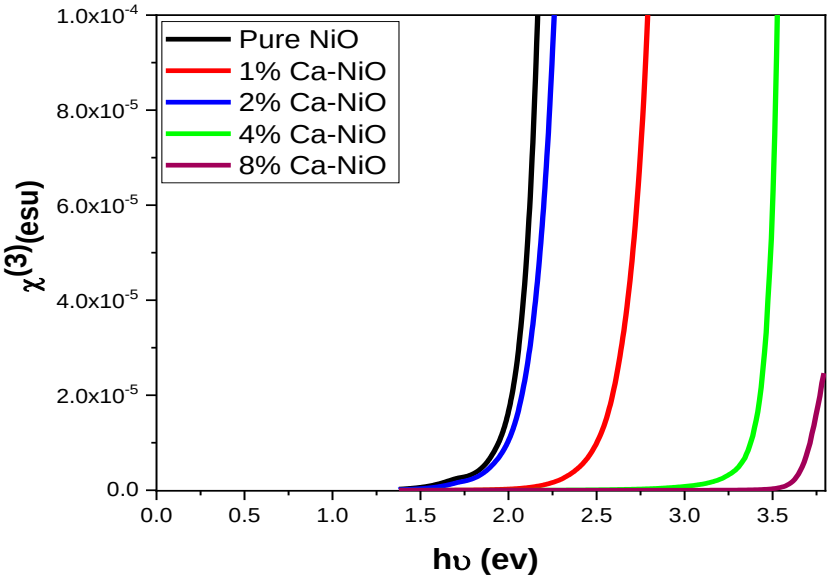

Figure 3.15. Variation of Nonlinear Susceptibility versus photon energy of all Ca: NiO films.

Moreover, the determination of the nonlinear refractive index (n_2) was undertaken, considering its significance as a crucial parameter for diverse applications in the optoelectronics of oxide films. The graph illustrating the variation of n_2 with E (eV) is presented in Figure 4.16. The n_2 values exhibit a comparable pattern to nonlinear susceptibilities, indicating a strong dependence on χ^3. It was observed that the n_2 values are sensitive to the doping content, and are in good agreement with the other parameters obtained for the films.

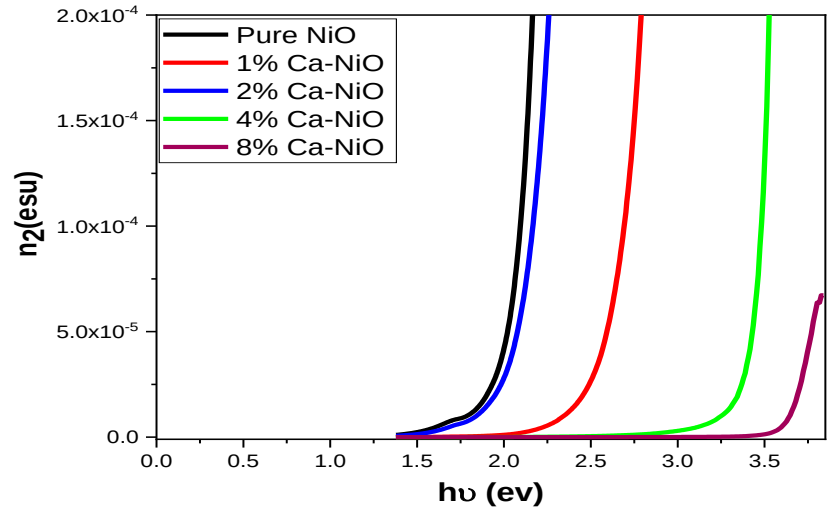

Figure 3.16. Plots of Nonlinear refractive index versus energy (hv) for all Ca:NiO films.

4.4 Conclusion

Undoped and Ca-doped NiO thin films were produced using a simple, low-cost spray pyrolysis process, and their linear and nonlinear optical characteristics were deeply investigated. The XRD investigation indicates that the produced films have a cubic structure and grow preferentially along (111) planes. The crystallite size values derived using Scherer's rule are seen to decrease from 31 to 14 nm with increasing Ca doping concentration. Agglomerations of particles with micropores were identified at higher magnifications Transmission and reflection measurements were used to estimate the optical constants of undoped and Ca-doped NiO thin films across the wavelength range of 200-900 nm. The direct energy gap values were calculated with a number of other factors, including absorption and refractive indices, oscillator parameters, and so on. The direct energy gap value ranges between 3.30 and 3.43 eV. Also, it has been observed that the calcium doping content affects the third-order nonlinearity (χ^3) and the refractive index nonlinearity (n_2).

References

Adeoye, A. E., Ajenifuja, E., Taleatu, B. A., & Fasasi, A. Y. (2015). Rutherford backscattering spectrometry analysis and structural properties of thin films deposited by chemical spray pyrolysis. Journal of Materials, 2015. http://dx.doi.org/10.1155/2015/215210.

Amor, M. B., Boukhachem, A., Boubaker, K., & Amlouk, M. (2014). Structural, optical and electrical studies on Mg-doped NiO thin films for sensitivity applications. Materials science in semiconductor processing, 27, 994-1006. https://doi.org/10.1016/j.mssp.2014.08.008.

Bhatt, A. S., Ranjitha, R., Santosh, M. S., Ravikumar, C. R., Prashantha, S. C., Maphanga, R. R., & Silva, G. F. L. E. (2020). Optical and electrochemical applications of Li-doped NiO nanostructures synthesized via facile microwave technique. Materials, 13(13), 2961. https://doi.org/10.3390/ma13132961.

Caglar, Y., Ilican, S., & Caglar, M. (2007). Single-oscillator model and determination of optical constants of spray pyrolyzed amorphous SnO 2 thin films. The European Physical Journal B, 58, 251-256. https://doi.org/10.1140/epjb/e2007-00227-y.

Derbali, A., Attaf, A., Saidi, H., Benamra, H., Nouadji, M., Aida, M. S., Attaf, N., & Ezzaouia, H. (2018). Investigation of structural, optical and electrical properties of ZnS thin films prepared by ultrasonic spray technique for photovoltaic applications. Optik, 154, 286-293. https://doi.org/10.1016/j.ijleo.2017.10.034.

El Radaf, I. M., Hameed, T. A., & Dahy, T. M. (2019). Synthesis, structural, linear and nonlinear optical properties of chromium doped SnO_2 thin films. Ceramics International, 45(3), 3072-3080. https://doi.org/10.1016/j.ceramint.2018.10.189.

Erdoğan, E., Kundakçı, M., & Mantarcı, A. (2016). InGaN thin film deposition on Si (100) and glass substrates by termionic vacuum arc. In Journal of Physics: Conference Series (Vol. 707, No. 1, p. 012019). IOP Publishing. https://doi.org/10.1088/1742-6596/707/1/012019.

Ganesh, V., Haritha, L., Anis, M., Shkir, M., Yahia, I. S., Singh, A., & AlFaify, S. (2018). Structural, morphological, optical and third order nonlinear optical response of spin-coated NiO thin films: An effect of N doping. Solid State Sciences, 86, 98-106. https://doi.org/10.1016/j.solidstatesciences.2018.10.009.

Ganesh, V., Yahia, I. S., AlFaify, S., & Shkir, M. (2017). Sn-doped ZnO nanocrystalline thin films with enhanced linear and nonlinear optical properties for optoelectronic applications. Journal of Physics and Chemistry of Solids, 100, 115-125. https://doi.org/10.1016/j.jpcs.2016.09.022.

Ghougali, M. (2019). Elaboration and characterization of nanostructuring NiO thin films for gas sensing applications (Doctoral dissertation, University of Mohamed Khider, Biskra). http://thesis.univ-biskra.dz/id/eprint/4617.

Mehta, C., Saini, G. S. S., Abbas, J. M., & Tripathi, S. K. (2009). Effect of deposition parameters on structural, optical and electrical properties of nanocrystalline ZnSe thin films. Applied Surface Science, 256(3), 608-614. https://doi.org/10.1016/j.apsusc.2009.06.023.

Moghe, S., Acharya, A. D., Panda, R., Shrivastava, S. B., Gangrade, M., Shripathi, T., & Ganesan, V. (2012). Effect of copper doping on the change in the optical absorption behaviour in NiO thin films. Renewable Energy, 46, 43-48. https://doi.org/10.1016/j.renene.2012.02.028.

Shaaban, E. R., El-Hagary, M., Moustafa, E. S., Hassan, H. S., Ismail, Y. A., Emam-Ismail, M., & Ali, A. S. (2016). Structural, linear and nonlinear optical properties of co-doped ZnO thin films. Applied Physics A, 122, 1-10. https://doi.org/10.1007/s00339-015-9551-z.

Shkir, M., Ganesh, V., AlFaify, S., & Yahia, I. S. (2017). Structural, linear and third order nonlinear optical properties of drop casting deposited high quality nanocrystalline phenol red thin films. Journal of Materials Science: Materials in Electronics, 28, 10573-10581. https://doi.org/10.1007/s10854-017-6831-8.

Shkir, M., Ganesh, V., AlFaify, S., Yahia, I. S., & Zahran, H. Y. (2018). Tailoring the linear and nonlinear optical properties of NiO thin films through Cr^{3+} doping. Journal of Materials Science: Materials in Electronics, 29, 6446-6457. https://doi.org/10.1007/s10854-018-8626-y.

Sun, R. D., Nakajima, A., Fujishima, A., Watanabe, T., & Hashimoto, K. (2001). Photoinduced surface wettability conversion of ZnO and TiO_2 thin films. The Journal of Physical Chemistry B, 105(10), 1984-1990. https://doi.org/10.1021/jp002525j.

Taşköprü, T., Bayansal, F., Şahin, B., & Zor, M. (2015). Structural and optical properties of Co-doped NiO films prepared by SILAR method. Philosophical Magazine, 95(1), 32-40. https://doi.org/10.1080/14786435.2014.984788.

Urbach, F. (1953). The long-wavelength edge of photographic sensitivity and of the electronic absorption of solids. Physical review, 92(5), 1324. https://doi.org/10.1103/PhysRev.92.1324.

Yang, M., Shi, Z., Feng, J., Pu, H., Li, G., Zhou, J., & Zhang, Q. (2011). Copper doped nickel oxide transparent p-type conductive thin films deposited by pulsed plasma deposition. Thin Solid Films, 519(10), 3021-3025. https://doi.org/10.1016/j.tsf.2010.12.009.

General conclusion

Conclusions and Future Work

Over the past decade, extensive research has been focused on NiO as a promising semiconductor material for photocatalysis, nanofibers, and optoelectronic applications. Regarding this thesis research, spray pyrolysis has been used to deposit undoped and Li-doped NiO thin films. It has been known that spray pyrolysis serves as a synthesis technique for generating high-quality NiO thin films. Despite extensive research and various characterization results reported on undoped and doped NiO thin films, many researchers still face challenges in optimizing several parameters and applications in practical devices. Several studies have shown that the doping type and doping ratio influence the morphology and structure of NiO core layers of the films by examining the morphological, microstructural, optical, and nonlinear properties. The present thesis addresses our contributions to the production and characterization of nanostructured NiO thin films as the future aims that this work can assist in attaining.

Nickel oxide thin films exhibit intriguing nonlinear properties, characterized by their ability to undergo significant changes in conductivity or optical properties in response to varying external stimuli, such as light or electric fields. These nonlinearity phenomena are pivotal in the development of advanced electronic and photonic devices, offering prospects for efficient modulation and control in various applications ranging from sensors to optoelectronics. Understanding and harnessing these properties hold promise for innovations in next-generation technologies.

1. Contributions

Studies on undoped and doped NiO thin films deposited on a glass substrate using spray pyrolysis yielded the following conclusions:

Studies on Lithium-Doped NiO Thin Films

- Current research is dedicated to investigating the structural and optical characteristics of pure and Li-doped NiO thin films deposited on glass substrates using spray pyrolysis.
- Samples were prepared with different amounts of Li doping (1%, 2%, 3%, and 5%) at 480°C.
- Results show a cubic structure with the (200) as the preferred orientation.
- Crystal size reduced from 75.62nm to 62.37nm with increasing Li in NiO lattice.
- The transmittance of (Li:NiO) films is high and ranges from 60% to 80%.

- Doping induces notable changes in band gap values, ranging from 3.38 to 3.66 eV.
- Increasing Li doping concentration increases the refractive index (n), extinction coefficient (k), and dielectric constants consistently.
- The Wemple DiDomenico (WDD) model was used to analyze refractive index dispersion and calculate oscillator parameters.
- The nonlinear characteristics values of χ^1, χ^3, and n_2 improved when the Lithium doping was added to the NiO lattice structure.

Studies on Calcium-Doped NiO Thin Films

- Undoped and Ca-doped NiO thin films were fabricated using the simple and cost-effective SPT method, their linear and nonlinear optical properties were investigated.
- XRD revealed a cubic structure with a preferred orientation along the (111) plane.
- Increasing the Ca doping level reduced crystallite size from 31 nm to 14 nm.
- At greater magnifications, SEM pictures showed clusters of particles with micropores, and the EDX spectra verified the elemental compositions.
- The estimated band gap energy gaps, absorption, refractive indices, and oscillator parameters etc.. were estimated.
- The values of the direct energy gap varied between 3.30 and 3.43 eV.
- Third-order nonlinearity (χ^3) and refractive index nonlinearity (n_2) were studied and found to be influenced by the calcium doping content.

The experimental characterization indicates that (Li or Ca) doping plays an important role in the structural, optical, and nonlinear properties of the films.

2. Future Work

- Study and improve methods for preparing doped nickel oxide films to improve the quality and crystal structure.
- Expanding the study of optical properties and crystal structure using more detailed analysis techniques.
- Exploring the effectiveness of doped nickel oxide films in nonlinear device applications such as laser devices and optical communication components.
- Investigating the incorporation of nickel oxide with other materials to enhance nonlinear performance.
- Building theoretical models to better understand interactions in membranes and guide future research.

ABSTRACT

Abstract: Nickel oxide (NiO) has gained significant attention as a transparent conductive oxide material with promising physical properties for diverse technological applications. This thesis presents a comprehensive exploration of the structural and optical properties of undoped and doped nickel oxide (NiO) thin films, focusing on two key studies. The first study investigates the effects of Lithium doping on the structural and optical characteristics of NiO thin films. These films were deposited using spray pyrolysis on glass substrates at 480 °C, with varying concentrations of Li doping. Structural analysis through X-Ray Diffraction (XRD) revealed a polycrystalline cubic structure, predominantly oriented along the (200) crystal plane. The films exhibited a remarkable transmittance ranging between 60% and 80%. The bandgap values (Eg) were significantly influenced by the Li doping ratios, varying from 3.38 to 3.66 eV. Furthermore, a thorough examination of linear and nonlinear optical properties indicated improvements in χ^1, χ^3, and n_2 with the incorporation of lithium doping into the NiO lattice. The second study focuses on producing and characterizing undoped and calcium-doped NiO thin films using the Spray Pyrolysis Technique. The XRD investigation indicates that the produced films have a cubic structure and grow preferentially along (111) planes. The introduction of calcium reduced the crystallite size from 31 to 14 nm. SEM images identified agglomerations of particles with micropores, while elemental compositions were confirmed through EDX spectrum analysis. Transmission and reflection measurements in the 200-900 nm wavelength range were used to determine the optical constants. The direct energy gap values ranged from 3.30 to 3.43 eV. Nonlinear susceptibility (χ^3) and refractive index nonlinearity (n_2) were also studied, revealing their sensitivity to calcium doping content.

Keywords: NiO thin films; Spray pyrolysis; Doping; Optical properties; Linear and nonlinear optics.

ملخص: اكتسب أكسيد النيكل (NiO) اهتمامًا كبيرًا باعتباره مادة أكسيد موصلة شفافة ذات خصائص فيزيائية واعدة للتطبيقات التكنولوجية المتنوعة. تقدم هذه الأطروحة استكشافاً شاملاً للخصائص الهيكلية والبصرية للأغشية الرقيقة لأكسيد النيكل (NiO)، مع التركيز على دراستين رئيسيتين. تبحث الدراسة الأولى في تأثيرات تطعيم الليثيوم على الخصائص التركيبية والبصرية لأغشية NiO الرقيقة. حيث تم ترسيب هذه الأفلام باستخدام تقنية الانحلال الحراري بالرش على ركائز زجاجية عند درجة حرارة 480 درجة مئوية، مع تركيزات متفاوتة من محتوى الليثيوم. كشف التحليل الهيكلي من خلال حيود الأشعة السينية (XRD) عن بنية مكعبة متعددة البلورات، موجهة في الغالب على طول المستوى البلوري (200). وأظهرت الأفلام نفاذية ملحوظة تتراوح بين 60% و80%. كما تأثرت قيم فجوة النطاق (Eg) بشكل كبير بنسب التطعيم بالليثيوم، والتي تراوحت من 3.38 إلى 3.66 إلكترون فولت. علاوة على ذلك، أشار الفحص الشامل للخصائص البصرية الخطية وغير الخطية إلى حدوث تحسينات في χ^1 وχ^3 وn_2 مع دمج شوارد الليثيوم في شبكة أكسيد النيكل. أما الدراسة الثانية فقد ركزت على إنتاج وتوصيف أغشية NiO الرقيقة غير المطعمة والمطعمة بالكالسيوم باستخدام تقنية الانحلال الحراري بالرش. تشير نتائج فحص XRD إلى أن الأفلام المنتجة لها بنية مكعبة وتنمو بشكل تفضيلي على المستوى البلوري (111). كما أدى إدخال شوارد الكالسيوم إلى تقليل حجم البلورات من 31 إلى 14 نانومتر. حددت صور SEM تجمعات الجسيمات ذات المسام الصغيرة، بينما تم تأكيد التركيبات الأولية من خلال تحليل طيف EDX. تم استخدام قياسات الإرسال والانعكاس في مدى الطول الموجي 200-900 نانومتر لتحديد الثوابت البصرية. تراوحت قيم فجوة الطاقة المباشرة من 3.30 إلى 3.43 إلكترون فولت. تمت أيضًا دراسة القابلية غير الخطية (χ^3) ومؤشر الانكسار اللاخطي (n_2)، مما يكشف عن حساسيتهما لمحتوى الكالسيوم المضاف.

الكلمات المفتاحية: أفلام أكسيد النيكل الرقيقة؛ الانحلال الحراري بالرش؛ التطعيم؛ الخصائص البصرية؛ البصريات الخطية وغير الخطية.